

NPS ARCHIVE
1967
KELLY, R.

AN INVESTIGATION OF THE OXIDIZER FLOW
PASSAGES IN A DUAL-COMBUSTION
LIQUID ROCKET ENGINE

ROBERT JOSEPH KELLY

DUDLEY KNOX LIBRARY
NAVAL POSTGRADUATE SCHOOL
MONTEREY, CALIF. 93943-5101

AN INVESTIGATION OF THE OXIDIZER
FLOW PASSAGES IN A DUAL-COMBUSTION
LIQUID ROCKET ENGINE

by

Robert Joseph Kelly
Lieutenant Commander, United States Navy
B. S., United States Naval Academy, 1959



Submitted in partial fulfillment of the
requirements for the degree of

Aeronautical Engineer

from the

NAVAL POSTGRADUATE SCHOOL
September 1967

NPS ARCHIVE

~~Thesis W-2867~~ C1

1967

KELLY, R.

ABSTRACT

This work was undertaken to determine the pressure drops in the oxidizer flow passages of a compact dual-combustion liquid rocket engine by means of fluid dynamic model tests, using air instead of liquids, to establish design data. Investigated also were flow distributions and flow instabilities by measurements and flow visualization methods. Changes are indicated to improve the original design.

The air tests were carried out over a range of Reynolds numbers to establish the effect of compressibility on the pressure drop loss coefficients. Water tests were undertaken to check the validity of the results and of the proposed calculating method.

The tests were conducted at the Turbo-Propulsion Laboratory of the Naval Postgraduate School, Monterey, California.

Thesis by Robert Joseph Kelly entitled: "An investigation of the Oxidizer Flow Passages in a Dual-Combustion Liquid Rocket Engine"

ERRATA

<u>Page</u>	<u>Line</u>	<u>Change</u>	<u>To</u>
13	3	Unit of viscosity	lb sec/ft ²
13	4	Unit of kinematic viscosity	ft ³ /sec
20	22/23	Manom-eter	Mano-meter
22	10/11	Manom-eter	Mano-meter

TABLE OF CONTENTS

Section	Page
1. Introduction	15
2. Description of ARES Unit and Test Model	17
3. Test Installation and Instrumentation	20
4. Theoretical Considerations	23
5. Description of Tests	29
6. Results and Discussion	34
7. Conclusions	49
8. Bibliography	117
Appendix	
A. Derivation of Flow Measuring Equation	118
B. Data Reduction for Air and Water Tests with Flow Channel	120
C. Data Reduction for Tests with ARES Model	123

LIST OF TABLES

Table	Page
I. Index of Runs	51
II. Oxidizer Return Sub-assembly, Inlet Orifice Data and Equivalent Flow Rates	52
III. Flow Distribution through Orifice Plate, Loss Coefficient Plane D to Plane X, R1, R2, R3	53
IV. Flow Distribution through Orifice Plate, Loss Coefficient Plane D to Plane X, R4, R5, R6	54
V. Area Restriction Plane E, Mach Number Planes E, F, and I, Loss Coefficients Planes D to F, X to F, F to G, and G to I	55
VI. Peripheral Distribution of Loss Coefficient Planes A to F and D to F	56
VII. Loss Coefficients Planes G to H and H to I Runs R1 through R6	57
VIII. Velocity Distribution Plane I	58
IX. Results of Water Tests with Scale Model Nozzle Tube	59
X. Results of Water Tests with Geometrically Similar Model of Section between Planes W and X	60
XI. Oxidizer Discharge and Return Assembly, Inlet Orifice Data and Equivalent Flow Rates	61
XII. Loss Coefficients Planes Z to A, A to F, F to G, G to H, H to I, W to X, Discharge Mach Number	62

LIST OF ILLUSTRATIONS

Figure	Page
1. Artist's Conception of ARES Propulsion System	63
2. Scale Model of Rocket Nozzle Tubes	64
3. View of Assembled ARES Model	65
4. Schematic of Flow Passages in ARES Model	66
5. View of Part 1 of ARES Model	67
6. View of Part 2 of ARES Model	68
7. View of Part 3 of ARES Model	69
8. Exploded View of Parts 4, 5 and 6 of ARES Model	70
9. View of Part 7 of ARES Model	71
10. View of Return Annulus	72
11. View of Supply Pipe and Plenum 2	73
12. Schematic of Sharp Edge Orifice and Flow Nozzle	74
13. Schematic of Flow Measuring Installation	75
14. View of Test Installation for Assembled ARES Model	76
15. Total Pressure Probe Used at Model Inlet	77
16. Schematic of Inlet Total Pressure Probe Installation	78
17. View of Discharge Plane Total Pressure Probe Assembly	79
18. Schematic of Injector Tube and Total Pressure Probe Alignment	80
19. View of Removable Total Pressure Probe	81
20. View of Adapter for Return Sub-assembly Installation	82
21. Oxidizer Return Sub-assembly Test Installation with Provisions for Water Flow Visualization	83
22. View of a Flow Channel	84
23. View of Air Test Installation of Flow Channel	85
24. Inlet to Discharge Loss Coefficient of Flow Channel vs. Reynolds Number	86

Figure	Page
25. View of Water Test Installation of Flow Device	87
26. View of Test Installation of Nozzle Tubes	88
27. View of Test Installation for Geometrically Similar Model of Plane W to Plane X	89
28. Schematic of Test Installation for Geometrically Similar Model of Plane W to Plane X	90
29. Orifice Discharge Coefficient vs. Reynolds Number	91
30. Total Pressure Loss Plane D to Plane X vs. Reynolds Number	91
31. Peripheral Flow Distribution Plane D to Plane X	92
32. Friction Factors for Flow in Pipes	93
33. Peripheral Distribution of Loss Coefficient Plane G, Runs R1 through R6	94
34. View of Intersection of Passages from Plane G to Return Annulus	95
35. Average Loss Coefficients Return Sub-assembly vs. Reynolds Number	96
36. Discharge Plane I and Location of Plane H Measuring Taps	97
37. Discharge Velocity Distribution Run R3	98
38. Discharge Velocity Distribution Run R4	99
39. Discharge Velocity Distribution Run R5	100
40. Discharge Velocity Distribution Run R6	101
41. One Half of Return Annulus Developed into Plane	102
42. Flow in Return Annulus Run R4	103
43. Flow in Return Annulus Run R5	107
44. Nozzle Tube Loss Coefficient vs. Reynolds Number	111
45. Friction Factor vs. Reynolds Number for Runs W1 and W2	112
46. Friction Factor vs. Reynolds Number for Run W3	113

Figure	Page
47. Loss Coefficient ξ vs. Reynolds Number	114
48. Peripheral Distribution of Loss Coefficient Plane G, Runs R7 through R11	115
49. Average Loss Coefficients Assembled Model vs. Reynolds Number	116

LIST OF SYMBOLS

Symbol	Definition	Units
A,B,C,D, E,F,G,H, I,W,X,Y,Z	Location of measuring planes within ARES model	---
ARES	Advanced Rocket Engine Storable	---
A	Area	in ²
d	Diameter	in
d	Position downstream of flow measuring orifice	---
dis	Discharge	---
e	Roughness parameter based on average variation of inside radius	ft
F _i	Flow distribution factor plane D	---
f _r	Reynolds number correction factor	---
f _t	Area multiplier to account for thermal expansion of nozzle	---
g	Universal gravitational constant	ft/sec ²
H	Total pressure indication on manometer	---
h	Static pressure indication on manometer	---
H _L	Head loss	in
h _L	Head loss	lb/ft ²
in	Inlet	---
K	Orifice discharge coefficient dependent on Reynolds number	---
k	Combined frictional and momentum loss coefficient	in ⁻⁴
l	Length	ft
M	Mach number	---
o	Position at entrance to simulated pump vanes	---

Symbol	Definition	Units
P	Static pressure	lb/in ²
P _t	Total pressure	lb/in ²
q	Dynamic pressure	lb/in ²
R	Gas constant for air 53.35	$\frac{\text{ft-lb}}{\text{lb}_m \cdot \text{R}}$
Re	Reynolds number	---
T	Temperature	°R
T _t	Total Temperature	°R
t	Temperature	°F
t'	Elapsed time	sec
u	Position upstream of flow measuring orifice	---
V	Velocity	ft/sec
\dot{V}	Volume flow rate	in ³ /sec
\dot{w}	Mass flow rate	lb _m /sec
w*	Equivalent flow rate	in ²
W _t	Weight of water	lb
Y ₁	Expansion factor for compressibility effects	---
z	Height above reference plane	ft
α	Nozzle discharge coefficient independent of Reynolds number	---
β	Diameter ratio	---
γ	Ratio of specific heats	---
γ _L	Specific weight	lb/ft ³
f	Loss in total pressure divided by static pressure change across orifice	---
ζ	Frictional loss coefficient	---
θ	Angle indicating peripheral location	---

Symbol	Definition	Units
λ	Momentum loss coefficient	---
μ	Viscosity	---
ν	Kinematic viscosity	---
ξ	Combined frictional and momentum loss coefficient in geometrically similar systems	---
ρ	Density	lb _m /ft ³
ψ	Combined friction and momentum loss coefficient	---
ϕ	Area restriction factor	---

SECTION 1

INTRODUCTION

The science of astronautics has progressed at an exponential rate in the last decade. The development of liquid rocket engines capable of producing large thrusts at high specific impulse has been responsible for this progress. These engines require very large flow rates of fuel and oxidizer. To keep their size and weight at a minimum the combustion pressures are high, limited only by structural and turbo-pump design considerations. The flow passages inside the units are intricate and costly to manufacture. Pressure losses in these passages are high and must be known in order to establish pump and turbine design point data. Accurate prediction of these losses by analytical means is not possible except for flow passages with simple geometries. Therefore, it is advisable to conduct model tests with fluids at low pressure, preferably air, to determine pressure loss coefficients experimentally which can then be used to predict the pressure losses in the actual engine.

The ARES (Advanced Rocket Engine Storable) propulsion unit is a compact dual-combustion liquid rocket engine designed by the Aerojet-General Corporation, Sacramento, California. Professor M. H. Vavra of the Department of Aeronautics, Naval Postgraduate School, Monterey, California, has designed full-scale fluid dynamics models of this unit and has conducted preliminary tests of the oxidizer flow passages with air. The models have been made available to the writer by Aerojet-General and were used to carry out more extensive and more detailed testing with improved instrumentation.

The purpose of this thesis is threefold. First, the air test results are used to predict the pressure drops in the flow passages, flow distribution within the unit, and velocity distribution at the entrance to the combustion chamber for a liquid flow. Second, the effects of compressibility and Reynolds number on the test results are investigated, and the validity of the testing method is established. Third, changes in design are recommended based on the test results and flow visualizations.

The author wishes to acknowledge the guidance provided by Professor Vavra and extends sincere thanks to Mr. R. W. Savage for his assistance in performing experiments. Acknowledgment is due also to Mr. R. Beichel, Aerojet-General Corporation, for the loan of the models and his endeavors to apply model testing techniques to the design of advanced rocket engines.

SECTION 2

DESCRIPTION OF ARES UNIT AND TEST MODEL

A three-dimensional schematic representation of the oxidizer passages of the ARES propulsion unit is shown in Fig. 1. The oxidizer is composed of a mixture of nitrogen tetroxide and hydrazine and it is used for regenerative cooling of the combustion chamber and the rocket nozzle before being mixed with the fuel. Oxidizer enters the outer annulus through a centrifugal pump. This annulus contains turning vanes, not shown in Fig. 1, to distribute the flow uniformly to the tubes that form the outer skin of the nozzle. Each tube is an integral unit consisting of a down-flow and an up-flow passage. The entrance and exit holes are in the same plane perpendicular to the nozzle axis; however, they are located at different radii in this plane. The tubes begin and end with an inner diameter of 0.3 inches. At the nozzle throat they form an ellipse with major and minor axes of 0.31 in. and 0.19 in., respectively. This elliptical cross section gradually increases until at the bottom of the tubes the major and minor axes have values of 0.76 in. and 0.70 in. A scale model of one of these tubes is shown in Fig. 2. From the discharge of the tubes the oxidizer enters a second annular chamber concentric with that into which the pump discharges. In this annular passage the flow is turned to enter a series of 60 holes drilled radially in the inner shell of the second annulus. The oxidizer is then discharged into the primary combustion chamber through 180 injectors. A flow passage, not shown in Fig. 1, directs the combustion gases to a single-stage axial turbine which drives the pump previously mentioned. Details of this flow passage are

given by Vavra.¹ Tests of two turbine designs have been performed, the results of which are reported by Vavra² and Messegue.³

The portion of the unit from the inlet of the outer annulus to the bottom of the rocket nozzle is called the oxidizer discharge. The portion including the remainder of the nozzle tubes to the injectors is called the oxidizer return. Secondary combustion takes place after the turbine discharge and ahead of the nozzle throat.

A scale model of these flow passages has several modifications as far as shape and layout of the actual unit is concerned, but mostly retains flow passage dimensions. The model, shown assembled in Fig. 3, is constructed of plastic and aluminum and weighs 136 pounds. A schematic of the flow passages is shown in Fig. 4. The discharge and return annuli are separated by 7 parts of varying flow areas and shapes. Flow enters the model through simulated pump vanes which impart a whirl component. The whirl is removed by turning vanes and the flow is distributed to part 1, shown separately in Fig. 5. Part 1 has 32 equally spaced groups of 3 holes with a total flow area of 4.712 sq. in. Parts 2 and 3 are shown respectively in Figs. 6 and 7. Each of these parts has 52 equally spaced single holes with a total flow area of 2.552 sq. in. Parts 4, 5, and 6 together with 2 orifice plates simulate the nozzle tubes. An exploded view of this assembly is shown in Fig. 8. The first orifice plate, having holes of diameter $d = 0.217$ in. and diameter ratio $d/D = \beta = 0.723$ simulates the ~~down-flow of the nozzle~~ tubes. The second plate with $d = 0.216$ in. and $\beta = 0.720$ simulates the up-flow of the nozzle tubes. Part 7, shown in Fig. 9, has 32 equally spaced triple holes with a total flow area of 5.574 sq. in. From part 7 the flow passes into the second annulus shown in Fig. 10,

where it is turned to enter the injectors. Each of the 60 injector tubes has 3 holes labeled A, B, C, respectively, from the outer radius inward. The tubes are labeled clockwise from 1 to 60 with the first tube just past the nine o'clock position when the injectors are viewed from the combustion chamber (see Fig. 36).

The model can be divided into sub-assemblies for testing. Tests on the oxidizer discharge sub-assembly including the first annulus through part 5, excluding the second orifice plate, were made by Vavra.⁴ Preliminary tests of the return sub-assembly, part 6 through the injectors including the second orifice plate, were also made by Vavra. This paper presents more complete tests of the return sub-assembly, in addition to tests of the fully assembled unit.

SECTION 3

TEST INSTALLATION AND INSTRUMENTATION

Available as a source of air is a 200 H. P. centrifugal compressor which delivers about 4 pounds mass of air per second at a pressure ratio of about 2. Part of this flow passes through a cooler; the rest discharges through a butterfly valve to atmosphere. Figure 13 is a schematic of the flow measuring installation. The cooled air enters plenum 1 then passes through a 4 in. pipe discharging into plenum 2 shown in Fig. 11. Flow measurement is accomplished by either a sharp edge orifice or a flow nozzle installed in the 4 in. pipe (Fig. 12). The design of the orifice and the flow nozzle is in accordance with VDI standards⁵, and the installation satisfies or exceeds the specified requirements of pipe lengths upstream and downstream of it. In addition a flow straightener is installed at the discharge of plenum 1. The orifice has a diameter $d = 3.024$ in. and a diameter ratio $\beta = 0.7429$. The nozzle has $d = 3.022$ in. and $\beta = 0.734$. Initial tests conducted by Vavra used the sharp edge orifice to measure flow rate. Prior to all tests performed by the writer the flow nozzle was installed.

Appendix A contains the derivation of the flow measuring equation for the nozzle. Similar information on the orifice is given by Kelly.⁶ Plastic hoses connect pressure taps with the measuring instruments. The pressure difference $P_u - P_d$ is measured by a Meriam Vernier Manometer filled with water. The gage pressure ahead of the nozzle is measured by a similar manometer filled with mercury. The measuring accuracy of these manometers is about ± 0.002 in. The temperature t_u is measured with an accuracy of $\pm 1^\circ\text{F.}$ by an iron-constantan thermocouple located 48.5 in. upstream of the nozzle.

Within plenum 2 there is arranged a bend and a 10 deg. conical diffuser with a series of screens at the discharge to minimize flow instabilities. A second thermocouple is situated within plenum 2. Plenum pressure is read on either a mercury filled manometer or a water filled manometer bank. Three such manometer banks were used. Bank 1 is a 250 cm. 40-tube bank which can be read to an accuracy of ± 0.1 cm. Bank 2 is a 175 cm. 60-tube bank with a reading accuracy of ± 0.2 cm. Bank 3 is a 92 in. 20-tube board that can be read with an accuracy of ± 0.1 in.

The model is attached to plenum 2 by means of a steel plate visible in Fig. 11. Mounted on this plate is a wooden nozzle of circular cross section to produce uniform entrance conditions. Situated at the throat of the nozzle is a Kiel probe measuring total pressure $P_{t_{in}}$. For tests with the entire model assembly the conduit shown in Fig. 14 is used to introduce air from opposite directions into the first annulus. Static pressure taps measuring P_o are located 1.5 in. ahead of the model inlet. In the same plane are located probes to measure P_{t_o} . One such probe is pictured in Fig. 15 and shown schematically in Fig. 16. The design allows rotation of the probe into the flow, ensuring an accurate total pressure reading.

Figure 4 shows the location of the measuring planes within the model. Pressure taps measure static or total pressure depending on their location. In each of the planes Z, B, C and E are arranged 8 equally spaced static taps. Planes Y and G each have 8 equally spaced total taps. Planes A and F have 4 static and 4 total taps, spaced alternately. Plane H has 12 equally spaced static taps. Plane X contains no taps, but the pressure can be accurately predicted at

this location. Total and static pressures are measured at selected injector nozzles in plane I by the probes shown in Fig. 17. These probes, having a 15-deg. chamfer at the inlet, were designed to measure total pressure of flows with yaw angles up to 20 deg. From Vavra's results it was suspected that the flow did not leave each injector axially. Therefore the new probe assembly was designed to permit quick adjustment to reach the condition depicted in Fig. 18. Total and static pressures at seven locations within the second annulus were obtained by inserting a removable probe which could be oriented into the direction of flow. All pressure taps were connected to the manometer bank by plastic tubing and measured against atmospheric or plenum pressure depending on the test configuration.

Testing of the return sub-assembly required a modification of the installation. An adapter fitted with screens, shown in Fig. 20, was mounted on plenum 2. Attached between the adapter and the sub-assembly was a ring of 52 inlet nozzles to introduce the flow uniformly to the orifice ring. Plane D, only used with this configuration, has 4 pressure taps. Because flow is essentially stagnant within the adapter, it is assumed that $P_D = P_{t_D}$. A view of this test installation, without the pressure taps connected, is shown in Fig. 21.

The inlet pressure for both configurations was remarkably steady and, except where noted, the pressures within the model did not fluctuate more than ± 0.5 cm. of water even at the highest flow rates.

SECTION 4

THEORETICAL CONSIDERATIONS

If a steady incompressible, adiabatic, viscous flow exists in a pipe, Bernouilli's equation between two points on a streamline can be written as

$$(144)P_1 + \rho \frac{v_1^2}{2g} + \rho z_1 = (144)P_2 + \rho \frac{v_2^2}{2g} + \rho z_2 + h_{L\ 1-2} \quad (1)$$

where:

P = static pressure (lb/in²)

ρ = density (lb_m/ft³)

v = velocity (ft/sec)

g = 32.17 (ft/sec²)

z = height above reference (ft)

h_L = head loss (lb/ft²)

Since the first three terms on each side of equation (1) represent the total pressure, the head loss is equal to the total pressure loss $\Delta P_{t\ 1-2}$ in the pipe.

Experience shows that this loss can be expressed by the function

$$\Delta P_{t\ 1-2} = f(\rho, \mu, v, l, d, e) \quad (2)$$

where: μ = viscosity (lbsec/ft²)

l = characteristic length (ft)

d = characteristic diameter (ft)

e = roughness parameter based on average variation of inside radius (ft)

Buckingham's π theorem⁷ states that the number of independent dimensionless groups used to describe a phenomenon with n variables is equal to $n-r$ where r is the number of basic dimensions. For

the basic dimensions of force F, length L, and time T, a dimensional analysis of equation (2) gives

$$\frac{\Delta P_{t_{1-2}}}{\rho v^2/g} = f \left\{ \frac{\rho v d}{\mu}, \frac{l}{d}, \frac{e}{d} \right\} \quad (3)$$

Equation (3) has four independent parameters

$$\frac{\Delta P_{t_{1-2}}}{\rho v^2/g} = \text{Euler number}$$

$$\frac{\rho v d}{\mu} = \text{Reynolds number} = \text{Re}$$

$$\frac{e}{d} = \text{relative roughness}$$

$$\frac{l}{d} = \text{geometrical factor}$$

Usually equation (3) is expressed by

$$\Delta P_{t_{1-2}} = \zeta \frac{l}{d} \frac{\rho v^2}{2g} \quad (4)$$

where ζ is the friction loss coefficient that depends on the relative roughness and Re. In pipe flow with Re higher than about 10^6 the coefficient ζ remains essentially constant. In addition, the so-called momentum loss occurs if pipes have either sudden contractions or expansions. It is primarily due to eddying turbulence and has been found experimentally to satisfy the relation

$$\Delta P_{t_{1-2}} = \lambda \frac{\rho v^2}{2g} \quad (5)$$

where λ is the momentum loss coefficient which depends primarily on flow geometry and remains practically independent of Re.

In a flow channel where frictional and momentum losses occur, the two loss coefficients may be combined to give

$$\Delta P_{t_{1-2}} = \psi \rho \frac{V^2}{2g} \frac{l}{d} \quad (6)$$

where ψ is a total loss coefficient which depends on Re. If Re is sufficiently high, the coefficient ψ is a function of geometry alone.

The analysis can be extended to systems of flow passages by considering an equivalent pipe for which equation (6) is valid. If such a system is modeled to scale, the factors ψ and $\frac{l}{d}$ are contained in one loss coefficient ξ . For air as a testing fluid, care must be taken to maintain low Mach numbers M in the model as equation (6) holds for incompressible flows only.

For air at low M and with the velocity V_1 at point 1 as a reference

$$V_1 = \frac{\dot{w}}{\rho A_1} \quad (7)$$

where: \dot{w} = flow rate (lb_m/sec)

$$A_1 = \text{area (ft}^2\text{)}$$

Equation (6) may then be written as

$$\Delta P_{t_{1-2}} = \frac{1}{2} \xi_{1-2} \frac{\dot{w}^2}{\rho A_1^2} \quad (8)$$

Using the equation of state for a perfect gas

$$\rho = \frac{P_{t_1} (144)}{RT_{t_1}} \quad (9)$$

$$\text{where } R = 53.35 \frac{\text{ft-lb}}{\text{lb}_m^{\circ}\text{R}}$$

$$T_{t_1} = \text{total temperature } (^{\circ}\text{R})$$

equation (8) becomes

$$\frac{\Delta P_{t_{1-2}}}{P_{t_1}} = \frac{1}{2gA_1^2} \int_{1-2} \left[\frac{P_{t_1}^2}{RT_{t_1}} \right] \dot{w}^2 \quad (10)$$

The so-called equivalent flow rate referred to total conditions at 1 is defined by

$$w_{1T}^* = \frac{\dot{w} \sqrt{T_{t_1}}}{P_{t_1}} \sqrt{\frac{R}{g}} \quad (\text{in}^2) \quad (11)$$

Equation (10) then becomes

$$\frac{\Delta P_{t_{1-2}}}{P_{t_1}} = k_{1-2} \left\{ w_{1T}^* \right\}^2 \quad (12)$$

$$\text{where } k_{1-2} = \int_{1-2} \frac{1}{2A_1^2} \quad (\text{in}^{-4})$$

w_{1s}^* will be defined as the equivalent flow rate referred to static conditions. Unless otherwise stated w^* refers to total conditions.

For a liquid of specific weight γ_L (lb/ft³) equation (6) becomes

$$\Delta P_{t_{1-2}} = \frac{1}{2} \int \frac{\dot{w}^2}{gA^2 \gamma_L} \quad (13)$$

Regrouping terms

$$\Delta P_{t_{1-2}} = k_{1-2} \frac{\dot{w}^2}{g \gamma_L} \quad (14)$$

Determination of k_{1-2} by air tests of a model makes it possible to predict pressure losses in a unit for particular fluids at a given flow rate.

Prior to the application of this theory to the ARES model it was decided to construct an arbitrarily shaped flow passage which could be tested with air and water varying Re and M . This passage, which is shown in Fig. 22, has both friction and momentum losses. It was designed to operate in the same Re range for both fluids. Its inlet and discharge areas are equal to 4 sq. in. At the inlet is fitted a contoured nozzle to minimize entrance losses into the first section of the pipe. Internally the model has a sudden expansion, a flow straightener, and a sudden contraction. The minimum flow area of 2.23 sq. in. occurs in the flow straightener.

Air was obtained from the installation previously described. The model was attached to plenum 2, as shown in Fig. 23. Inlet total pressure is measured by the Kiel probe, and inlet temperature was taken as that measured in plenum 2. Discharge pressure $P_{t_{dis}}$ was measured by one of the probes shown in Fig. 17. Since conditions at the discharge were found to be nearly uniform, except in close proximity to the walls of the pipe, the average of five traverse points was taken as $P_{t_{dis}}$. Static pressure P_{dis} was taken to be atmospheric.

Values of k_{in-dis} , inlet to discharge pressure loss coefficient, were established for Re (based on d_{in}) between 1.58×10^5 and 3.67×10^5 and are plotted in Fig. 24 with the curve giving the best fit through the data points. Variation of k_{in-dis} is from -0.042 to $+0.057 k_{avg}$. Higher values of Re could not be reached due to a limiting manometer height. The highest Mach number M , obtained at the

discharge as determined by the static to total pressure ratio, was 0.28. A slightly higher M was undoubtedly present in the flow straightener.

Figure 25 shows the test installation for the water tests of this model. At the 4 in. discharge of a fire hydrant were available about 400 gal. H_2O /min. at a pressure of 50 psia. After steady flow was reached, the discharge was deflected to fill a 50 gallon drum. By weighing the drum before and after each run and knowing the elapsed time, the flow rate was found. Inlet static pressure P_{in} was measured just after the entrance nozzle by a 50 psig. pressure gage.

Values of k_{in-dis} were calculated for Re between 1.33×10^5 and 4.88×10^5 for 4 separate runs. The method of data reduction is given in Appendix B, and the results are shown in Fig. 24. Except for a few points there is excellent agreement between water data and the curve established by the air test. A maximum deviation of 10 per cent is noted while most points fall within 2 per cent of the curve obtained from the air tests. At both extremes of the Re spectrum the pressure P_{in} tended to fluctuate, which accounts for some of the scatter in these areas. What occurs at higher Re is hard to predict although it appears that k_{in-dis} is tending to approach some constant value. Because of limitations imposed by the method used to collect and weigh water, the higher Re range could not be tested. If a flow measuring orifice were installed upstream of the model inlet so that high flow rates could be measured accurately, data at high Re could be obtained.

These tests prove that the use of equations (12) and (15) for the evaluation of the pressure loss coefficient for liquid flows from air tests is justified.

SECTION 5

DESCRIPTION OF TESTS

In addition to the two configurations of the ARES model and the flow channel mentioned previously, tests were made on a full scale model of a nozzle tube to determine a representative loss coefficient. Moreover, separate tests were made with a geometrically similar model of a tube section in the ARES model from plane W to plane X, simulating the nozzle tubes. These tests are described in the sequence they were made. Table I gives an index of the runs conducted. All raw data from these tests are on file with Professor Vavra at the Propulsion Laboratory.

5.1 Oxidizer Return Sub-assembly

In testing the oxidizer return sub-assembly, a total of six runs was carried out at Re between 0.868×10^5 and 1.343×10^5 referred to conditions just upstream of the flow measuring orifice. The maximum Re attainable was restricted by the height (250 cm) of manometer bank 1. As a result of Vavra's preliminary tests it was determined that a new discharge total probe assembly should be designed. Runs R1 and R2 were conducted without taking any measurements in discharge plane I. The new probe assembly shown in Fig. 17 was built, calibrated, and used first during run R3 where alignment and ease of adjustment were investigated. More complete data in plane I were taken during runs R4, R5 and R6. At each selected peripheral location the probes were aligned individually with the injectors. Although the readings were steady and accurate, the procedure was time consuming. It was therefore decided to use data from every third injector tube only.

Pressure taps were made in the annulus by drilling a 1/16 in. hole partially tapped with a 10-32 thread. If the portable probe shown in Fig. 19 was not inserted, these holes were plugged by screws. Because of wear on the threads in the plastic, conditions in the annulus were determined only for runs R3 through R6.

Pressures from plenum 2 downstream through plane H were measured on manometer bank 1 referenced to atmosphere. Pressure in plane I was measured on bank 3, also referenced to atmosphere. Because of the large number of tubes and the slight pressure fluctuations noticed during testing, Polaroid pictures were taken of bank 1 for more accurate data recording.

At locations 5, 6, 7 and 8 in plane H the pressures were observed to fluctuate considerably, especially at higher flow rates. The area of this unsteadiness is visible in Fig. 10. For runs R1 and R2 the fluctuation was dampened by clamping the pressure lines leading from these taps to the manometer bank. During runs R3 through R6 the clamps were removed and an average was taken between the maximum and minimum fluctuation. This method produced the same readings as with the clamps, but the fluctuations could now be observed.

The general procedure for conducting each run was as follows:

1. The micromanometers and thermocouples were zeroed and atmospheric pressure recorded.
2. The desired pressure in plenum 2 was set and the flow was allowed to stabilize.
3. Flow measuring data were recorded and a photograph of bank 1 was taken.
4. Plane I and annulus data were recorded.
5. Part 3 was repeated.

Because of the interesting velocity distribution in the discharge plane and the large pressure fluctuations at locations in plane H, attempts were made to observe the flow in the annulus visually. Different methods to introduce smoke had negative results. The first attempt used a 50 gallon drum within which a standard Navy MK-5 day signal flare was ignited. This particular flare produces about 15 minutes of a dense, slightly toxic, white smoke. The drum was connected directly to plenum 2 and pressurized so that the smoke would go directly into the plenum. At the discharge of the model there was arranged a device to pipe the flow out of the building. It was found that too much smoke was produced, and the mixing in plenum 2 was so complete that there was no streamline definition in the annulus. The flare produced enough heat to melt the rubber pressure seals in the drum, allowing toxic smoke to enter the room. For these reasons this attempt was abandoned in favor of introducing smoke directly into the annulus. Cigars soaked in mineral oil and paraffin were ignited in a small container which was pressurized. Lines from this container led to eight 1/16 in. diameter holes spaced around the entrance to the annulus. The smoke partially condensed in the lines and that part which entered the annulus diffused quite rapidly. Although streamlines were faintly discernible, they were of insufficient definition to observe the flow.

This latter method left a large residue of tar and nicotine in the model. With the air passing through water was introduced into the annulus to clean out this residue. It became evident then that water would work as a visualization fluid. The set-up shown in Fig. 21 consists of a manifold connected to a plastic liquid soap bottle. Water

colored by food dye was forced into the annulus through the top four holes by squeezing the soap bottle. This method was very successful and produced a flow picture of photographic quality. Motion pictures of runs R3 through R6 were taken using a Kodak Cine-Special II, 16 mm camera. Both black and white and color film were used at 64 frames per second. Runs R3, R4 and R5 were photographed in black and white using TRI-EX, ASA 120 film and a red filter. KODACHROME II, ASA 25, was used on runs R5 and R6.

5.2 Nozzle Tubes

The nozzle tubes were tested in the configuration shown in Fig. 26. Water was supplied by a 1.0 in. hose from a faucet where the pressure was higher than 50 psig. A total of 22 data points during two runs was taken between Re of 1.844×10^4 and 6.874×10^4 , referred to inlet diameter.

Static pressure was measured at the tube inlet by a 50 psig pressure gage accurate to within ± 0.1 psi. The flow discharged to atmosphere. For each data point the inlet pressure was set and the flow allowed to stabilize. Water was then collected in a five gallon bucket during a measured time. Data recorded were inlet static pressure, weight of water, and elapsed time. The maximum Re was obtained with the water supply fully open.

5.3 Geometrically Similar Model of Plane W to Plane X

A single tube from plane W to plane X was scaled up by a factor of 3.5 and tested with water by using the set-up shown in Figs. 27 and 28. Water was supplied through a 1 in. hose to a 24 in. length of 6 in. diameter pipe, at the bottom of which is installed a contoured nozzle to ensure smooth entry into the 1.05 in. diameter pipe section. For runs W1 and W2, the orifices A and B had diameters of 0.761 and

0.757 in., respectively. Prior to run W3 new orifices, each having a diameter of 0.714 in., were installed. A constant water level in the reservoir was maintained at all times, and the flow rate was controlled by regulating the water supply and the discharge valve. The Reynolds number Re , referred to inlet diameter, could be changed from 0.415×10^4 to 4.078×10^4 during the tests. The runs were conducted in the same manner as those for the nozzle tubes. The pressures at the 6 locations indicated in Fig. 27 were read from a manometer board referenced to atmosphere.

5.4 Discharge and Return Assembly

Based on the information from these water tests two new orifice plates, with holes of 0.204 in. diameter, were installed in the ARES model. A total of five runs, R7 through R11, was carried out at Re , referred to the 4 in. supply pipe, between 0.917×10^5 and 1.32×10^5 . Pressures from plenum 2 downstream through plane B were measured on bank 1 referenced to plenum 2. Bank 2, referenced to atmosphere, measured pressures from plane C through plane H. Bank 3 was used again for plane I. The test procedures were similar to those used for the return sub-assembly. Two cameras were used to photograph manometer banks 1 and 2 simultaneously. No data was taken within the second annulus. Total pressure in plane Z was measured by the removable probe.

SECTION 6

RESULTS AND DISCUSSION

The oxidizer return sub-assembly was tested separately, mainly to investigate the velocity distribution in the discharge plane and the stability of the flow inside the return annulus. To a large extent these criteria determine the feasibility of the flow passage design. Assuming that fuel is pumped into the combustion chamber at plane I and distributed uniformly around the periphery, the importance of a uniform oxidizer distribution can be seen. The mixture of fuel and oxidizer will be rich or lean depending on whether the oxidizer flow is deficient or excessive. If the oxidizer discharge varies either with time or peripherally, and if it is not possible to meter the fuel accordingly, a non-uniform combustion will result. This condition is undesirable for two reasons. First, hot spots will result in the combustion chamber inducing thermal stresses in the combustion liner. Second, and more important, is the effect on turbine inlet conditions. The combustion chamber length is short, and non-uniform temperatures would have insufficient time to adjust prior to reaching the turbine inlet. A turbine blade then would pass through a non-uniform temperature field. An off-design condition would result and could have a detrimental effect on turbine performance. A major portion of the regenerative cooling in the ARES system occurs within the return annulus. The convective heat transfer in this annulus is totally dependent on the oxidizer flow pattern.

Since the return sub-assembly differs from the full model only upstream of plane E, it seems reasonable to assume that flow downstream

of this point will represent the conditions that will exist in the fully assembled model. Actually it was found that inlet conditions at plane E were essentially the same in both test configurations.

Data reduction for runs R1 through R6 is contained in Appendix C, part 2. The equivalent flow rate w_u^* referred to conditions at the flow measuring nozzle, and the values of Re just upstream of this point are listed in Table II. Appendix A gives the derivation of the flow measuring equations. Actual flow rate \dot{w} varies from $0.283 \text{ lb}_m/\text{sec}$ in run R3 to $0.449 \text{ lb}_m/\text{sec}$ in run R6. Also listed in Table II are average total pressures and equivalent flow rates at intermediate planes D, F and G found according to equation (C2). Losses between planes will be referred to one of these average inlet conditions.

It is important that the flow is distributed evenly around the periphery as it enters the model. In this case the procedure of averaging conditions at each plane can be justified. From water tests conducted by Vavra,⁴ on a geometrically similar model of a tube from plane D to plane X, an orifice discharge coefficient K was obtained. Vavra's model scaled the orifice size by a factor of 3.5 from 0.216 in. to 0.757 in. This discharge coefficient, analogous to αf_r of equation (A3), takes into account some of the difference between measured and actual flow rate. Figure 29 shows K plotted as a function of Re referred to tube inlet conditions. Values of K in Fig. 29 appear somewhat higher than those listed by ASME⁸ for a sharp edge orifice with $\beta = 0.7209$. This is quite reasonable when the different inlet conditions are considered. The ASME data are dependent on a minimum length of straight pipe upstream of the orifice. For Vavra's tests an inlet nozzle was present only ahead of the orifice. In later tests of

the same orifice with some length of pipe upstream, values of K were obtained which agreed more closely to those listed by the ASME.

The flow at plane D was found to be stagnated, and the pressure $P_D = P_{t_D}$ was uniform. At each measuring point in plane E an equivalent flow rate $w_{D_i}^*$ was found according to equations (C5) and (C6). Assuming that $w_{D_i}^*$ existed through each of the 52 orifices the peripheral flow distribution can be expressed by a factor F_i , where

$$F_i = \frac{(52) w_{D_i}^*}{w_D^*} \quad (15)$$

The total equivalent flow rate w_D^* is given in Table II. Tables III and IV list values of F_i in addition to intermediate quantities used in the calculation. Figure 31 is a plot of F_i as a function of peripheral location for R1 through R6. Looking downstream the angle is measured counterclockwise with $\Theta = 0$ deg. corresponding to the three o'clock position. In each instance the flow distribution is almost identical. The maximum deviation of this average F_i from $F_i = 1.0$ occurs in run R3 where the lowest Re was encountered. It was observed that most of the questionable data obtained during these tests occurred at the lower Re where the measuring accuracy is lower. Generally each curve has two peaks and two valleys indicating a deficiency of flow at $\Theta = 110$ deg. and 300 deg., and an excess at $\Theta = 0$ deg. and 225 deg. This is a relatively symmetric condition with the maxima appearing about 180 deg. apart. Because of this somewhat regular occurrence the values of F_i at $\Theta = 90$ deg. for runs R3 through R6 are questionable. Not to be overlooked, however, is the fact that the maximum deviation from $F_i = 1.0$ is only 4 per cent. This fact tends to

establish the accuracy of Fig. 29 and to substantiate that flow enters the oxidizer return sub-assembly uniformly.

Figure 30, also plotted from Vavra's water tests, shows f_{D-X} , the loss in total pressure from plane D to plane X divided by the static pressure change across the orifice, as a function of Re. The total pressure P_{tX} at plane X is found according to equation (C8). With this pressure and the inlet conditions at plane D, the coefficient k_{D-X} was calculated for each peripheral location. An average value \bar{k}_{D-X} for each run was found which is shown in Tables III and IV. It should be noted that at any peripheral location the value of k_{D-X} differs from \bar{k}_{D-X} by not more than five per cent.

If, as was hypothesized, the losses in this section are independent of Re, then k_{D-X} should not vary from point to point. This may be shown by referring to equation (12) and recognizing that both ΔP_{D-X} and $w_{D_i}^{*2}$ depend essentially on ΔP_{D-E} . The distribution of k_{D-X}/\bar{k}_{D-X} follows the same pattern as that established for F_i . This is shown in Fig. 31 for R1 and R2 and holds for the other runs also. Since $w_{D_i}^*$ is proportional to Re in accordance with equation (C6), the loss coefficient is also proportional to Re.

Experimentally obtained values of the friction factor proportional to k as a function of Re and relative roughness are shown in Fig. 32 for two different conditions of flow in pipes. These curves were taken from Schlichting.⁹ For the artificially roughened pipe of Fig. 32(a) the friction factor increases with Re to approach a constant value, whereas for the commercial pipe of Fig. 32(b) the factor decreases with Re toward a constant value. In the former case the pipes tested were lined with protuberances which penetrated completely through the

laminar sub-layer of the boundary layer. A large part of the friction is then due to a form drag which can be thought of as a momentum loss. In the second case skin-friction alone accounts for the friction factor. As relative roughness is increased in both cases the friction factor reaches a constant value at a lower Re. Realizing that in the present model test each tube from plane D to plane X is machined to at least the equivalent of commercial roughness and that k_{D-X} increases slightly with Re, it can be concluded that the momentum loss created by the orifice predominates. Tables III and IV show values of Re corresponding to the general transition range of Fig. 32. The loss coefficient k_{D-X} would become constant if either more momentum loss were introduced or if Re were increased.

Incompressible flow is a basic assumption of the theory proposed for this analysis. It seems reasonable to assume that the highest Mach number M in the model exists at the minimum flow area which occurs at the vena-contracta downstream of the orifice plate. At plane E an average area restriction factor $\bar{\phi}_E$ was found using equations (C9) through (C13). Also calculated were average values of \bar{P}_E , \bar{P}_{tE} and \bar{M}_E . Table V lists these values for runs R1 through R6. Applying the values of $\bar{\phi}_E$ to a flow area at plane E of 3.676 sq. in. gives an effective flow area varying from 2.081 sq. in. to 2.161 sq. in. The next largest area in the model is the 3.138 sq. in. area at plane I, where an average \bar{M}_I was calculated and is listed in Table V. For all runs the highest M in the model occurs at plane E, reaching a maximum value of 0.34 in run R6. Hence it is permissible to assume that the flow is essentially incompressible.

Table V also lists values of average loss coefficients from planes D to F, F to G, G to I and X to F. The latter loss is given by

$$\bar{k}_{X-F} = \bar{k}_{D-F} - \bar{k}_{D-X} \quad (16)$$

From Fig. 30 are obtained values of f which can be used to predict \bar{P}_{t_X} , and hence \bar{k}_{D-X} , whereas the values \bar{k}_{D-F} are calculated from test data. The magnitude of \bar{k}_{X-F} is small because of the small distance between the two planes. It can be said, therefore, that the method used to establish Fig. 30 is a valid one.

The peripheral distribution of k_{D-F}/\bar{k}_{D-F} is shown in Table VI. Except for a few isolated values, k_{D-F} is contained within 2 per cent of \bar{k}_{D-F} . Referring to the previous discussion, concerning the relationship between equivalent flow rate and loss coefficient, it can be assumed that the flow is distributed uniformly at plane F.

The situation is different in plane G. Figure 33 shows the peripheral distribution of k_{F-G}/\bar{k}_{F-G} . Since the pressure tap at $\Theta = 0$ deg. was damaged, a curve was faired in to give an estimated value at this location. Except for runs R3, at low Re, a definite pattern can be observed. A minimum loss coefficient occurs at $\Theta = 180$ deg. This indicates an irregularity of the flow at this peripheral location. This situation can be explained from the geometry of the flow passages. Figure 34 shows the intersection of the two cylinders with the positions of Θ in plane G indicated. At $\Theta = 90$ deg. and 270 deg. the flow has an easier path to follow, therefore one would expect a higher flow rate at these points and hence a higher value of loss coefficient. However, at $\Theta = 0$ deg. the flow enters the return annulus on top of the holes in plane H. It will be shown that the primary injectors at

this location pass a higher percentage of the discharge flow. It is entirely reasonable then that the flow is deficient as it enters the annulus from $\theta = 135$ deg. to $\theta = 225$ deg.

Table VII lists values of loss coefficient k_{G-H} for each location in plane H and \bar{k}_{G-H} for runs R1 through R6. Also shown in Table VII are values of \bar{k}_{H-I} for runs R3 through R6, found by

$$\bar{k}_{H-I} = \bar{k}_{G-I} - \bar{k}_{G-H} \quad (17)$$

Shown in Fig. 35 are values of average loss coefficients between different stations of the model as a function of Re. The increase with Re of \bar{k}_{D-X} has already been explained, however, the maximum and minimum values are only 92 and 104 per cent of the average value, respectively. The highest value which \bar{k}_{D-X} approaches at increased Re is probably around 0.125. If loss coefficients in the low Reynolds number range are not considered, the average losses from plane X throughout the remainder of the model are remarkably constant.

Velocity distribution in the discharge plane is found according to equations (C15) and (C16). Figure 36 shows a drawing of plane I from the discharge side and the relative position of the pressure taps in plane H. Table VIII lists values of V_1/\bar{V} for each of the surveyed locations for runs R3 through R6. An average of positions A, B and C was calculated at each location 1 through 57. This average velocity distribution is plotted in Figs. 37 through 40. The velocity distribution and hence the flow distribution is essentially independent of Re. The excessive flow from locations 54 through 10 was anticipated from the conditions existing at $\theta = 0$ deg. in plane G. The erratic condition from locations 24 through 36 will be explained later. It is not

understood why the flow is deficient around location 48. Data at the seven locations within the annulus obtained from the removable probe were entirely unreliable. The model had been dropped causing damage to the plastic threads and making it virtually impossible to prevent leakage.

The flow within the return annulus can best be described by referring to the results of the flow visualization efforts previously described. It has been shown that the flow in plane G is symmetrical about the $\theta = 0$ deg. and $\theta = 180$ deg. axis. Therefore, the annulus is naturally split into a top and bottom half in each of which the same flow pattern should exist. Water introduced in the lower half had a tendency to pool at the lowest point because of gravity effects, whereas all the water introduced in the top half was carried out of the model. For these reasons and because of problems associated with photographing the flow conditions, it was decided to investigate only the upper half of the annulus. Figure 41 is a drawing of that half annulus, developed into a plane, showing the locations where water was introduced. In addition, data obtained by Vavra⁴ are shown that give flow directions at locations within the annulus. These flow directions are represented by arrows in Fig. 41. Figure 42(a) through (h) and Fig. 43(a) through (h) are photographs taken of runs R4 and R5, respectively. The upper half of the annulus is shown as the upper 3/4 of each picture. These pictures were made from single frames of 16mm movie film taken at 64 frames per second. Each sequence spans one second of operation with a time between each pattern of 0.125 sec. Figure 42 is typical of the flow pattern at $Re = 1.028 \times 10^5$ and lower, whereas Fig. 43 is representative of the conditions at $Re = 1.177 \times 10^5$ and higher. Several

similarities exist at all Re. Most apparent is the extreme instability in the region of plane H where the flows from the top and bottom halves of the annulus mix. This region is exactly that in which the pressure taps H5, H6, H7 and H8 are located.

It should be noted that this is the only region in the model where the pressures were unsteady. Several vortices are present in this general area. The pattern is apparently being triggered by a huge separation from the turning vane near H5. Although not entirely obvious from the sequence of pictures, it was observed that these vortices went through a periodic variation in both intensity and location. At best, it can be said that the flow in this area is thoroughly confused and that this situation is most likely the cause of the cyclic velocity distribution in plane I which is evident from Figs. 37 through 40. It has been noted also that a deficiency of flow exists at the far right of the annulus. This portion of the annulus is supplied by the $\theta = 180$ deg. location of plane G where the deficiency of flow has already been observed. The most striking difference between Fig. 42 and Fig. 43 is the appearance in the latter of a huge vortex in the upper right hand portion of the annulus. It is believed that this vortex is caused by a flow separation from the turning vane immediately upstream of it. A 100 ft. roll of color film taken of runs R5 and R6 was left intact, and is on file with Professor Vavra.

From the above discussion and the flow visualization studies, it is possible to make a qualitative design evaluation of this portion of the ARES assembly. The test data at the higher Re will best simulate actual operation, although this distinction appears necessary only when considering conditions within the annulus. Heat transfer will most

certainly be hampered where vortices exist, since the same flow particles will tend to circulate in one spot instead of passing through the model. Hot spots could result in these regions. The deficiency of flow in the region farthest from plane H would have the same effect on heat transfer, only to a lesser extent. Elimination of these flow instabilities, in addition to improving heat transfer characteristics, would serve to reduce the losses from plane G to H and to distribute the discharge velocity more uniformly. One method of accomplishing this would be to redesign the turning vanes, making their shape conform more to airfoil cross sections cambered in the direction in which the flow is to be turned. For stress considerations, the contact surface area with the outer annulus would have to be maintained. Another scheme would be to replace the relatively large number of turning vanes with a few long flow dividers. It is felt that a large portion of the instability occurs as a result of the mixing of flows from each half of the annulus, and for this reason the arranging of a flow splitter is recommended.

The loss coefficients calculated during the tests of the return sub-assembly were duplicated when the full model was tested and will be discussed later in this report. Before proceeding with the tests of the entire unit, it was decided to determine how closely the pressure drop in the model, from plane W to plane X, simulated that in the actual nozzle tubes. Results of tests on the nozzle tube are listed in Table IX. The method of data reduction is shown in Appendix C, part 3. Loss coefficient ξ_{in-dis} is plotted as a function of Re in Fig. 44. Fluctuation of the pressure gage was as much as ± 0.5 psig. At low values of Re, where pressures were of the order of 3.5 psig., this

fluctuation could cause the computed ξ to vary between 11.1 and 8.5. Therefore, the dashed portion of the curve of Fig. 44 is questionable. The decrease of ξ with Re is quite evident, and by applying the rationale previously described, it seems that skin friction accounts for the major portion of the loss. Because of the scale chosen for ξ in Fig. 44 its variation appears magnified. Actually ξ only deviates ± 6 per cent from an average value of 10.3. The range of Re encountered falls well within the transition range for pipes as shown in Fig. 32.

Data from tests on the geometrically similar section of plane W to plane X were reduced by the method outlined in Appendix C, part 4. These tests were conducted similarly to those run by Vavra for which the validity has been established. Table X lists values of f_{1-6} , ξ_{1-6} and the orifice discharge coefficients, in addition to other quantities of interest. Points 1 and 6 refer to planes W and X respectively. Figure 45 shows f_{1-6} and ξ_{1-6} for runs W1 and W2, plotted as a function of Re. The loss coefficient ξ_{1-6} differs by almost a factor of 2 from ξ_{in-dis} of the nozzle tubes. This condition is unsatisfactory because the largest loss in the entire assembly occurs in these tubes and the water model with orifice plates of $d = 0.757$ in. and 0.761 in. gave half of this loss only. It is also interesting to compare the values of K (0.757) with those obtained by Vavra. The values differed on an average by almost 6 to 7 per cent. The difference in the discharge coefficient is due to the influence of the inlet conditions.

Table XI also lists the results of run W3 with orifice diameters of 0.714 in., whereas Fig. 46 shows ξ_{1-6} and f_{1-6} as functions of Re. It appears as if this orifice diameter more nearly simulates conditions in the nozzle tube. From the test of the fully assembled model,

values of ξ_{W-X} were computed as outlined in Appendix C, part 5, equations (C32) to (C36). Figure 47 shows these values together with the curve obtained from the water tests of the nozzle tubes. The difference in inlet conditions to plane W when the section is installed in the model could account for the differences between ξ_{W-X} and ξ_{1-6} . Apparently though the orifice size of 0.714 in. does the best job of simulation.

Tests of the complete assembly of Fig. 4 were conducted mainly to establish values of loss coefficients without making pressure or velocity surveys. The methods of data reduction are similar to those used for the return sub-assembly and are contained in Appendix C, part 5. Table XII gives the data for the flow rate determined, together with average total pressures and equivalent flow rates in planes Z, A, F and G. Data at plane Y indicated a lower total pressure than that occurring in plane A. This impossible situation must be due to inaccurate measurement in plane Y. These data were therefore disregarded. Average loss coefficients from planes Z to A, A to F, F to G, G to H, H to I and W to X are listed in Table XII for runs R7 through R11.

The range of Re encountered in the 4 inch supply pipe, and in the model at plane E, was the same as for the return sub-assembly alone, as was the value of discharge Mach number \bar{M}_1 . Arranging the discharge sub-assembly ahead of the return sub-assembly does not disturb the peripheral velocity distribution that was observed in the return sub-assembly alone. Table VI lists values of $k_A = F/\bar{k}_A - F$ which differ from a value of 1.0 by a maximum of 0.005. The distribution of loss coefficients from plane F to plane G is shown in Fig. 48. It is almost identical to that from runs R1 through R6. Velocity distribution in

plane I was also found to agree precisely with that determined previously. From the foregoing it is reasonable to conclude that the discussion of results for the return sub-assembly is applicable to the entire model.

Figure 49 shows the average loss coefficients as a function of Re. The scatter of \bar{k}_{Z-A} occurs because the total conditions at plane A were measured at only one location, hence a true average could not be obtained. However, this condition is not serious because this loss is only a small percentage of the total loss. The total loss coefficient \bar{k}_{Z-I} is obtained by adding the coefficients between intermediate planes. If only the conditions in planes Z and I are considered, a value \bar{k}_{Z-I}' is obtained which differs from \bar{k}_{Z-I} . As Re is increased $\bar{k}_{Z-I}/\bar{k}_{Z-I}'$ goes from 0.974 to 0.948. Evidently there exists a slight effect of compressibility. The difference in the two loss coefficients may be shown mathematically. Assume, for example, that the loss coefficient between planes Z and F is to be determined. The overall coefficient may be expressed as

$$\bar{k}_{Z-F}' = \frac{1}{\bar{w}_Z^2 \bar{P}_{tZ}} \left\{ (\bar{P}_{tZ} - \bar{P}_{tA}) + (\bar{P}_{tA} - \bar{P}_{tF}) \right\} \quad (18)$$

Using the relation

$$\bar{w}_Z^2 \bar{P}_{tZ} = \bar{w}_A^2 \bar{P}_{tA} \quad (19)$$

equation (17) becomes

$$\bar{k}_{Z-F}' = \bar{k}_{Z-A} + \frac{\bar{P}_t}{\bar{P}_{tA}} \bar{k}_{A-F} \quad (20)$$

Since total pressure must decrease from plane to plane, the pressure ratio $\bar{P}_{tZ}/\bar{P}_{tA}$ must be larger than unity. Hence, equation (20) shows that \bar{k}_{Z-F}' will always be larger than \bar{k}_{Z-F} . The total loss coefficient from plane Z to plane I can be expressed by

$$\bar{k}_{Z-I}' = \bar{k}_{Z-A}' + \bar{k}_{A-F}' + \bar{k}_{F-G}' + \bar{k}_{G-H}' + \bar{k}_{H-I}' \quad (21)$$

where

$$\bar{k}_{A-F}' = \frac{\bar{P}_{tZ}}{\bar{P}_{tA}} \bar{k}_{A-F} \quad (\text{etc.})$$

Equation (21) was used to compute \bar{k}_{Z-I}' for runs R6 through R11. The values were found to be identical to those obtained from

$$\bar{k}_{Z-I}' = \frac{\Delta \bar{P}_{tZ-I}}{\bar{P}_{tZ}} / (\bar{w}_Z^*)^2 \quad (22)$$

Consider the section from plane G to plane H only. Figures 35 and 49 show that the loss coefficient as a function of Re, if based only on inlet conditions at plane G, is the same for both the return sub-assembly and the fully assembled model. If the method of equation (21) were applied, it can be seen that \bar{k}_{G-H}' would increase as more sections were added to the model upstream, because for the same inlet conditions at plane G, namely, \bar{P}_{tG} and \bar{w}_G^* , the pressure ratio $\bar{P}_{tZ}/\bar{P}_{tG}$ would increase. This method actually refers all loss coefficients back to the initial inlet conditions and assumes incompressible flow from, say, plane Z to plane H. Using \bar{k}_{G-H} to represent the loss, effectively cancels any errors introduced by the incompressible assumption for flows upstream. Only in that portion of the model from

G to H is incompressible flow assumed. For this reason, it was decided to use the above-mentioned simple method for computing total loss coefficients. As an extension of this reasoning, the writer believes that more accurate estimates of loss coefficient could be obtained by adding more intermediate measuring planes. It is questionable whether this complication is justified since the maximum difference between \bar{k}_{Z-I} and \bar{k}'_{Z-I} is only 5.2 per cent.

From Fig. 49 the coefficient \bar{k}_{Z-I} appears to approach a value of about 0.62 of which 66 per cent is from plane W to plane X. As an example it will be assumed that the flow rate of the oxidizer \dot{w} is 100 lb_m/sec and that its specific weight γ_L is 75 lb/cu. ft. The total pressure drop $\Delta P_{t_{Z-I}}$ in the oxidizer passage from the pump discharge to the entrance into the primary combustion chamber is then from equation (14)

$$\Delta P_{t_{Z-I}} = \bar{k}_{Z-I} \frac{\dot{w}^2 (144)}{g \gamma_L} \quad (\text{lb/in}^2) \quad (23)$$

$$\text{where: } \bar{k}_{Z-I} = 0.62 \quad \text{in}^{-4}$$

$$g = 32.17 \text{ ft/sec}^2$$

or

$$\Delta P_{t_{Z-I}} = \frac{0.62 (100)^2 (144)}{(32.17) (75)} = 370 \text{ lb/in}^2 \quad (24)$$

SECTION 7

CONCLUSIONS

The average loss coefficient from a position just downstream of the oxidizer pump to the discharge of the primary injectors is 0.62. This experimentally determined coefficient should remain nearly constant near the specified operating range since the anticipated Reynolds number is sufficiently high. The model section from plane W to plane X with 2 orifice plates, having holes of $d = 0.204$ in., represents the actual nozzle tubes. The pressure loss coefficient found in the air test of this model section agreed closely with the coefficient determined from the water test of the tubes. The peripheral distribution of flow within the model is very nearly uniform until it enters the annulus. Here the flow becomes deficient in a 45 deg. sector centered on $\theta = 180$ deg. in plane G. This causes a deficiency of flow in that portion of the return annulus farthest from plane I.

Because of compressibility effects a difference exists between loss coefficients determined from inlet and discharge conditions only, and those obtained by a summation of the intermediate loss coefficients between adjacent planes. The flow channel used to check the basic theory by water and air tests was neither designed nor instrumented with this difference in mind. It would be of interest to construct a more complicated system of flow passages for this purpose and to investigate the effect of compressibility more fully. It is believed by the writer that more intermediate planes where exact conditions can be established will lead to more accurate estimations of loss coefficient.

Due to the fact that the major portion of the pressure drop is caused by momentum losses, it would be inconsistent to apply standard

theories that relate heat transfer to pressure drop with the objective of evaluating the heat transfer coefficients at different locations in the flow passages. However, the vortices within the return annulus, as evidenced by the photographs of the existing flow pattern, will certainly be detrimental to heat transfer in this region. These vortices could be largely eliminated by changing the design of the turning vanes and installing a flow divider where mixing now occurs between flows from the top and bottom of the annulus.

Model tests of this type provide a natural bridge between the completion of a design and the building of a prototype. It is estimated that a cost factor of 20 to 1 exists between the actual hardware of the ARES unit and its corresponding flow model. Prediction of the pressure loss coefficients of complicated passages analytically is, at present, an impossible task. Except for the slight effects of Reynolds number, the experimental method of predicting pressure loss coefficients presented in this paper is both valid and accurate.

TABLE I
INDEX OF RUNS

<u>RUN NUMBER</u>	<u>TEST DESCRIPTION</u>
RM1	Air test of flow device
RMW1, RMW2, RMW3, RMW4	Water test of flow device
R1, R2, R3, R4, R5, R6	Air test of oxidizer return sub-assembly
W1, W2	Water test of geometrically similar model plane W to plane X, orifice plates of $d = 0.761$ in. and $d = 0.757$ in.
W3	Same as W1 and W2 with orifice plates both of $d = 0.714$ in.
WV1, WV2, WV3	Water tests of geometrically similar model plane W to plane X
R7, R8, R9, R10, R11	Air tests of full ARES assembly

TABLE II
OXIDIZER RETURN SUB-ASSEMBLY, INLET ORIFICE
DATA AND EQUIVALENT FLOW RATES

RUN AVERAGE OF ALL DATA POINTS	R1	R2	R3	R4	R5	R6
P_{atm} (lb/in ²)	14.768	14.768	14.778	14.778	14.792	14.734
P_u (lb/in ²)	17.758	17.550	16.094	16.746	17.437	18.147
Δh_o (in H ₂ O)	1.998	1.887	0.971	1.380	1.776	2.221
T_u (°R)	539.0	539.7	540.5	541.0	552.0	551.5
T_{plen} (°R)	534.7	535.3	536.0	542.0	550.5	549.5
$Re(10^{-5})_d = 4.07''$	1.307	1.262	0.868	1.028	1.177	1.343
w_u^* (in ²)	.71785	.70176	.52655	.61562	.68344	.74901
P_D (lb/in ²)	17.708	17.490	16.058	16.699	17.367	18.061
\bar{P}_{t_F} (lb/in ²)	16.510	16.385	15.546	15.926	16.323	16.704
\bar{P}_{t_G} (lb/in ²)	16.227	16.122	15.427	15.738	16.073	16.383
w_D^* (in ²)	.71732	.70137	.52558	.61799	.68534	.75132
\bar{w}_F^* (in ²)	.76914	.74870	.54291	.64797	.72918	.81237
\bar{w}_G^* (in ²)	.78254	.76088	.54708	.65574	.74051	.82829

TABLE III
FLOW DISTRIBUTION THROUGH ORIFICE PLATE,
LOSS COEFFICIENT PLANE D TO PLANE X

RUNS R1, R2, R3

Location	1	2	3	4	5	6	7	8
R1 $w_D^* = .71732$, $K = .79$, $\bar{P}_{t_X} = P_D - .50 \Delta P_{D-E} = 1161.4$								
$P_D - P_E$ (Cm H ₂ O)	163.10	159.40	155.05	151.80	159.50	163.10	159.10	158.45
$Re(10^{-4})$ $d=0.3$	3.503	3.468	3.426	3.391	3.468	3.503	3.466	3.458
$w_{D_i}^*$ (in ²)	.01417	.01403	.01386	.01371	.01403	.01417	.01402	.01399
F_i	1.027	1.016	1.005	0.994	1.005	1.027	1.016	1.014
k_{D-X} (in. ⁻⁴)	.1273	.1244	.1210 avg.	.1185 .1239	.1245	.1273	.1242	.1237
R2 $w_D^* = .70137$, $K = .79$, $\bar{P}_{t_X} = P_D - .50 \Delta P_{D-E} = 1152.13$								
$P_D - P_E$ (Cm H ₂ O)	151.25	147.80	143.85	141.70	147.65	151.60	147.60	147.33
$Re(10^{-4})$ $d=0.3$	3.363	3.328	3.286	3.264	3.326	3.366	3.326	3.324
$w_{D_i}^*$ (in ²)	.01377	.01363	.01346	.01337	.01362	.01378	.01362	.01361
F_i	1.021	1.010	0.998	0.991	1.009	1.022	1.009	1.009
k_{D-X} (in. ⁻⁴)	.1250	.1221	.1188 avg.	.1171 .1217	.1220	.1252	.1219	.1217
R3 $w_D^* = .52558$, $K = .795$, $\bar{P}_{t_X} = P_D - .505 \Delta P_{D-E} = 1095.29$								
$P_D - P_E$ (Cm H ₂ O)	69.70	65.50	68.95	64.75	66.85	71.45	67.55	67.35
$Re(10^{-4})$ $d=0.3$	2.249	2.187	2.238	2.173	2.207	2.276	2.218	2.214
$w_{D_i}^*$ (in ²)	.01004	.00976	.00999	.00970	.00985	.01016	.00990	.00988
F_i	0.994	0.965	0.989	0.960	0.975	1.006	0.979	0.978
k_{D-X} (in. ⁻⁴)	.1128	.1060	.1116 avg.	.1048 .1096	.1082	.1156	.1093	.1090

TABLE IV
FLOW DISTRIBUTION THROUGH ORIFICE PLATE,
LOSS COEFFICIENT PLANE D TO PLANE X

RUNS R4, R5, R6

Location	1	2	3	4	5	6	7	8
R4 $w_D^* = .61799$, $K = .79$, $\bar{P}_{t_X} = P_D - .508 \Delta P_{D-E} = 1122.90$								
$P_D - P_E$ (Cm H ₂ O)	104.70	99.50	102.40	96.60	101.60	106.70	101.50	100.50
$Re (10^{-4})$ $d=0.3$	2.752	2.687	2.724	2.650	2.711	2.780	2.711	2.687
$w_{D_i}^*$ (in ²)	.01188	.01160	.01176	.01144	.01170	.01200	.01170	.01160
F_i	1.000	0.976	0.989	0.962	0.986	1.008	0.985	0.981
k_{D-X} (in. ⁻⁴)	.1185	.1127	.1160 avg.	.1094 .1151	.1150	.1208	.1149	.1138
R5 $w_D^* = .68534$, $K = .79$, $\bar{P}_{t_X} = P_D - .50 \Delta P_{D-E} = 1152.88$								
$P_D - P_E$ (Cm H ₂ O)	140.95	135.05	137.25	132.05	137.95	142.95	136.45	135.95
$Re (10^{-4})$ $d=0.3$	3.200	3.139	3.158	3.106	3.168	3.220	3.146	3.146
$w_{D_i}^*$ (in ²)	.01339	.01313	.0321	.01299	.01325	.01347	.01316	.01316
F_i	1.016	0.996	1.003	0.986	1.005	1.022	0.999	0.999
k_{D-X} (in. ⁻⁴)	.1228	.1177	.1196	.1151	.1202	.1246	.1189	.1185
R6 $w_D^* = .75132$, $K = .79$, $\bar{P}_{t_X} = P_D - .50 \Delta P_{D-E} = 1181.06$								
$P_D - P_E$ (Cm H ₂ O)	182.90	176.05	176.90	171.35	180.90	185.60	177.90	177.05
$Re (10^{-4})$ $d=0.3$	3.681	3.618	3.626	3.574	3.661	3.706	3.606	3.628
$w_{D_i}^*$ (in ²)	.01479	.01454	.01457	.01436	.01471	.01489	.01461	.01458
F_i	1.024	1.006	1.008	0.994	1.019	1.030	1.011	1.009
k_{D-X} (in. ⁻⁴)	.1275	.1228	.1233 avg.	.1195 .1245	.1261	.1294	.1240	.1234

TABLE V AREA RESTRICTION PLANE E, MACH # PLANES E, F & I, LOSS COEFFICIENTS PLANES D TO F, X TO F, F TO G & G TO I						
RUN	R1	R2	R3	R4	R5	R6
\bar{P}_{tE} (cm H ₂ O)	1169.33	1159.50	1096.98	1125.75	1155.63	1184.63
\bar{P}_E (cm H ₂ O)	1086.43	1082.89	1061.75	1072.87	1084.22	1091.77
\bar{M}_E	.32	.31	.21	.26	.30	.34
T_E/T_D	.979	.981	.991	.986	.982	.977
\bar{w}_E^* ST	.81367	.78919	.55660	.67181	.76516	.86410
$\bar{\phi}_E$.567	.571	.588	.582	.574	.570
\bar{P}_F (cm H ₂ O)	1148.37	1140.39	1087.82	111.81	1137.18	1161.11
\bar{P}_{tF} (cm H ₂ O)	1161.24	1152.46	1093.46	1120.18	1148.11	1174.90
\bar{M}_F	.12	.12	.08	.10	.12	.13
\bar{k}_{D-F} (in ⁻⁴)	.1309	.1285	.1166	.1212	.1280	.1331
\bar{k}_{X-F} (in ⁻⁴)	.0070	.0068	.0015	.0061	.0083	.0086
\bar{k}_{F-G} (in ⁻⁴)	.0293	.0288	.0261	.0284	.0290	.0295
\bar{P}_I (cm H ₂ O)			408.34	407.81	407.71	405.50
\bar{P}_{tI} (cm H ₂ O)			420.92	426.43	432.78	437.57
\bar{M}_I			.21	.25	.29	.33
\bar{k}_{G-I} (in ⁻⁴)			.0492	.0501	.0504	.0517

TABLE VI
PERIPHERAL DISTRIBUTION OF LOSS COEFFICIENT
PLANES A TO F AND PLANES D TO F

$\frac{K_{D-F}}{\overline{K}_{D-F}}$	RUN	Re(10^{-5})	F2	F4	F6	F8
	R1	1.307	0.986	0.989	1.038	1.001
	R2	1.262	0.987	0.991	1.017	1.004
	R3	0.868	0.967	0.997	1.012	0.987
	R4	1.028	0.978	1.002	1.017	1.002
	R5	1.177	0.978	1.002	1.016	1.003
	R6	1.343	0.980	0.998	1.016	1.006
$\frac{K_{A-F}}{\overline{K}_{A-F}}$	R7	0.917	0.998	0.996	1.003	1.003
	R8	0.935	0.998	0.996	1.003	1.003
	R9	1.117	0.997	0.998	1.002	1.003
	R10	1.276	0.997	0.997	1.001	1.004
	R11	1.320	0.997	0.997	1.007	1.005

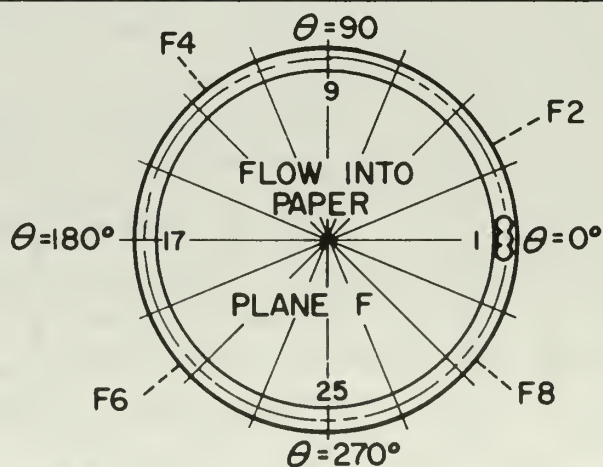


TABLE VII
LOSS COEFFICIENTS PLANES G TO H & H TO I
RUNS R1 THROUGH R6

LOCATION	PLANE	H	1	2	3	4	5	6	7	8	9	10	11	12
R1			33.60	28.04	25.99	23.64	26.49	23.04	24.39	36.44	26.09	26.29	29.14	36.79
			.0481	.0401	.0372	.0338	.0379	.0330	.0349	.0521	.0373	.0376	.0417	.0526
			$\bar{k}_{G-H} = .0405$											
R2			31.39	26.14	24.34	22.14	25.04	21.99	25.74	33.84	24.34	24.59	27.64	34.34
			.0478	.0398	.0371	.0337	.0381	.0335	.0392	.0515	.0371	.0374	.0421	.0523
			$\bar{k}_{G-H} = .0408$											
R3			15.50	13.20	12.35	11.45	15.20	11.85	14.45	14.70	12.30	11.95	13.70	17.45
			.0477	.0406	.0380	.0352	.0468	.0365	.0445	.0453	.0379	.0368	.0422	.0537
			$\bar{k}_{G-H} = .0421$											
			$\bar{k}_{H-I} = .0071$											
R4			22.49	18.99	17.79	16.39	23.89	16.69	18.89	21.24	17.79	16.99	19.59	25.39
			.0476	.0399	.0374	.0344	.0502	.0351	.0397	.0446	.0374	.0357	.0412	.0533
			$\bar{k}_{G-H} = .0413$											
			$\bar{k}_{H-I} = .0084$											
R5			29.49	25.09	23.34	21.39	30.39	21.79	25.99	27.39	23.09	22.49	25.94	33.34
			.0476	.0405	.0376	.0345	.0490	.0351	.0419	.0442	.0372	.0363	.0418	.0538
			$\bar{k}_{G-H} = .0416$											
			$\bar{k}_{H-I} = .0088$											
R6			37.41	31.71	29.46	27.06	38.31	27.61	31.31	36.81	29.26	28.51	32.96	42.76
			.0473	.0401	.0373	.0342	.0484	.0349	.0396	.0466	.0370	.0361	.0417	.0541
			$\bar{k}_{G-H} = .0414$											
			$\bar{k}_{H-I} = .0103$											

TABLE VIII
VELOCITY DISTRIBUTION $(\sqrt{q_i} / \frac{1}{n} \sum_{i=1}^n \sqrt{q_i})$, PLANE I

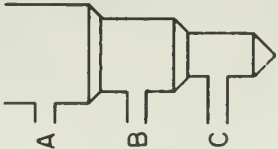
POSITION LOCATION		R3			R4			R5			R6		
		A	B	C	A	B	C	A	B	C	A	B	C
1		1.062	1.067	1.086	1.074	1.049	1.064	1.078	1.085	1.085	1.078	1.083	1.077
3		1.029	1.059	1.074	1.062	1.048	1.062	1.044	1.057	1.074	1.049	1.050	1.080
6					1.043	1.064	1.066	1.055	1.063	1.081	1.050	1.049	1.070
	9	1.019	1.045	1.082	1.012	1.062	1.084	1.015	1.049	1.079	1.034	1.030	1.080
	12				0.866	0.932	0.968	1.068	0.915	0.945	0.868	0.931	0.949
	15	0.952	0.978	1.011	0.971	0.993	1.020	0.924	0.972	0.994	0.968	0.997	1.034
	18				1.001	1.001	1.020	1.001	0.998	1.022	0.989	0.992	1.016
	21	1.011	0.999	1.043	1.030	1.017	1.041	1.024	1.020	1.007	1.006	1.003	1.028
	24				1.030	1.015	1.036	1.005	0.998	1.028	0.997	0.994	1.017
	27	0.852	0.861	0.963	0.850	0.932	0.923	0.847	0.934	0.951	0.839	0.917	0.947
30					1.077	1.007	0.990	1.044	1.003	0.958	1.049	0.999	0.994
33		0.991	0.916	0.921	0.963	0.940	0.946	0.970	0.949	0.936	1.000	0.959	0.970
36					1.056	1.028	0.993	1.049	1.028	1.018	1.030	1.030	1.008
39		0.939	0.965	1.011	1.017	0.982	0.985	0.936	0.960	0.996	1.026	0.991	1.002
42					0.985	0.971	0.985	0.962	0.966	0.996	1.006	0.991	1.003
45		0.952	0.974	0.943	0.949	0.974	0.957	0.951	0.972	0.982	0.937	0.956	0.951
48					0.808	0.899	0.960	0.815	0.895	0.960	0.844	0.919	0.898
51		0.847	0.976	0.957	0.840	0.985	0.971	0.858	0.982	0.968	0.889	0.975	0.968
54		1.031	1.064	1.072	1.041	1.059	1.056	1.040	1.049	1.068	1.037	1.056	1.070
57		1.074	1.074	1.093	1.077	1.087	1.089	1.081	1.094	1.094	1.071	1.067	1.065

TABLE IX
RESULTS OF WATER TESTS WITH SCALE
MODEL NOZZLE TUBE

RUN	DATA POINT	\dot{W} lb/sec.	V in ³ /sec.	P_{in} lb/in ² gage	$\Delta P_{in-dis.}$ lb/in ²	$Re(10^{-4})$ $d=.316$	$\xi_{in-dis.}$
WT1	1	0.384	10.639	9.175	9.624	2.67	11.187
\uparrow $P_{atm} = 14.785 \text{ psi}$ \downarrow	2	0.495	13.714	14.875	15.621	3.44	10.928
	3	0.578	16.014	20.625	21.642	4.03	11.104
	4	0.626	17.344	24.200	25.388	4.36	11.105
	5	0.656	18.169	26.000	27.304	4.56	10.883
	6	0.693	19.194	27.950	29.411	4.82	10.504
	7	0.782	21.681	34.150	36.014	5.45	10.081
WT2	1	0.254	7.037	3.500	3.696	1.77	9.822
\uparrow $P_{atm} = 14.780 \text{ psi}$ \downarrow	2	0.238	6.594	3.000	3.172	1.65	9.600
	3	0.382	10.584	8.675	9.119	2.66	10.711
	4	0.448	12.412	11.950	12.560	3.12	10.728
	5	0.521	14.435	16.300	17.126	3.63	10.815
	6	0.560	15.515	18.475	19.430	3.90	10.620
	7	0.612	16.956	22.000	23.340	4.26	10.682
	8	0.649	17.981	24.550	25.832	4.51	10.513
	9	0.690	19.117	27.375	28.824	4.80	10.378
	10	0.732	20.281	30.225	31.856	5.10	10.191
	11	0.770	21.334	32.950	34.755	5.35	10.047
	12	0.809	22.414	35.150	37.142	5.64	9.728
	13	0.823	22.802	37.350	39.412	5.74	9.974
	14	0.870	24.104	39.600	41.903	6.06	9.490
	15	0.887	24.575	41.150	45.545	6.17	9.487

TABLE X
RESULTS OF WATER TESTS WITH GEOMETRICALLY SIMILAR
MODEL OF SECTION BETWEEN PLANES W AND X

RUN	\dot{W} lb/sec	V in ³ /sec	$Re(10^{-4})$ $d = 1.05$	f_{1-6}	ξ_{1-6}	K(.757) pos. B	K(.761) pos. A	K(.714) pos. A	K(.714) pos. B
W1	0.198	5.488	0.415	1.082	5.824	.720	.697		
	0.313	8.674	0.656	1.388	6.886	.768	.727		
	0.509	14.112	1.068	1.167	5.600	.775	.739		
	0.739	20.474	1.549	1.253	5.304	.787	.787		
	0.910	25.203	1.907	1.232	5.333	.780	.778		
	1.007	27.912	2.112	1.219	5.375	.774	.771		
	1.124	31.149	2.357	1.219	5.419	.780	.768		
	1.191	32.994	2.496	1.204	5.402	.766	.764		
	1.270	35.203	2.663	1.203	5.367	.767	.767		
	1.372	38.023	2.877	1.204	5.576	.755	.753		
	1.515	41.969	3.175	1.208	5.673	.743	.748		
	1.759	48.715	3.686	1.216	5.689	.745	.749		
	1.829	50.682	3.834	1.222	5.680	.746	.751		
W2	0.878	24.340	1.841	1.224	5.664	.762	.753		
	1.183	32.769	2.479	1.208	5.617	.760	.751		
	1.344	37.246	2.818	1.181	5.718	.752	.736		
	1.437	39.814	3.012	1.178	5.730	.745	.740		
	1.812	50.213	3.799	1.174	5.619	.754	.740		
	1.929	53.435	4.044	1.207	5.686	.747	.746		
	1.946	53.913	4.078	1.193	5.768	.742	.737		
W3	0.559	15.485	1.221	1.487	8.669			.794	.748
	0.809	22.406	1.767	1.481	8.456			.802	.748
	0.876	24.285	1.915	1.481	8.688			.792	.734
	0.988	27.384	2.160	1.440	8.418			.793	.746
	1.078	29.881	2.357	1.462	8.693			.786	.730
	1.262	34.958	2.757	1.457	8.971			.773	.724
	1.343	37.222	2.936	1.454	9.112			.766	.715
	1.440	39.903	3.147	1.449	9.035			.768	.718
	1.494	41.407	3.266	1.452	9.230			.760	.714
	1.589	44.029	3.473	1.447	9.034			.767	.724
	1.690	46.828	3.693	1.434	9.216			.756	.713
	1.754	48.587	3.832	1.430	8.698			.778	.733

TABLE XI
OXIDIZER DISCHARGE & RETURN ASSEMBLY, INLET
ORIFICE DATA AND EQUIVALENT FLOW RATES

$$P_{\text{atm}} = 14.743 \text{ lb/in}^2$$

RUN AVERAGE OF DATA POINTS	R7	R8	R9	R10	R11
P_u (lb/in ²)	18.055	18.943	19.986	21.179	22.220
Δh_o (in H ₂ O)	0.991	1.198	1.448	1.736	1.951
T_u (°R)	541.0	564.5	561.0	554.0	580.5
T_{plen} (°R)	539.5	559.5	559.0	553.5	576.0
$Re(10^{-5})$ $d = 4.07''$	0.917	0.985	1.117	1.276	1.320
w_u^* (in ²)	.50180	.53848	.57723	.61355	.63494
\bar{P}_{tZ} (lb/in ²)	17.769	18.651	19.602	20.750	21.721
\bar{P}_{tA} (lb/in ²)	17.597	18.388	19.296	20.393	21.330
\bar{P}_{tF} (lb/in ²)	15.589	15.827	16.114	16.462	16.752
\bar{P}_{tG} (lb/in ²)	15.464	15.668	15.913	16.216	16.463
\bar{w}_Z^* (in ²)	.50916	.54449	.58750	.62596	.64702
\bar{w}_A^* (in ²)	.51414	.55228	.59679	.63690	.65888
\bar{w}_F^* (in ²)	.58037	.64164	.71467	.78901	.83895
\bar{w}_G^* (in ²)	.58505	.64817	.72367	.80098	.85364
\bar{P}_{tO} (lb/in ²)	18.005	18.890	19.894	21.093	22.132

TABLE XII
LOSS COEFFICIENTS PLANES Z TO A, A TO F,
F TO G, G TO H, H TO I, W TO X
DISCHARGE MACH NUMBER

RUN	R7	R8	R9	R10	R11
\bar{k}_{Z-A} (in ⁻⁴)	.0374	.0473	.0451	.0438	.0430
\bar{k}_{A-F} (in ⁻⁴)	.4316	.4564	.4630	.4752	.4944
\bar{k}_{F-G} (in ⁻⁴)	.0237	.0245	.0243	.0240	.0244
\bar{k}_{G-H} (in ⁻⁴)	.0414	.0415	.0410	.0407	.0409
\bar{P}_{t_I} (in H ₂ O)	420.98	425.07	429.52	434.54	439.60
\bar{P}_I (in H ₂ O)	407.00	407.03	406.71	406.23	405.83
\bar{M}_I	.22	.25	.28	.31	.34
\bar{k}_{G-I} (in ⁻⁴)	.0500	.0486	.0486	.0506	.0493
\bar{k}_{H-I} (in ⁻⁴)	.0086	.0071	.0076	.0099	.0084
\bar{k}_{A-X} (in ⁻⁴)	.4296	.4539	.4600	.4702	.4894
\bar{P}_{t_X} (lb/in ²)	15.601	15.845	16.138	16.492	16.801
Re (10 ⁻⁴) d = 0.3	2.392	2.567	2.913	3.329	3.442
\bar{P}_{t_W} (lb/in ²)	17.338	18.024	18.914	19.935	20.752
\bar{w}_W^* (in ²)	.52182	.56342	.60886	.65180	.67614
$f = \Delta \bar{P}_{t_{W-X}} / \Delta \bar{P}_{B-C}$	1.46	1.458	1.453	1.447	1.445
\bar{k}_{W-X} (in ⁻⁴)	.3678	.3908	.3959	.4061	.4193
ξ_{W-X}	9.938	10.560	10.698	10.973	11.329

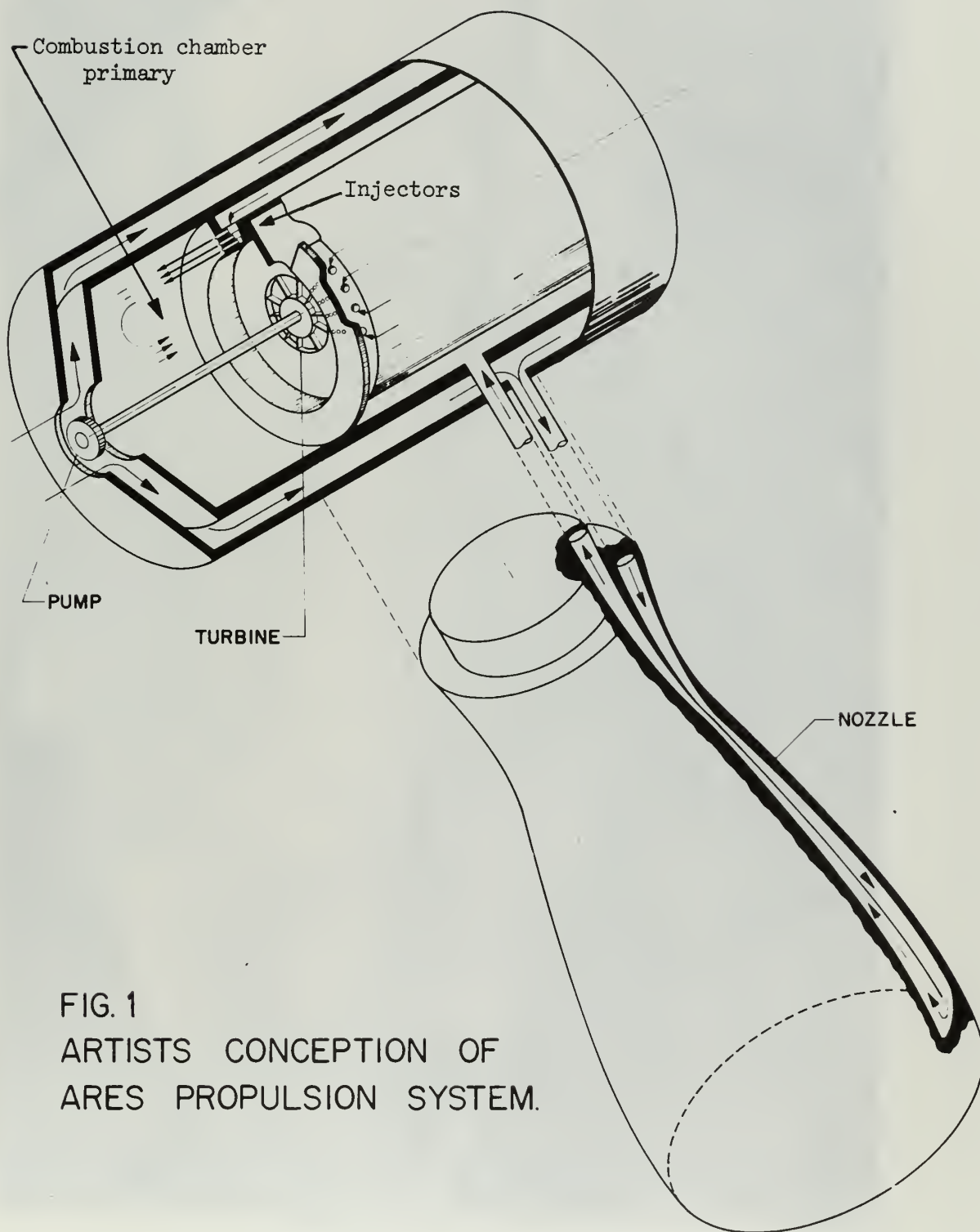
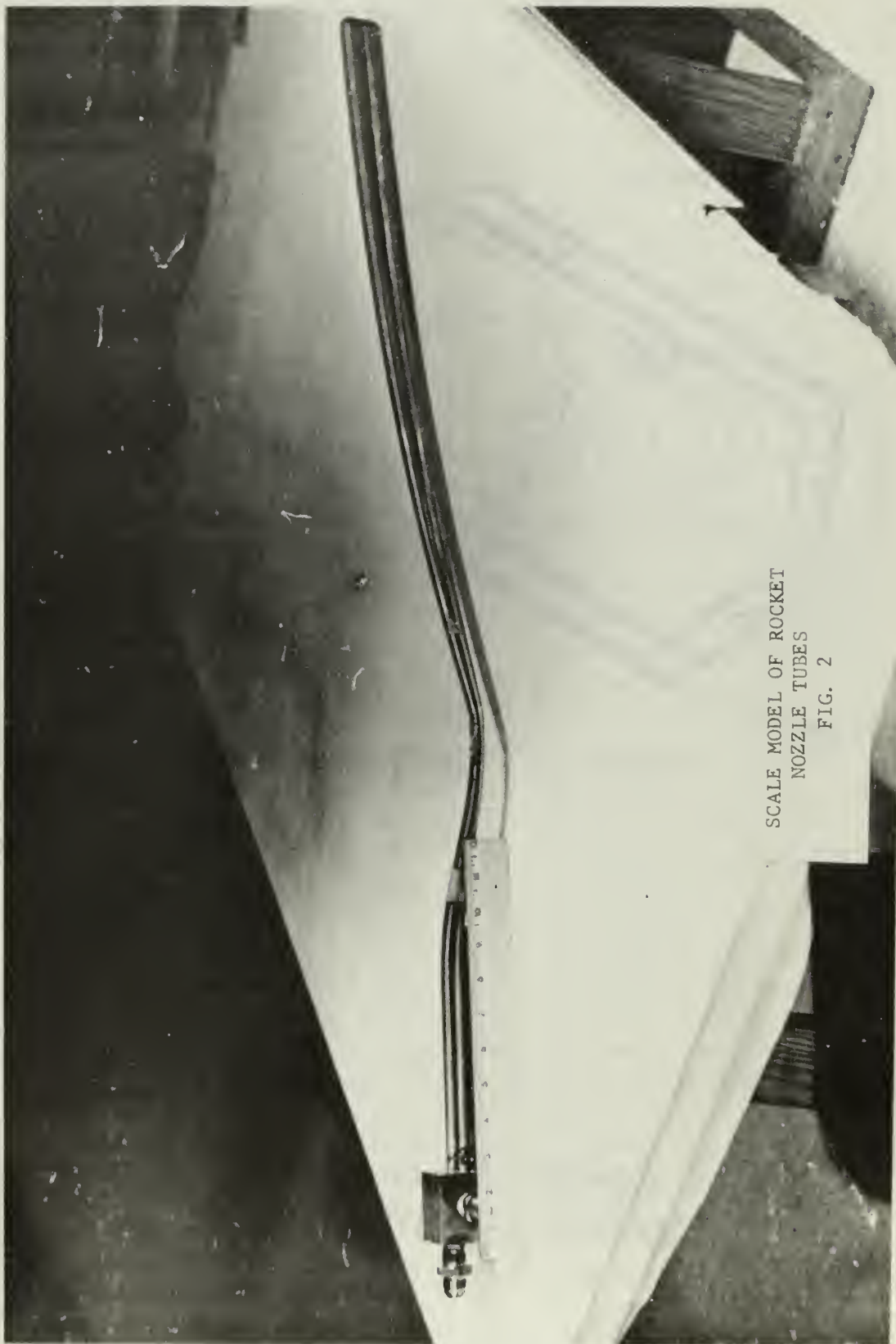


FIG. 1
ARTIST'S CONCEPTION OF
ARES PROPULSION SYSTEM.

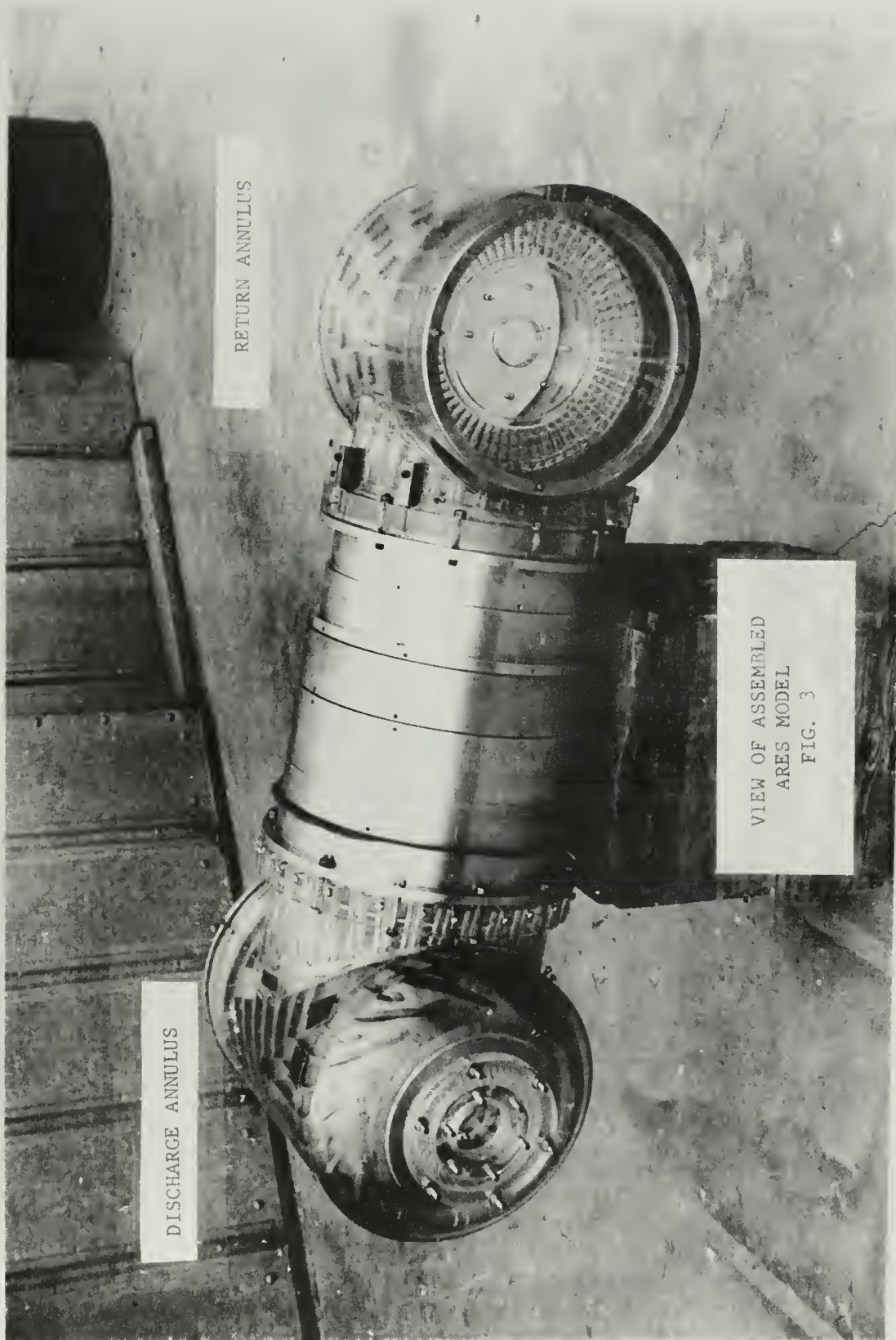


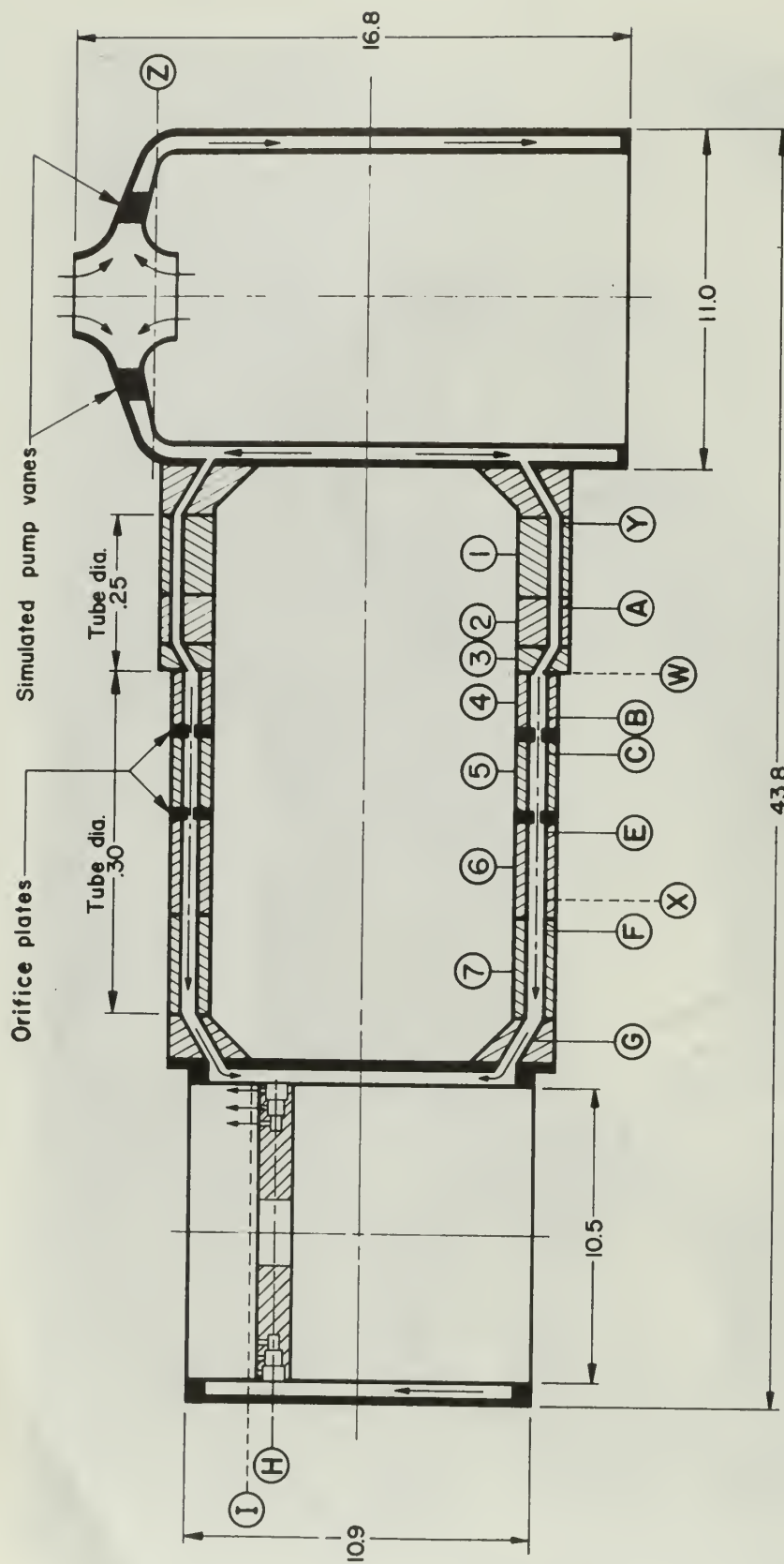
SCALE MODEL OF ROCKET
NOZZLE TUBES
FIG. 2

DISCHARGE ANNULUS

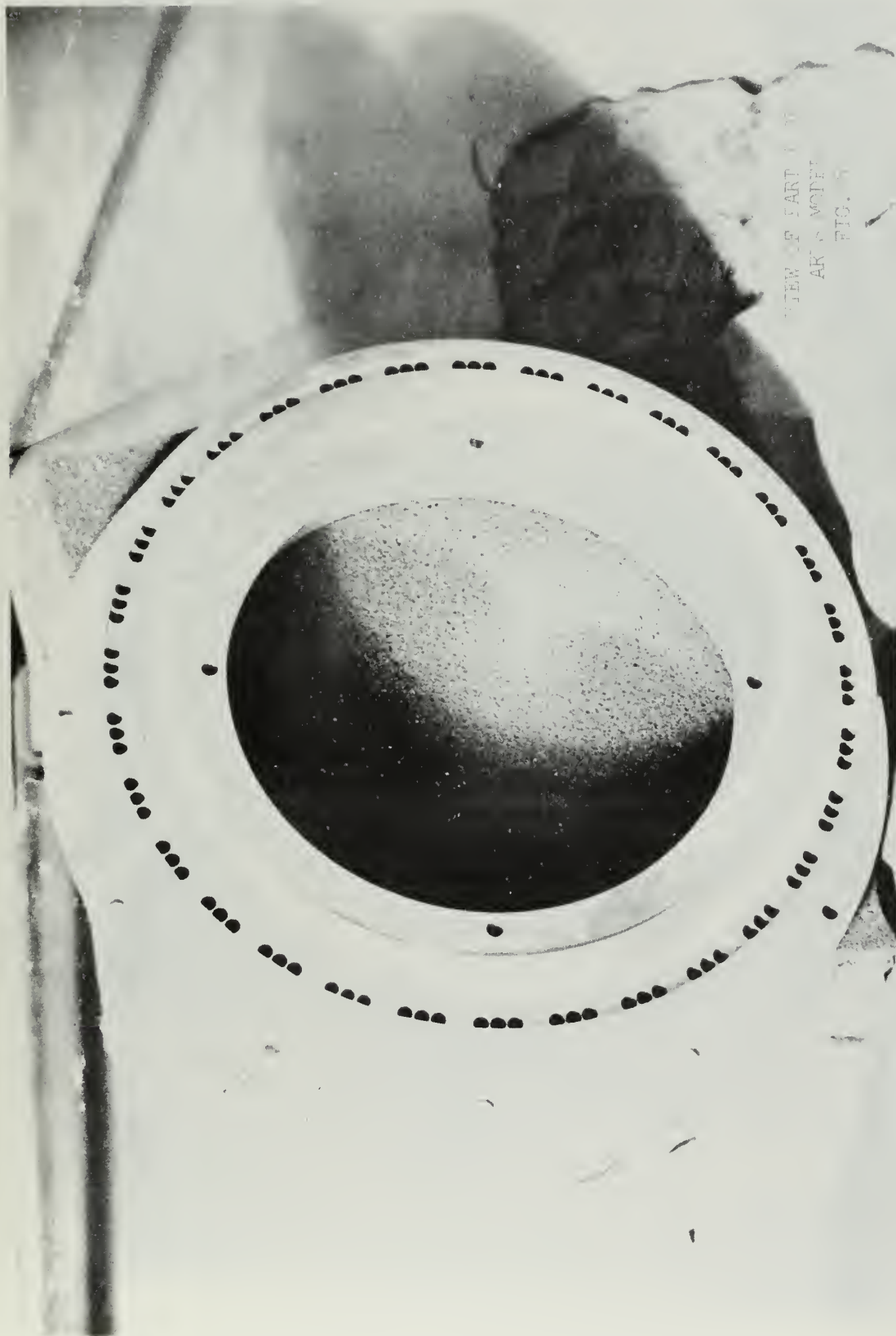
RETURN ANNULUS

VIEW OF ASSEMBLED
ARES MODEL
FIG. 3

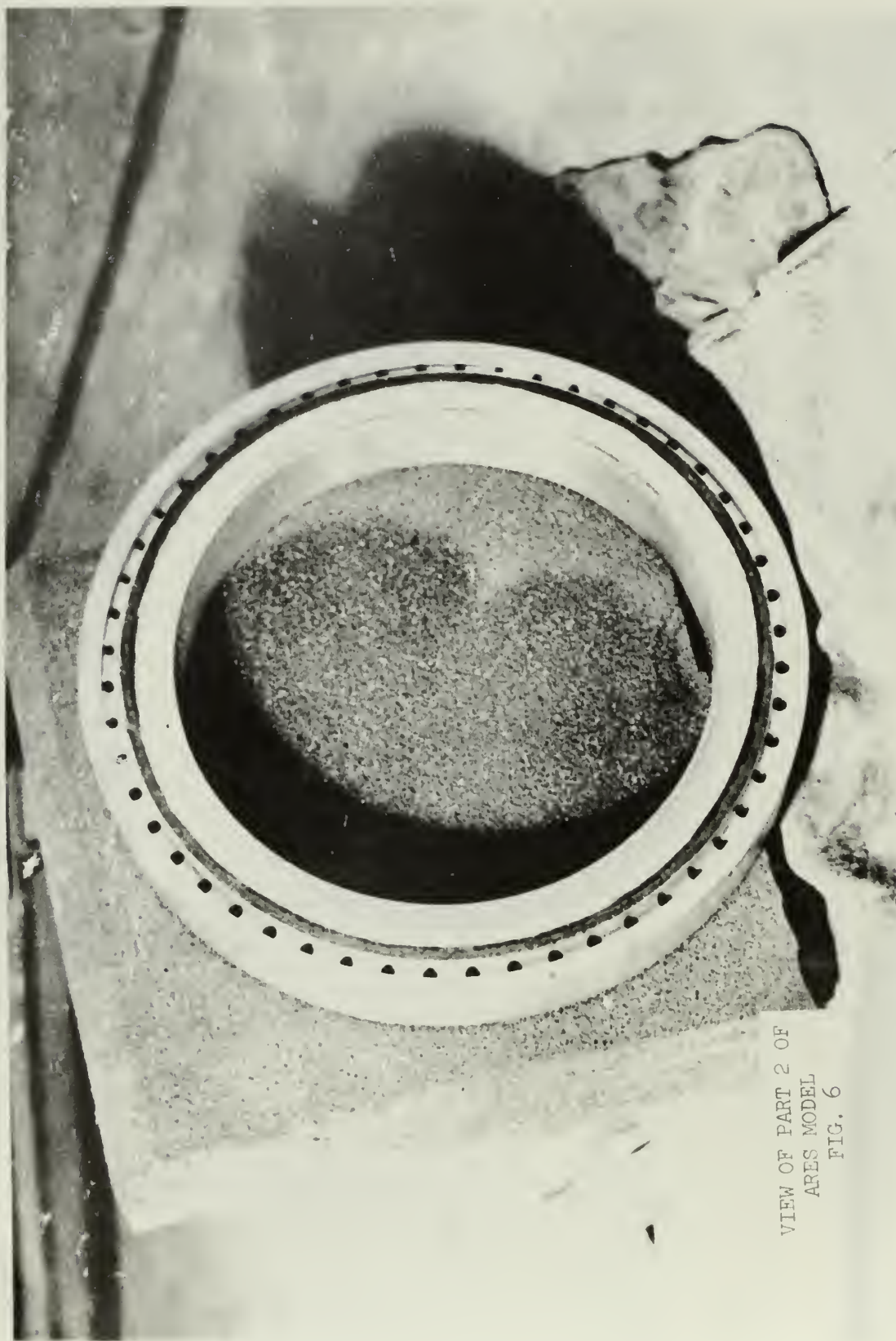




SCHEMATIC OF FLOW PASSAGES
IN ARES MODEL
FIG. 4



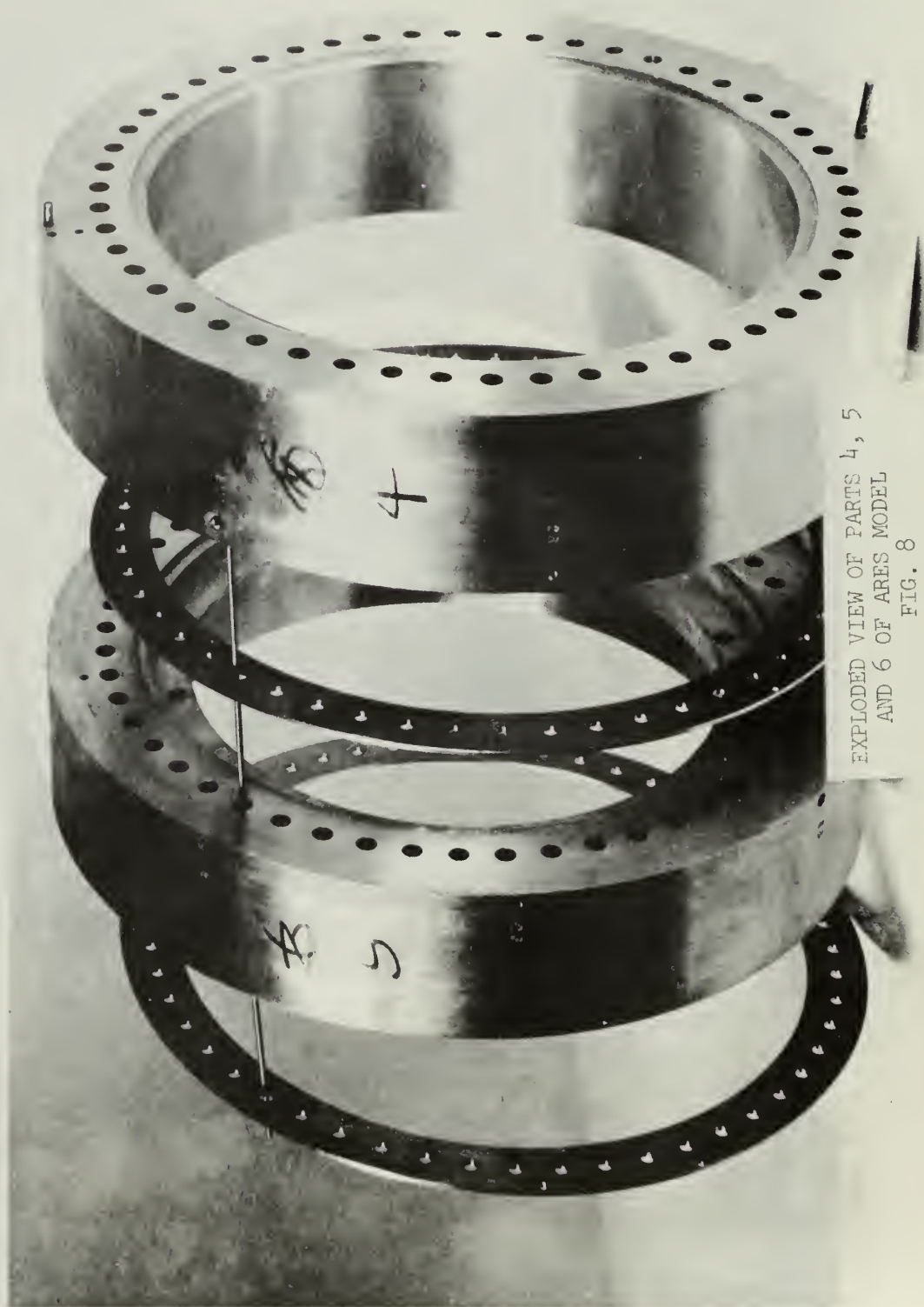
VIEW OF PART OF
ART. 5. MODEL
FIG. 5



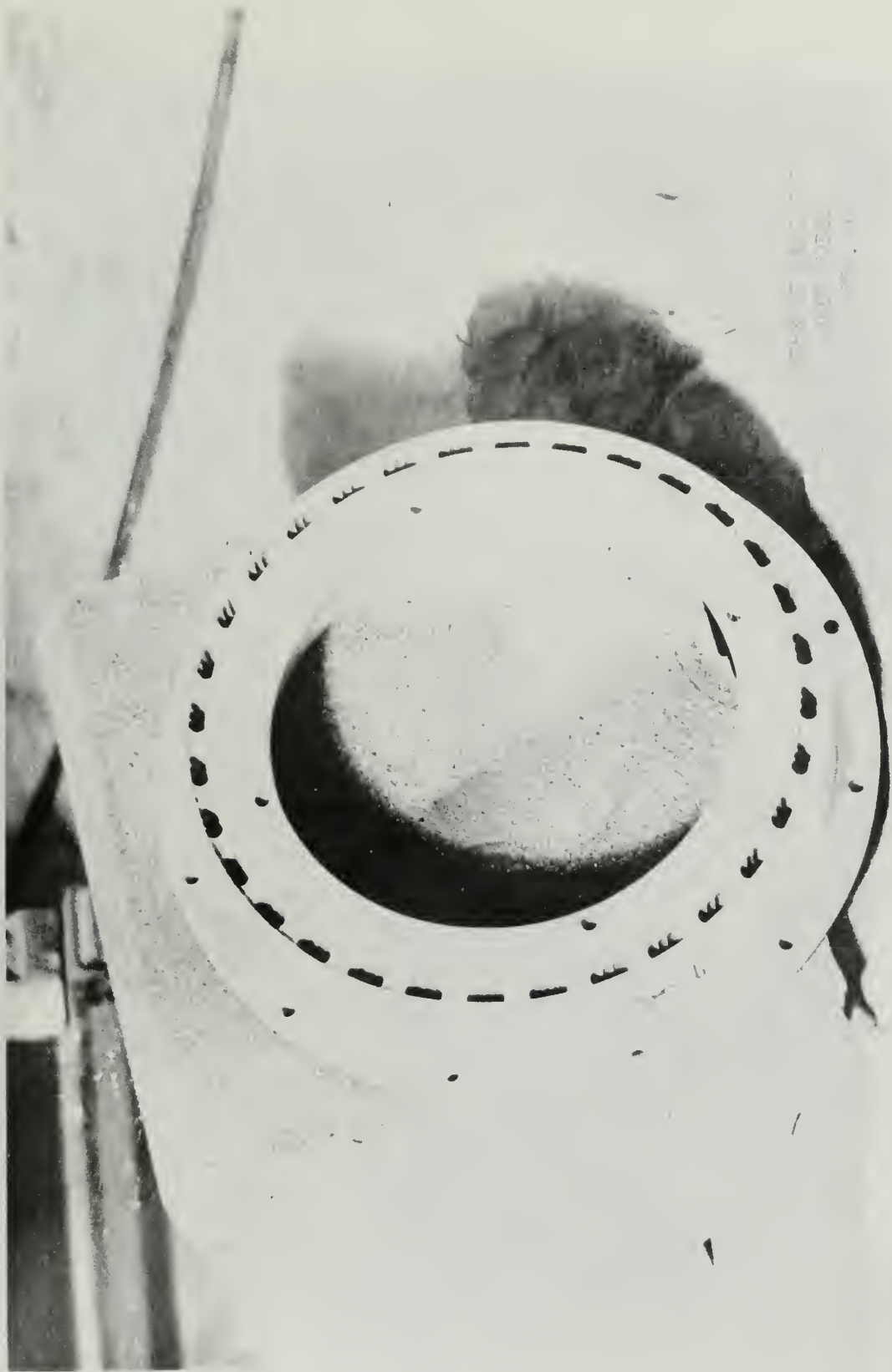
VIEW OF PART 2 OF
ARES MODEL
FIG. 6



VIEW OF PART 3 OF
ARES MODEL
FIG. 7

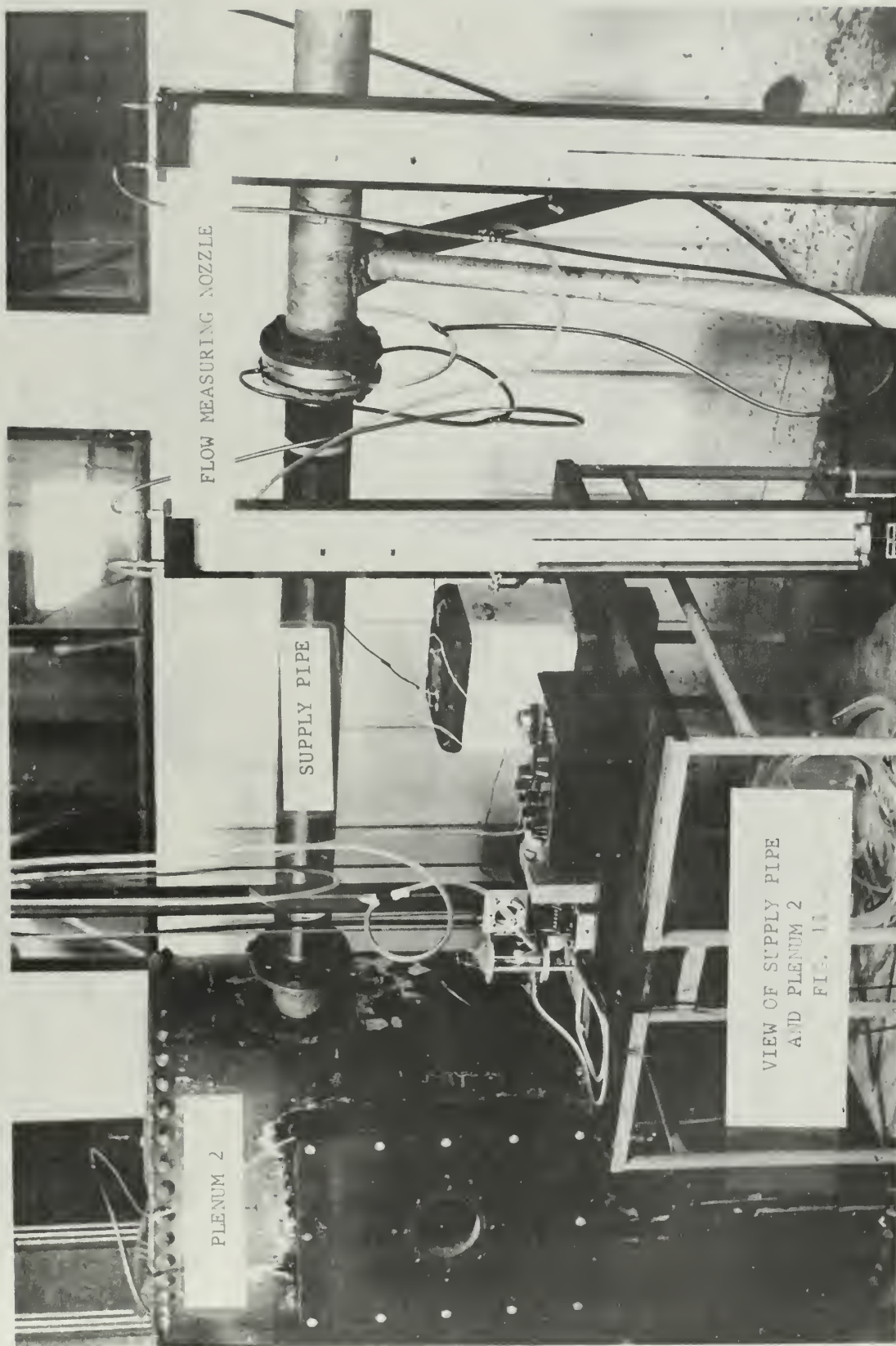


EXPLODED VIEW OF PARTS 4, 5
AND 6 OF APRES MODEL
FIG. 8



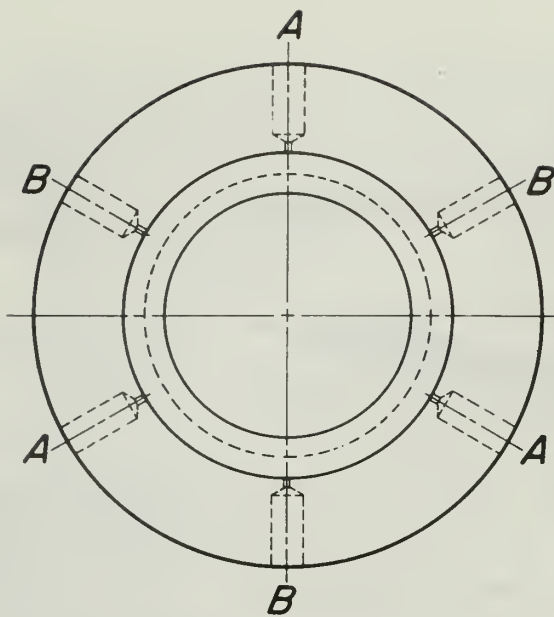


VIEW OF RETURN ANNULUS
FIG. 10



VIEW OF SUPPLY PIPE
AND PLENUM 2

FIG. 1



A - Pressure upstream
B - Pressure downstream

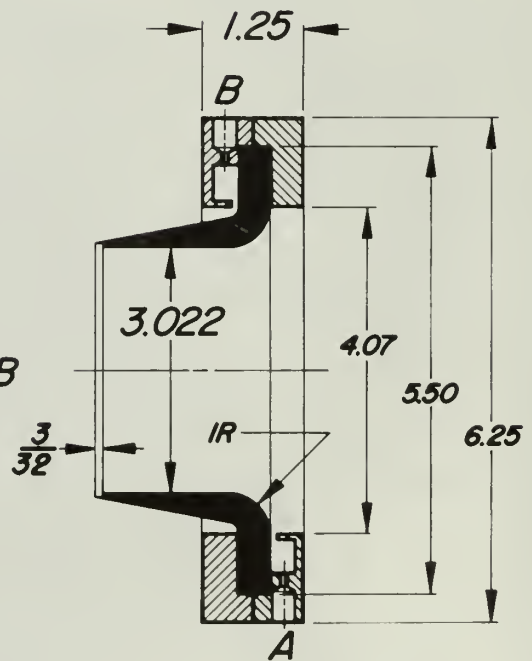
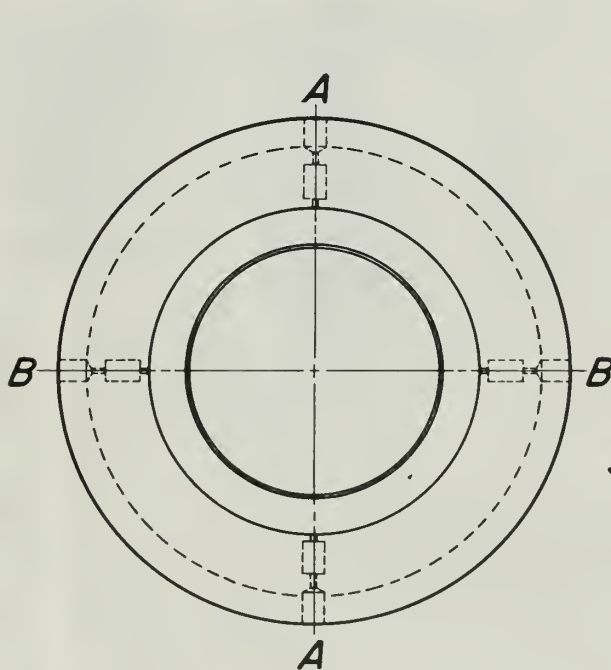
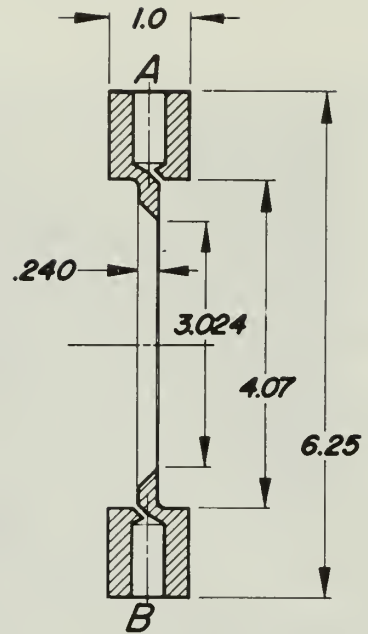
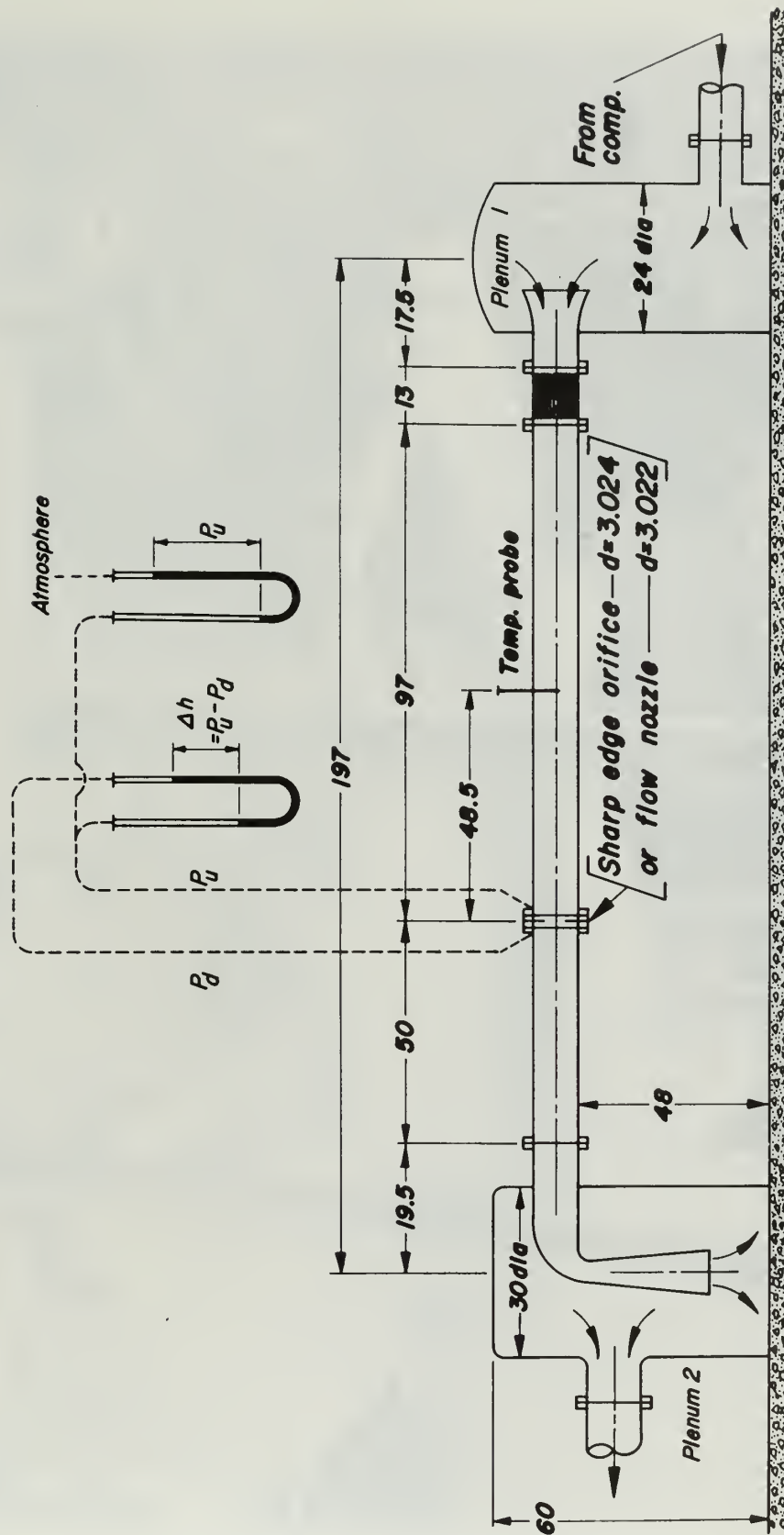
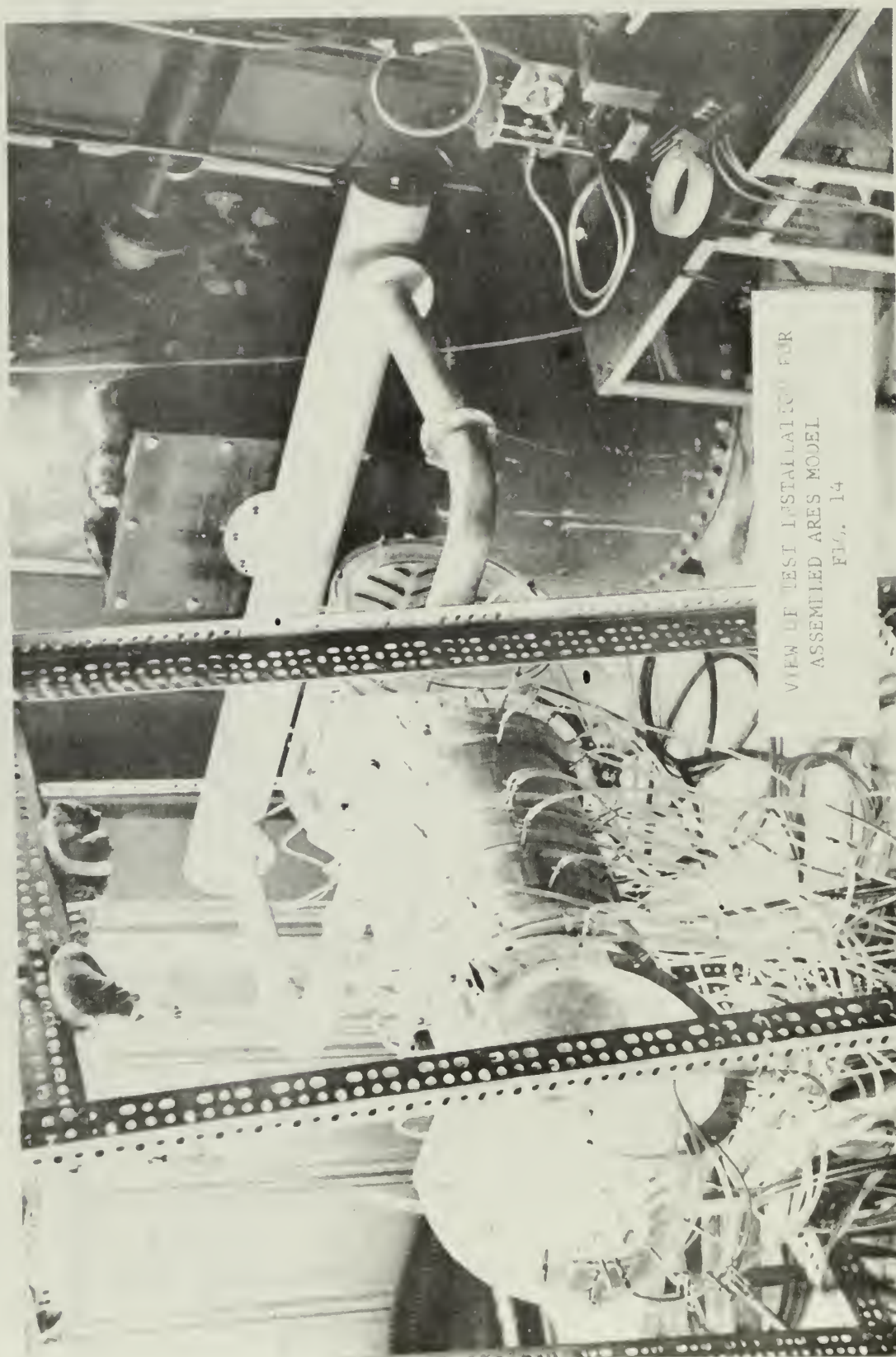


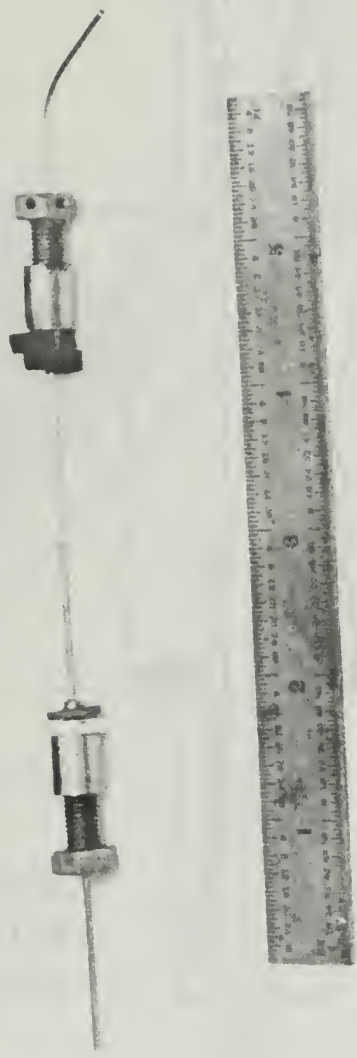
Fig 12 Schematic of sharp edge Orifice and flow nozzle.



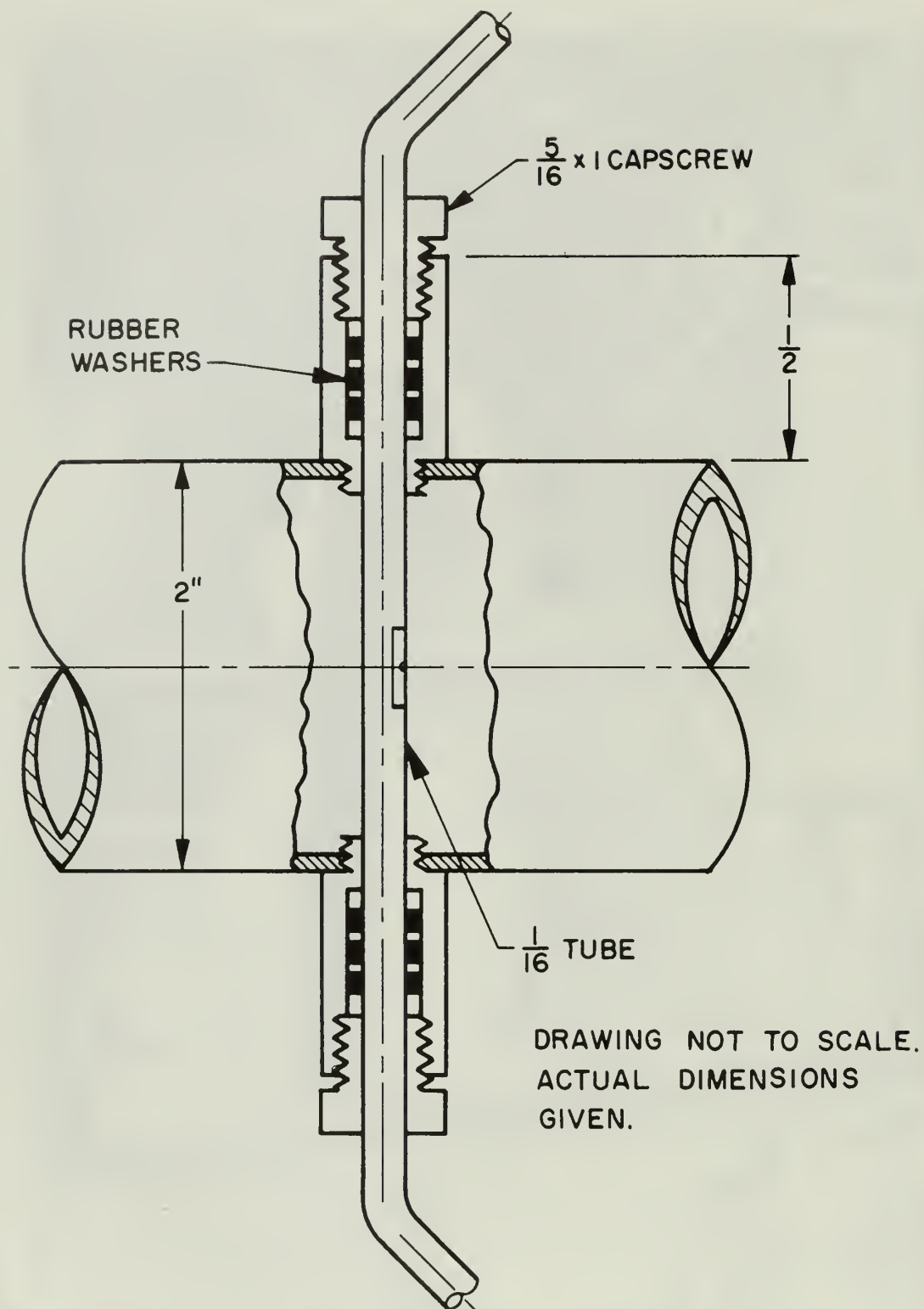
SCHEMATIC OF FLOW MEASURING
INSTALLATION
FIG. 13



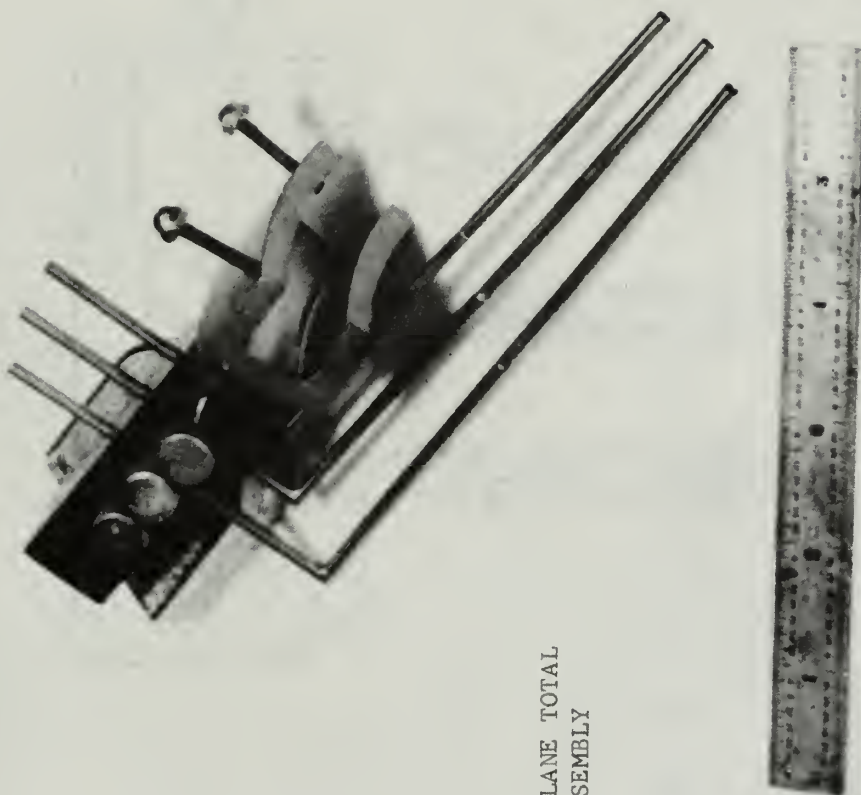
VIEW OF TEST INSTALLATION FOR
ASSEMBLED ARES MODEL
FIG. 14



TOTAL PRESSURE PROBE
USED AT MODEL INLET
FIG. 15

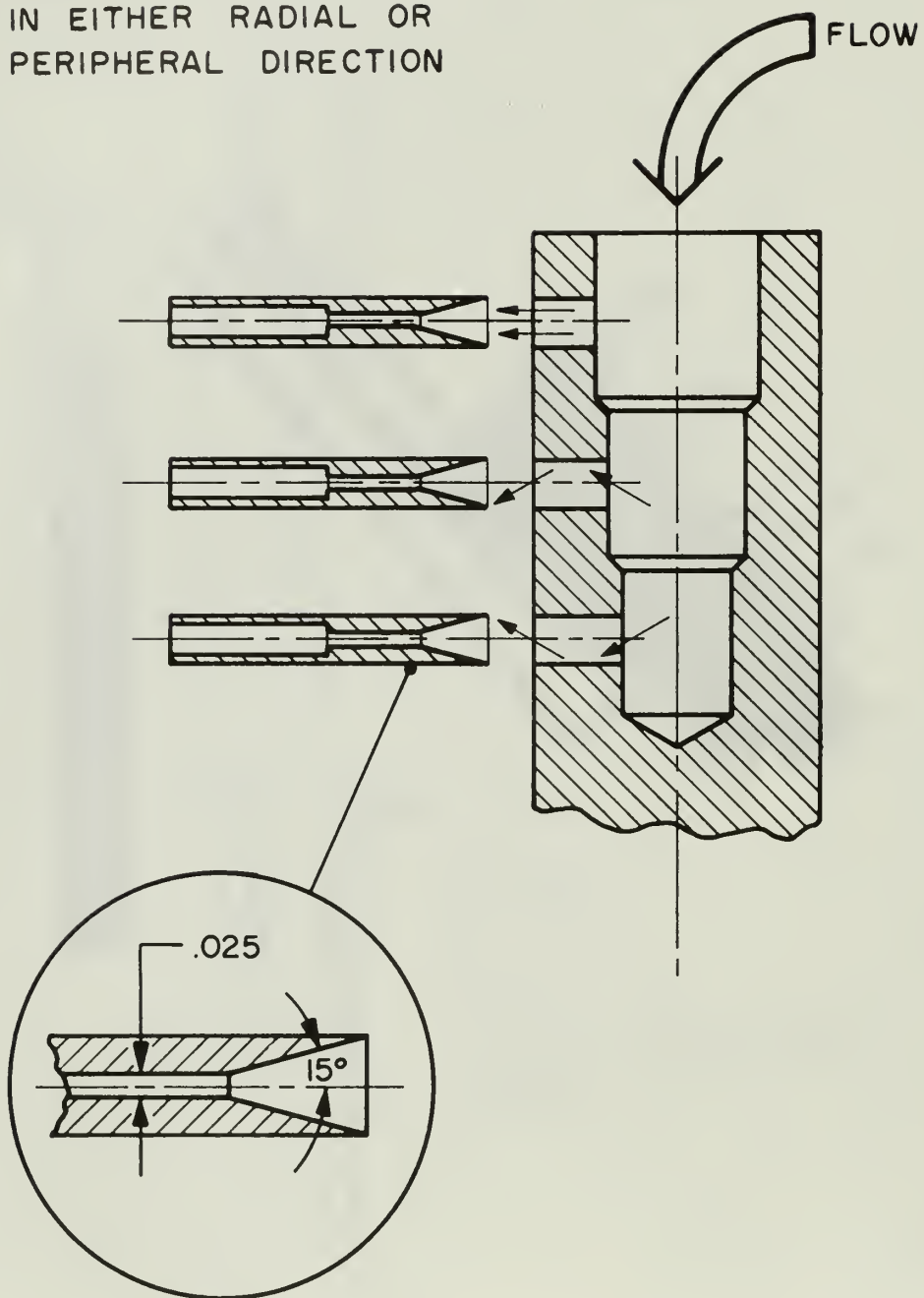


SCHEMATIC OF INLET TOTAL PRESSURE
PROBE INSTALLATION
FIG. 16



VIEW OF DISCHARGE PLANE TOTAL
PRESSURE PROBE ASSEMBLY
FIG. 17

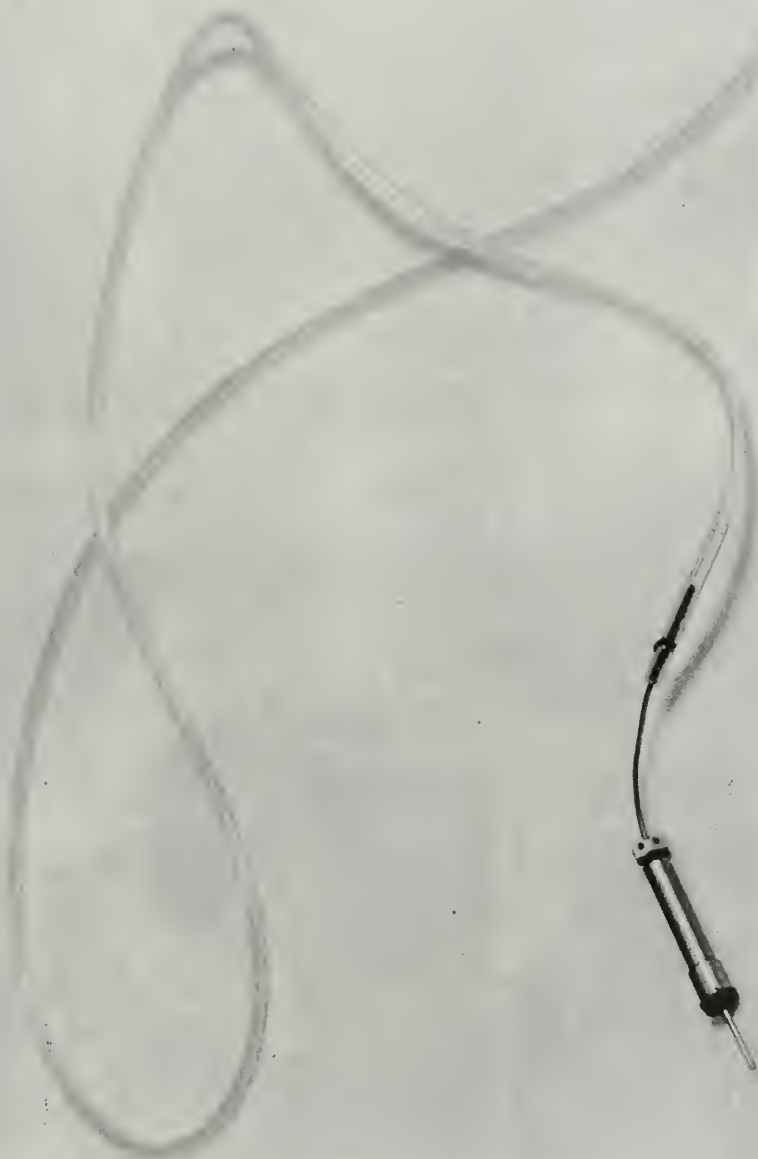
PROBES ADJUSTABLE
IN EITHER RADIAL OR
PERIPHERAL DIRECTION

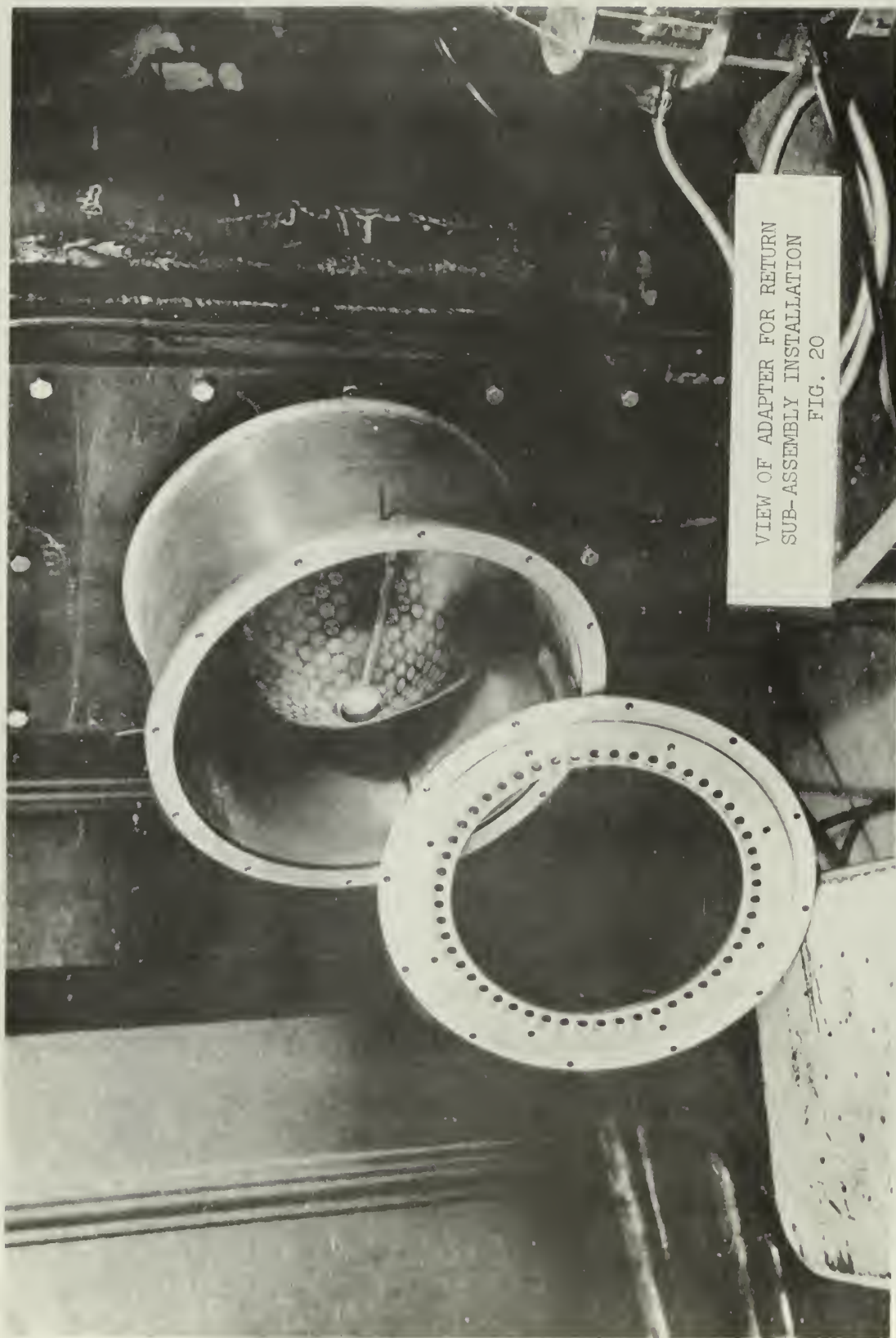


SCHEMATIC OF INJECTOR TUBE AND TOTAL
PRESSURE PROBE ALIGNMENT

FIG. 18

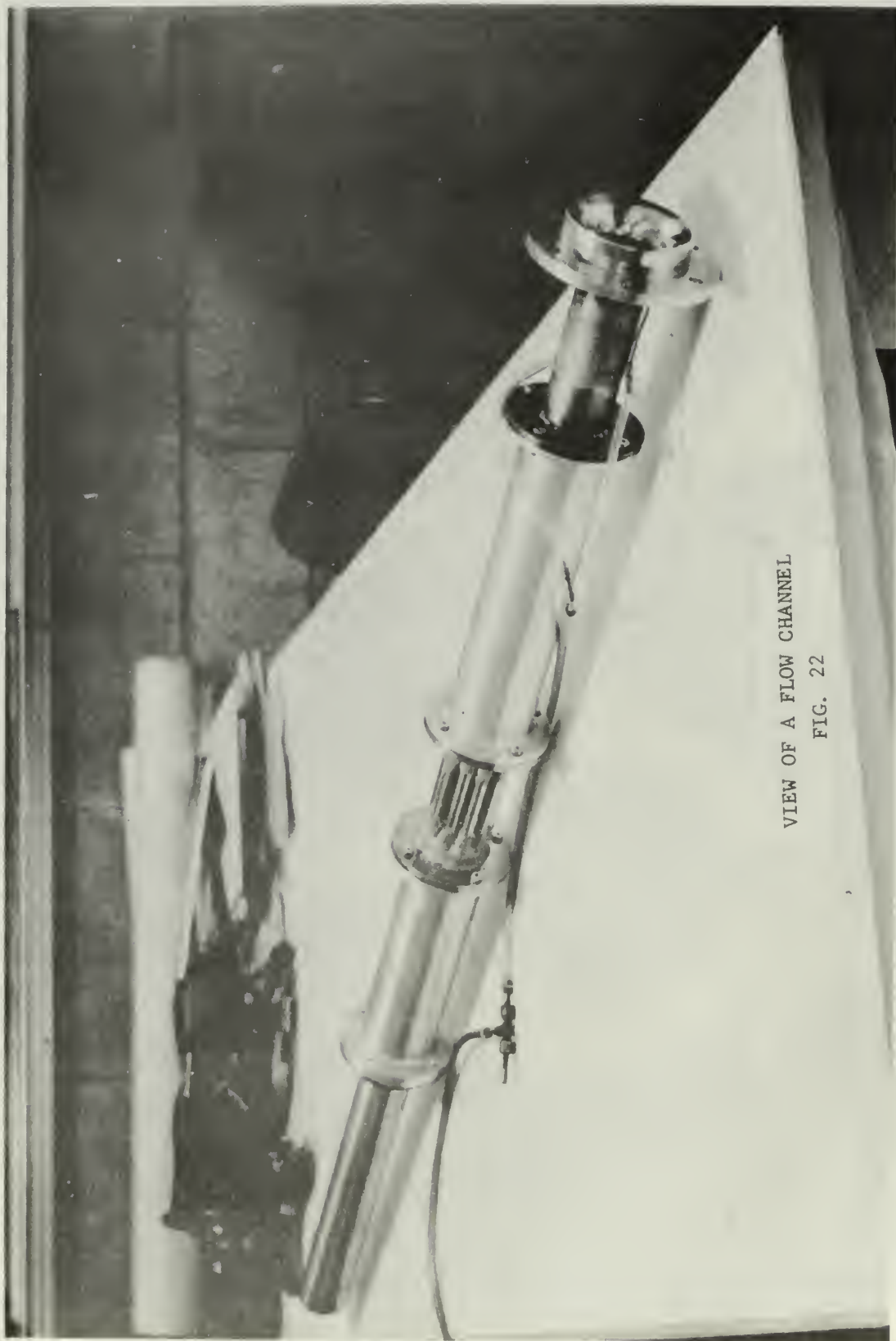
VIEW OF PORTABLE TOTAL
PRESSURE PROBE
FIG. 19







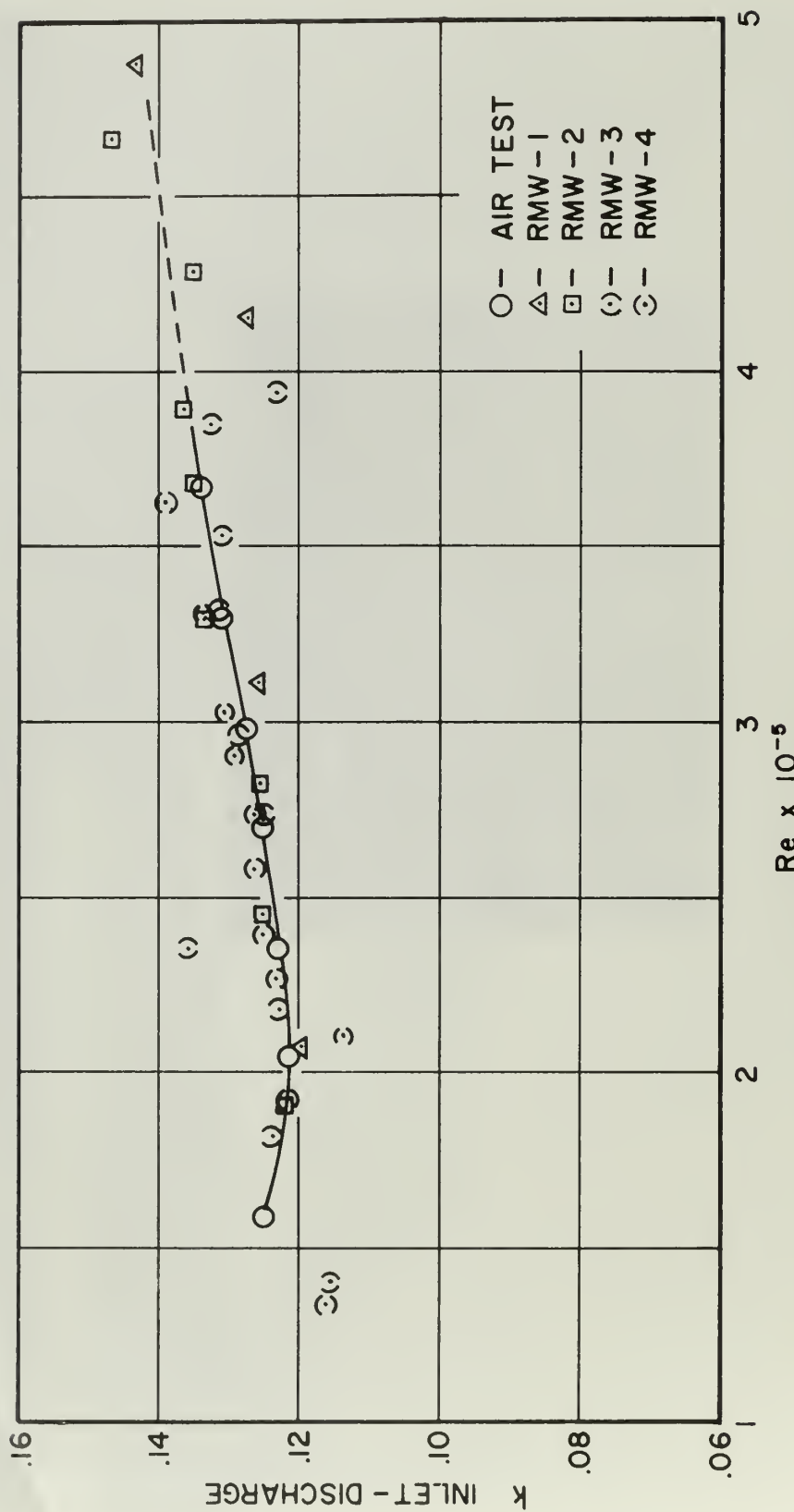
OXYLIZER RETURN SUB-ASSEMBLY TEST INSTALLATION
WITH PROVISIONS FOR WATER FLOW VISUALIZATION
FIG. 21



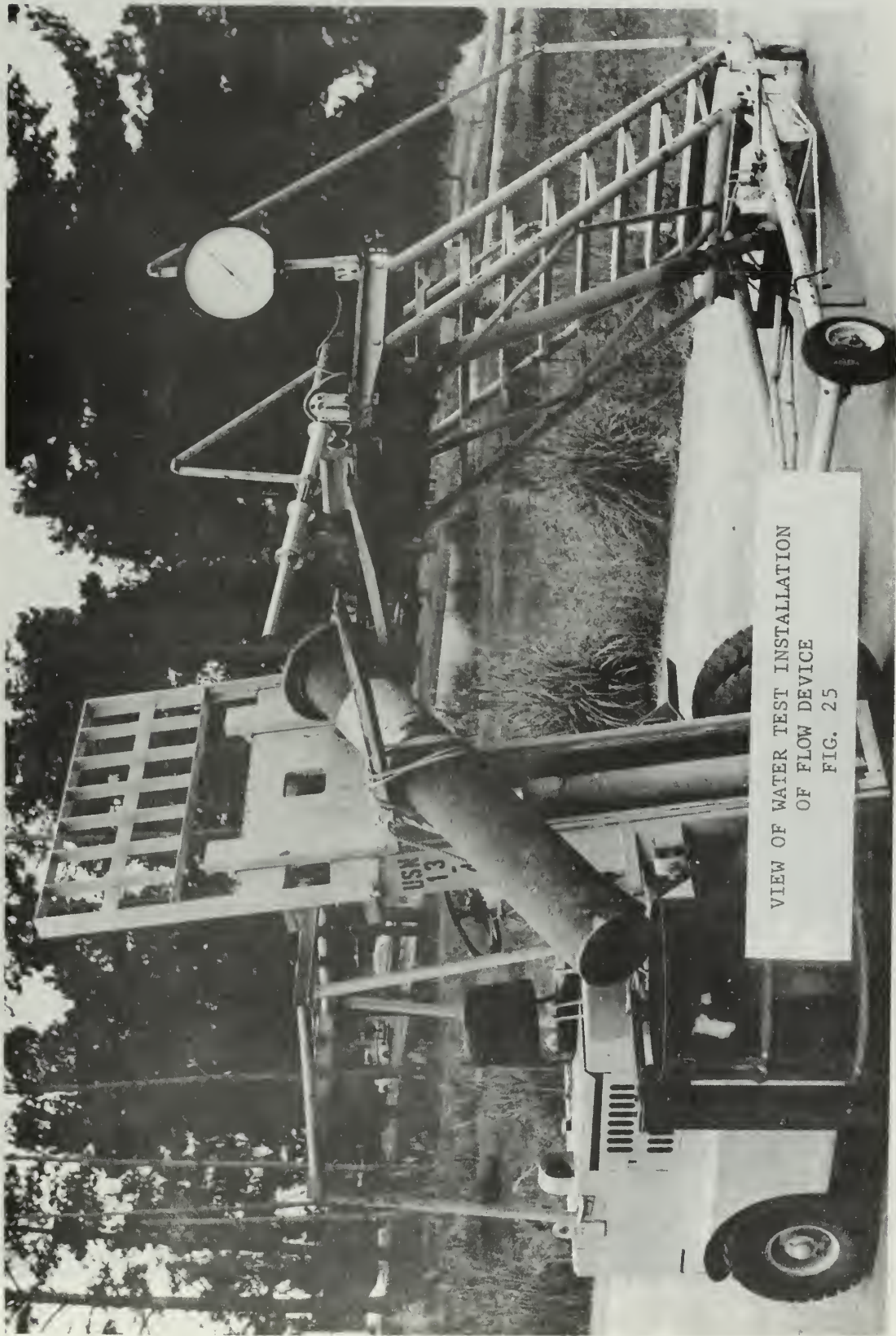
VIEW OF A FLOW CHANNEL
FIG. 22

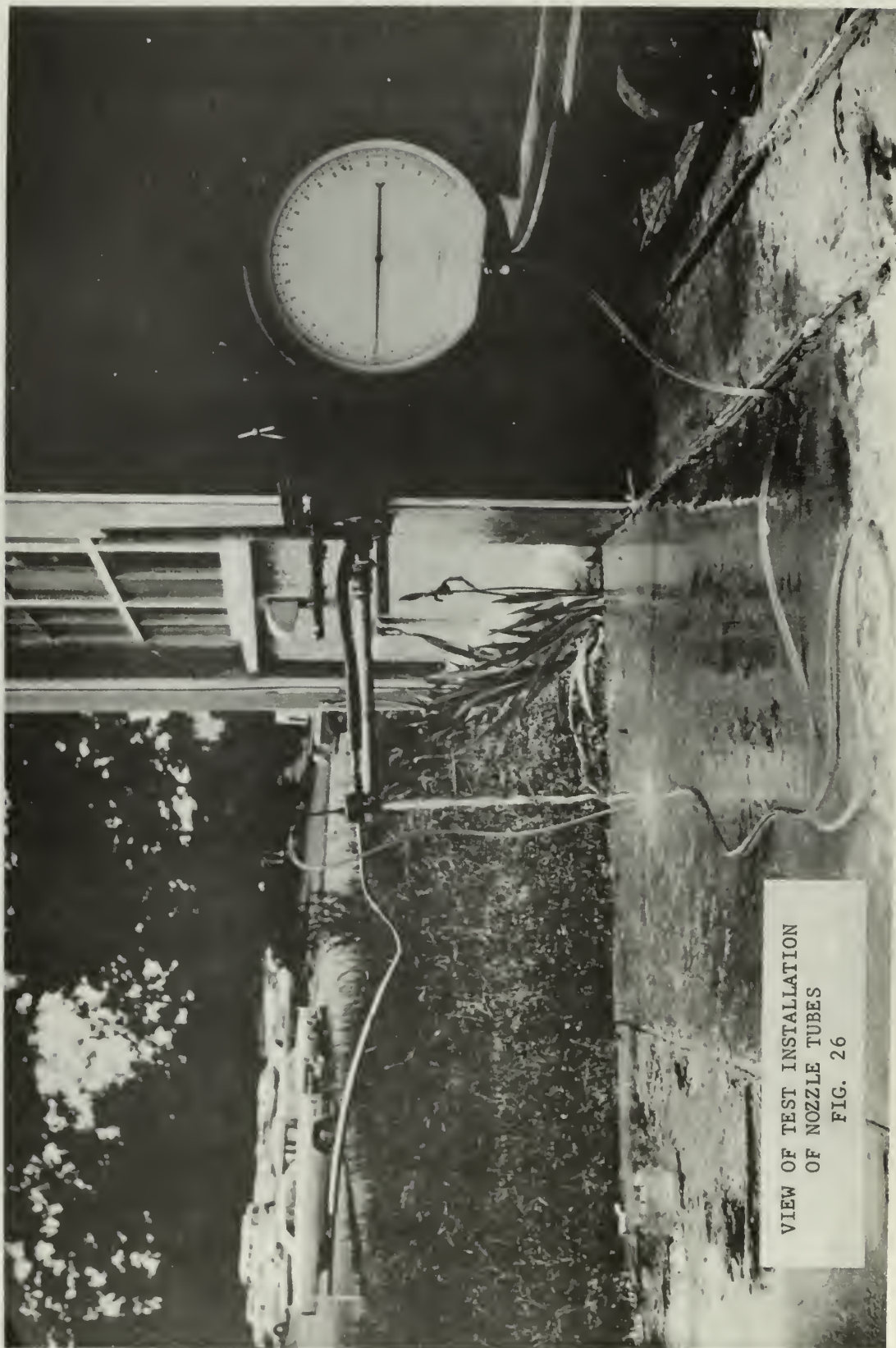


VIEW OF AIR TEST INSTALLATION
OF FLOW CHANNEL
FIG. 23



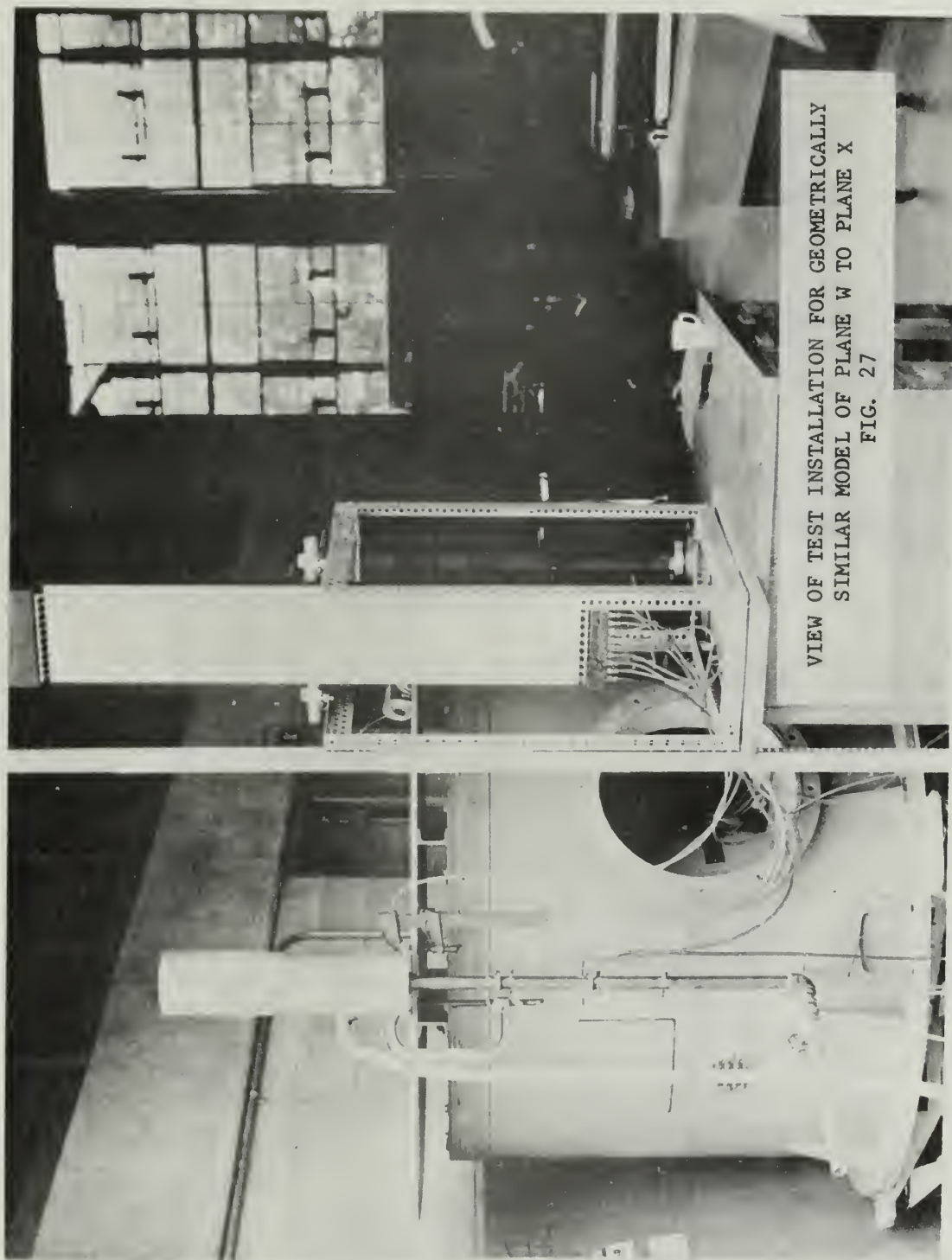
INLET TO DISCHARGE LOSS COEFFICIENT OF FLOW DEVICE
VS REYNOLDS NO.
FIG. 24





VIEW OF TEST INSTALLATION
OF NOZZLE TUBES
FIG. 26

VIEW OF TEST INSTALLATION FOR GEOMETRICALLY
SIMILAR MODEL OF PLANE W TO PLANE X
FIG. 27



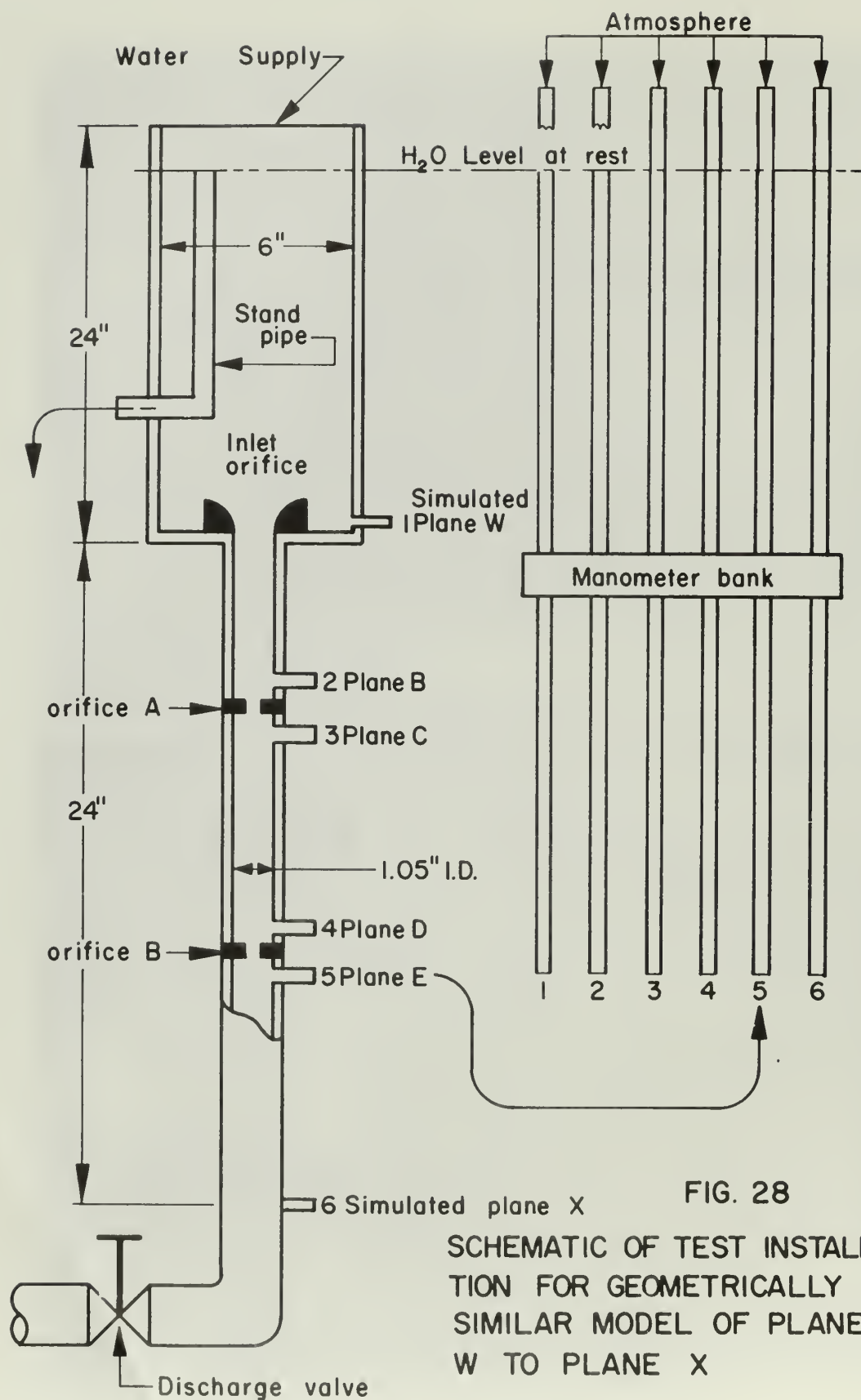
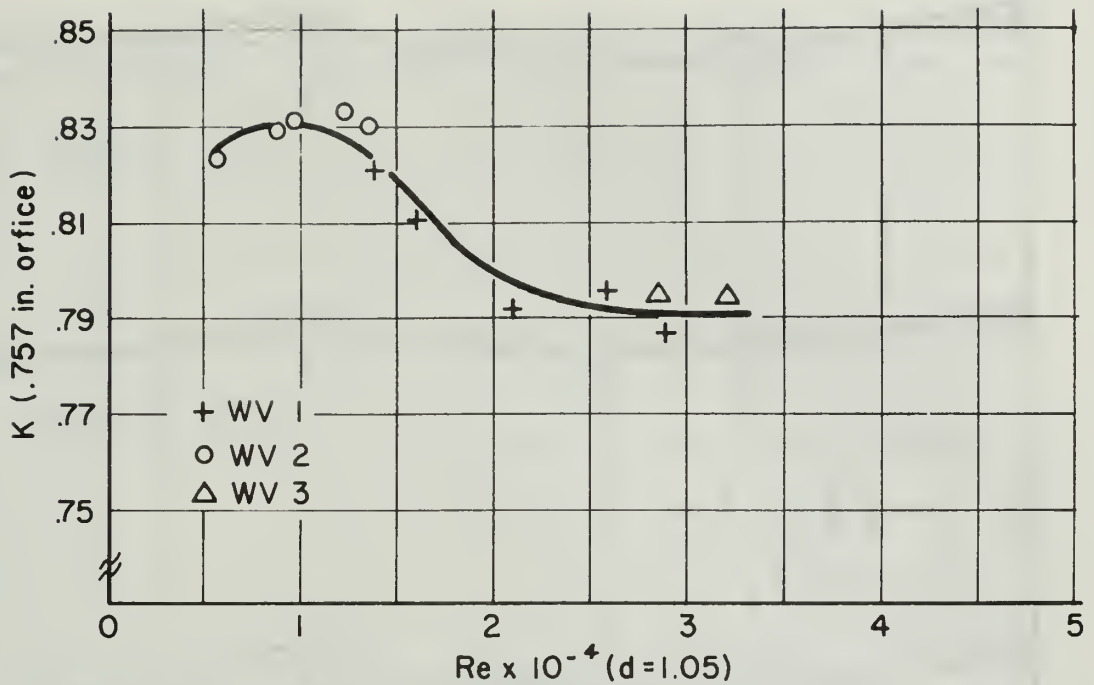
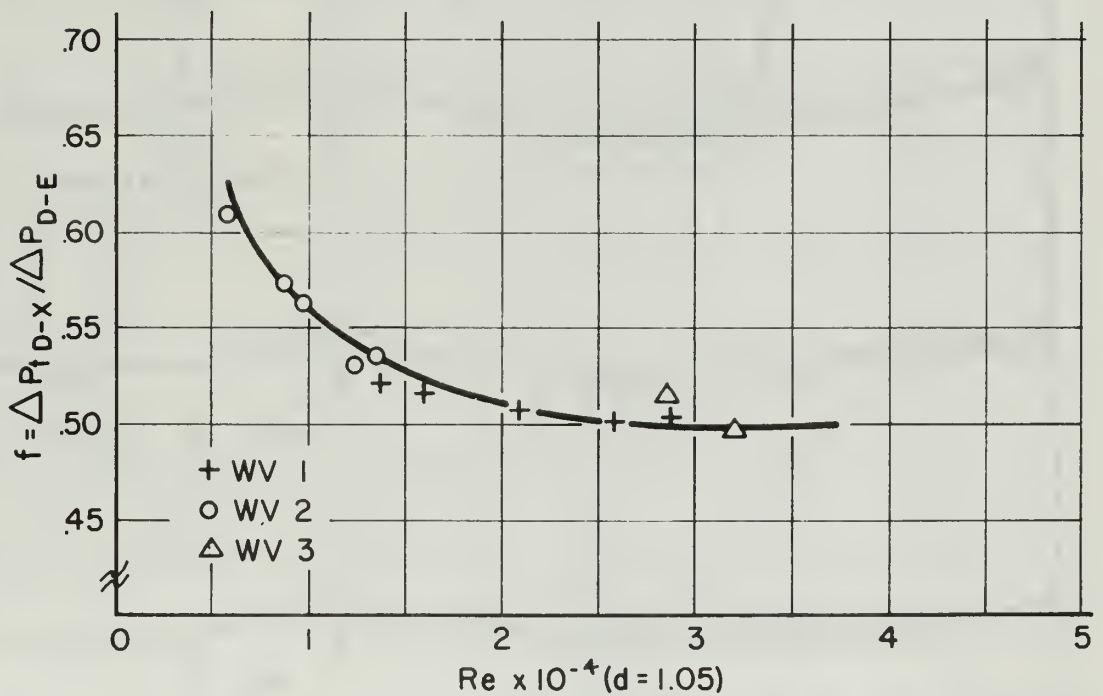


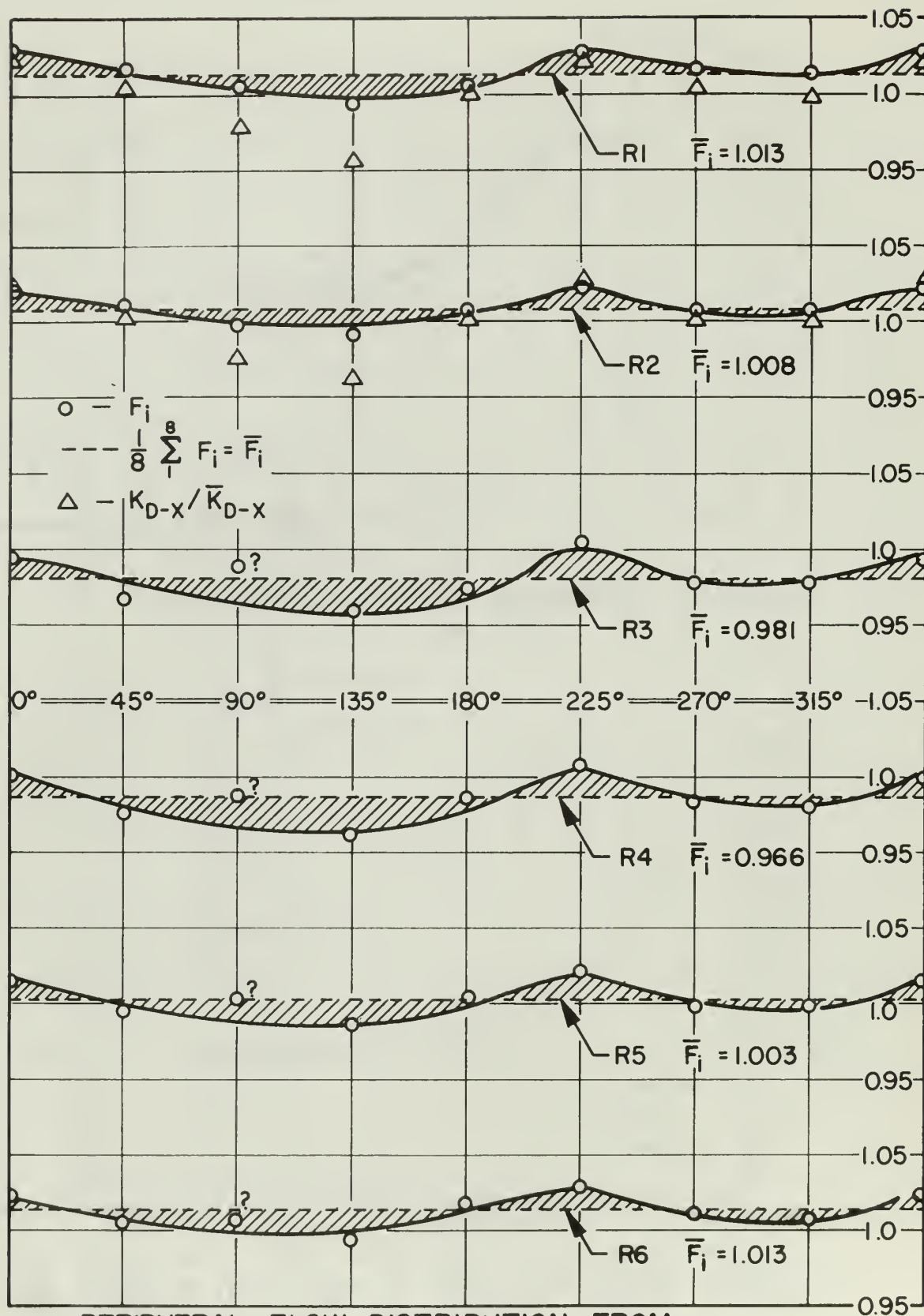
FIG. 28
SCHEMATIC OF TEST INSTALLA-
TION FOR GEOMETRICALLY
SIMILAR MODEL OF PLANE
W TO PLANE X



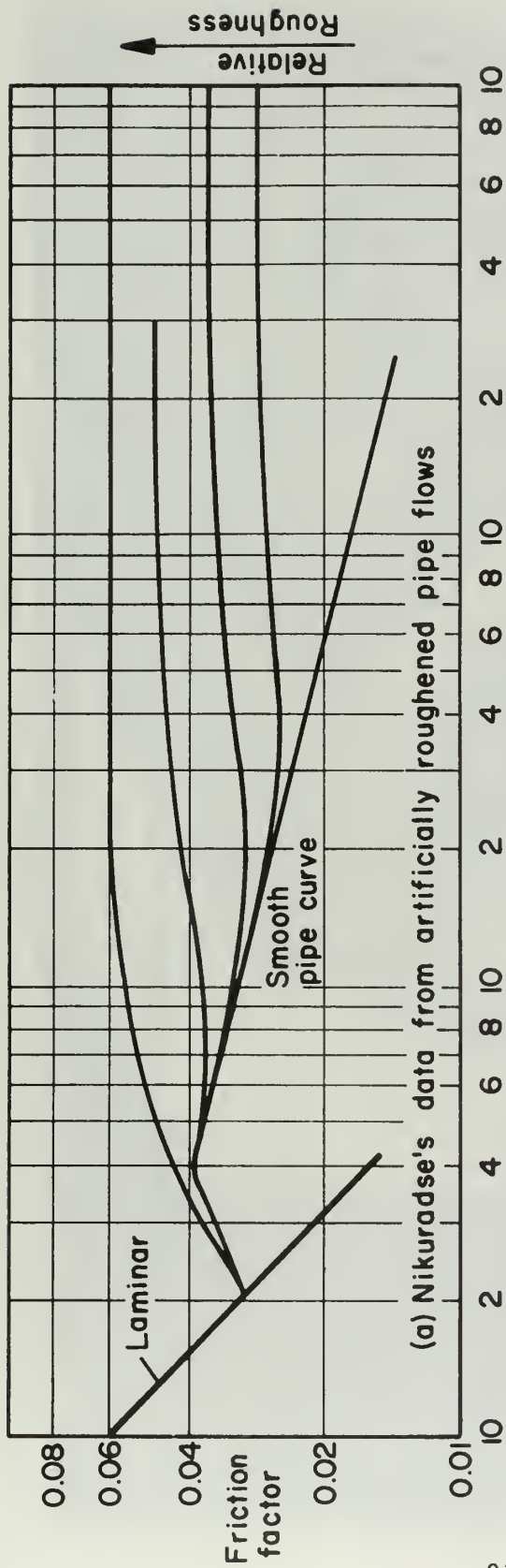
ORIFICE DISCHARGE COEFFICIENT VS Re
FIG. 29



TOTAL PRESSURE LOSS PLANE D TO PLANE X VS Re
FIG. 30



PERIPHERAL FLOW DISTRIBUTION FROM
 PLANE D TO PLANE X.
 FIG. 31



93

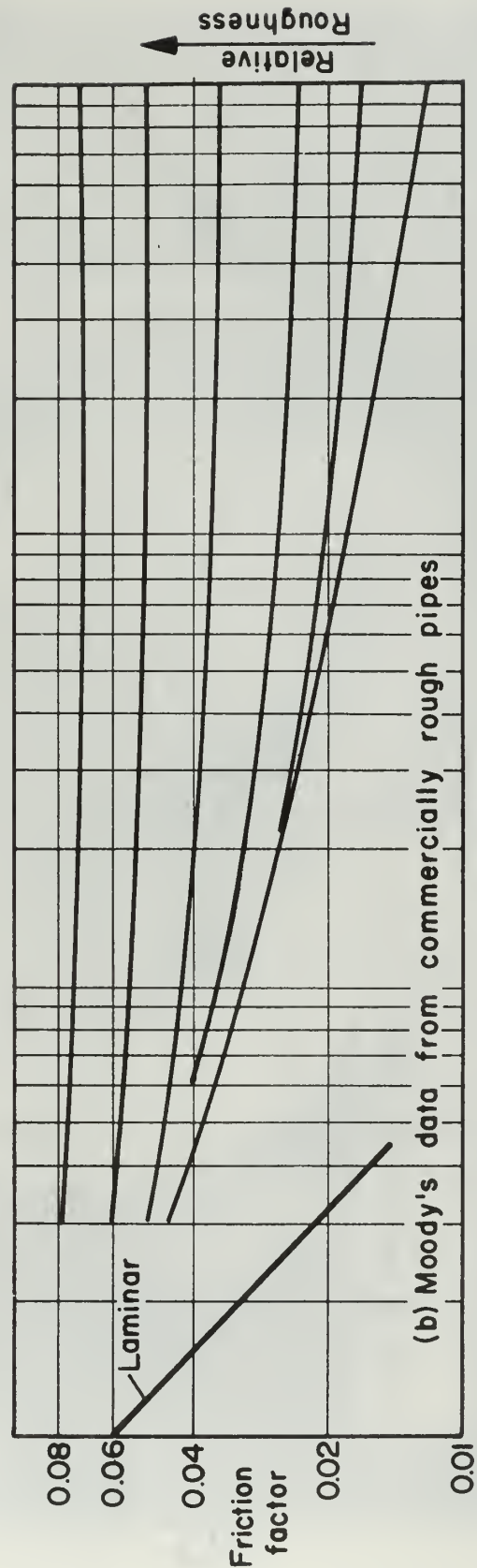


FIG. 32
FRICTION FACTORS FOR FLOW IN PIPES

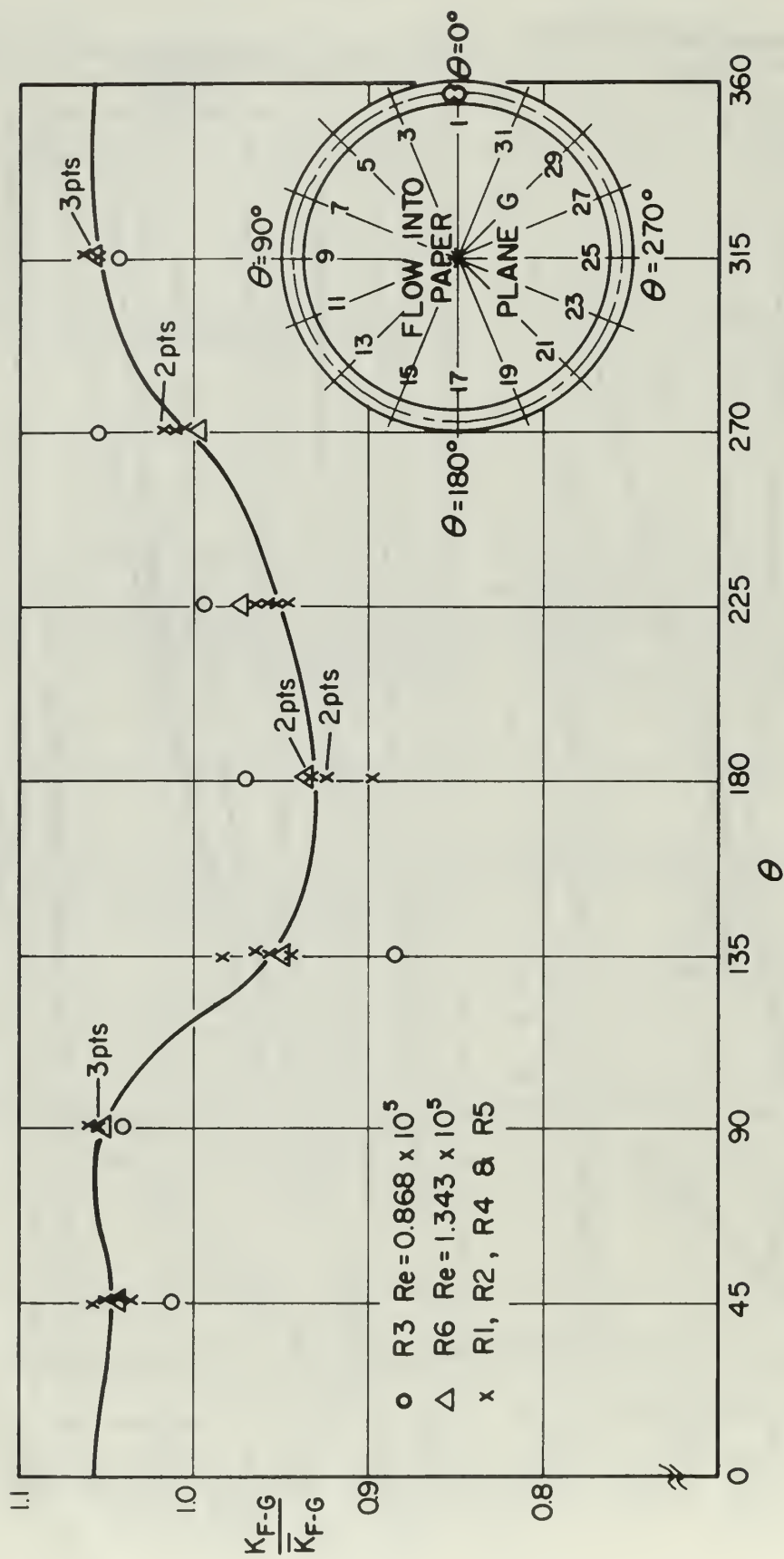
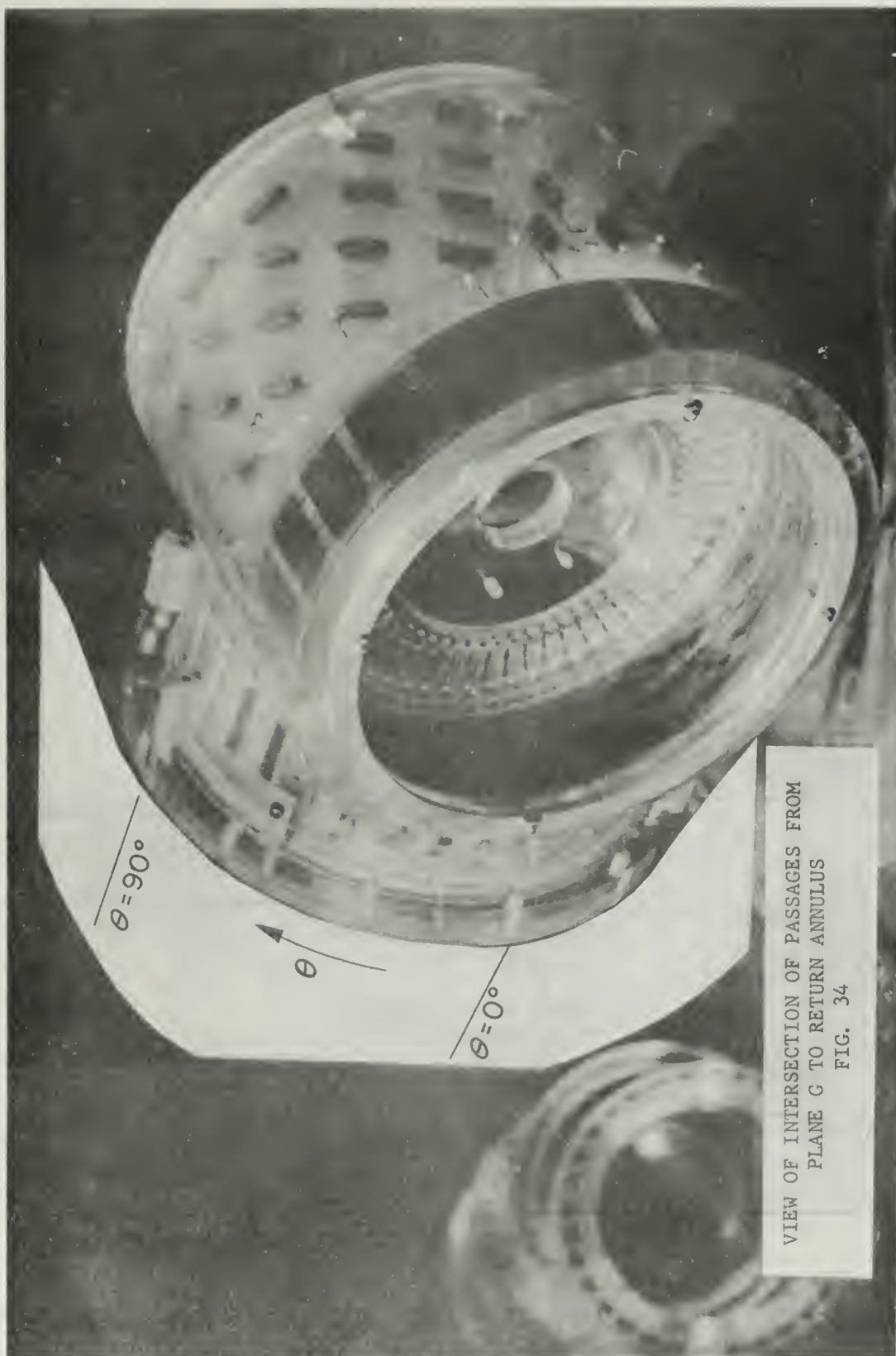
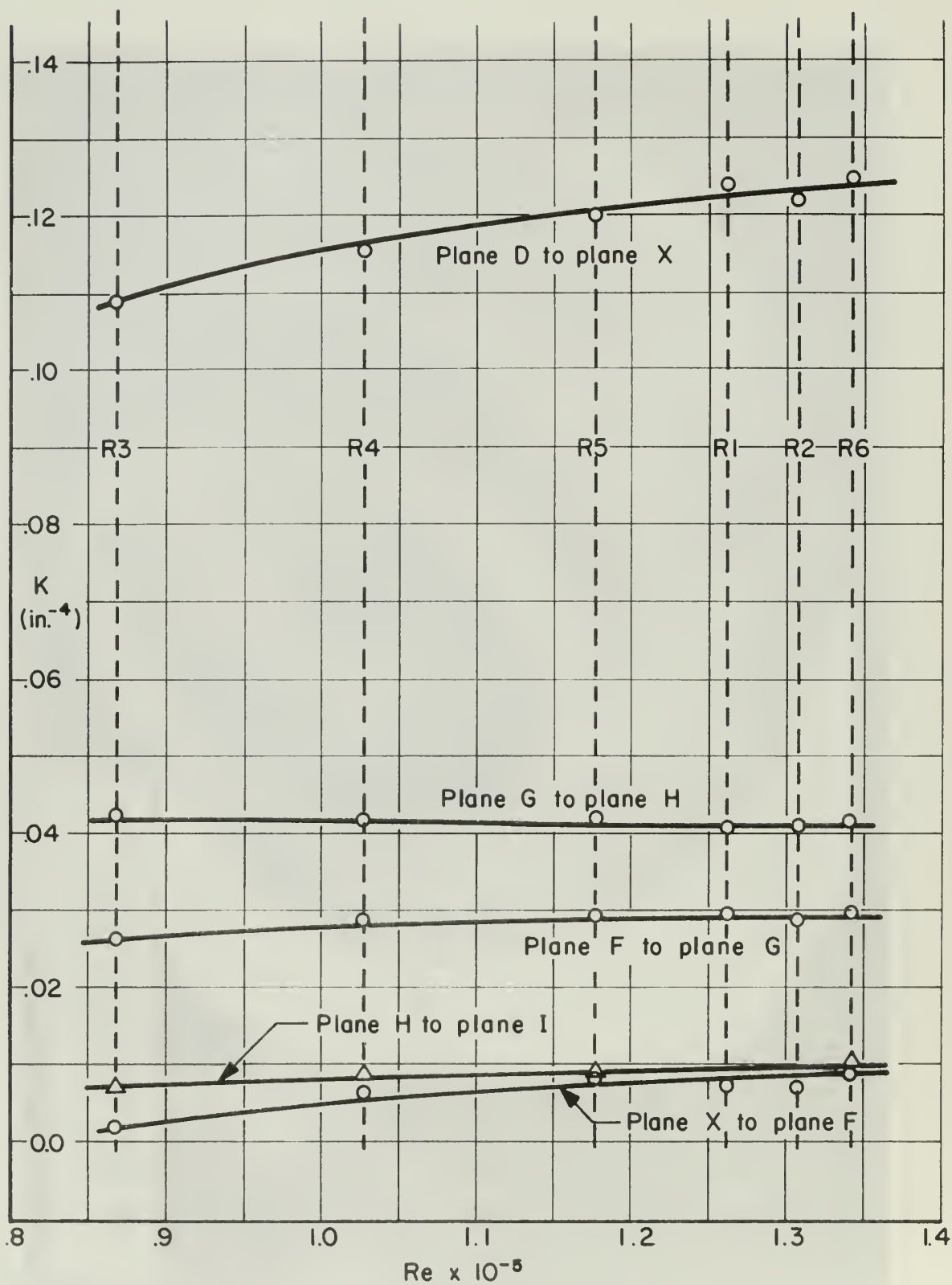


FIG. 33
PERIPHERAL DISTRIBUTION OF LOSS COEFFICIENT
PLANE G, RUNS R1 THRU R6.

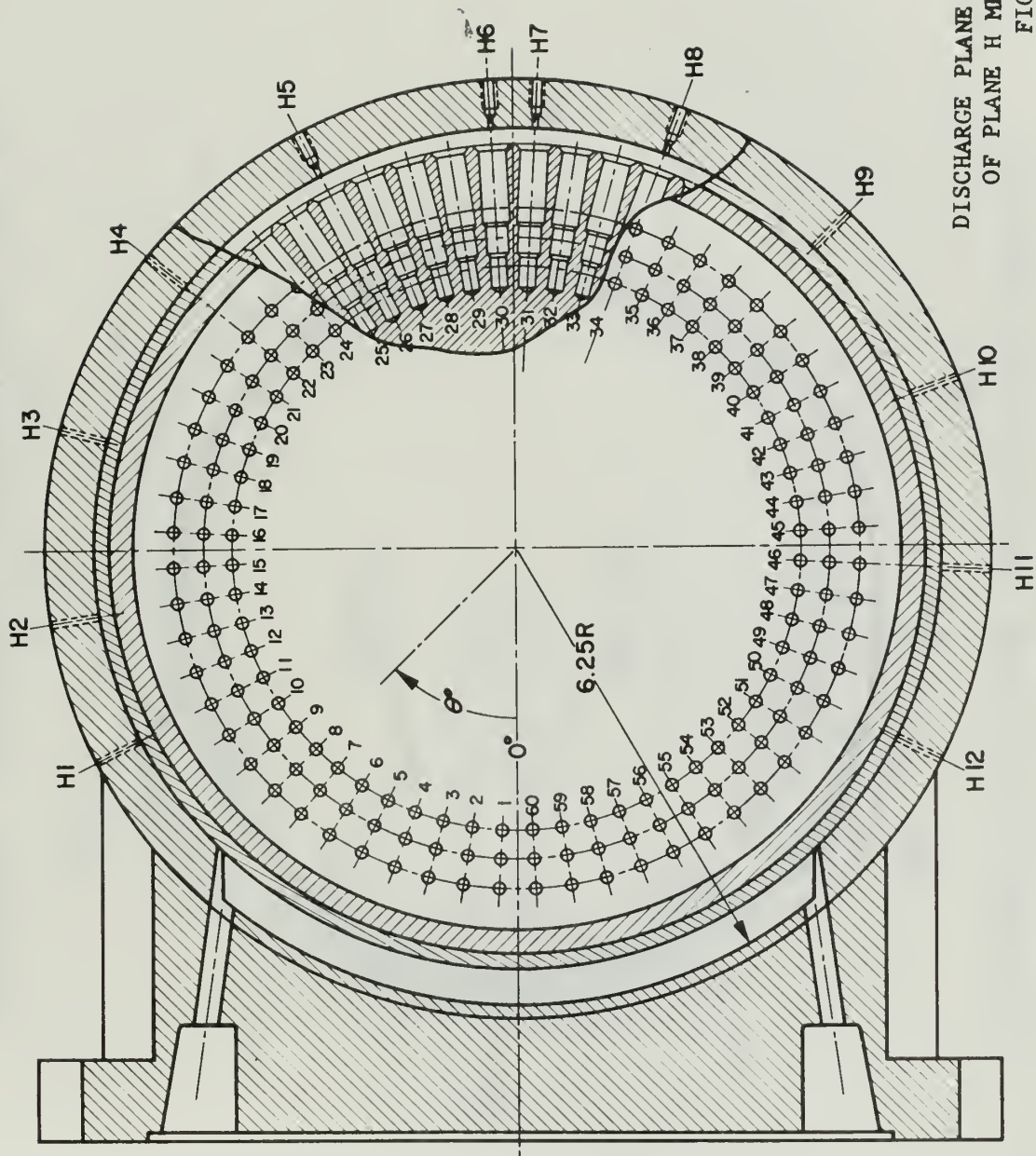


VIEW OF INTERSECTION OF PASSAGES FROM
PLANE G TO RETURN ANNULUS
FIG. 34

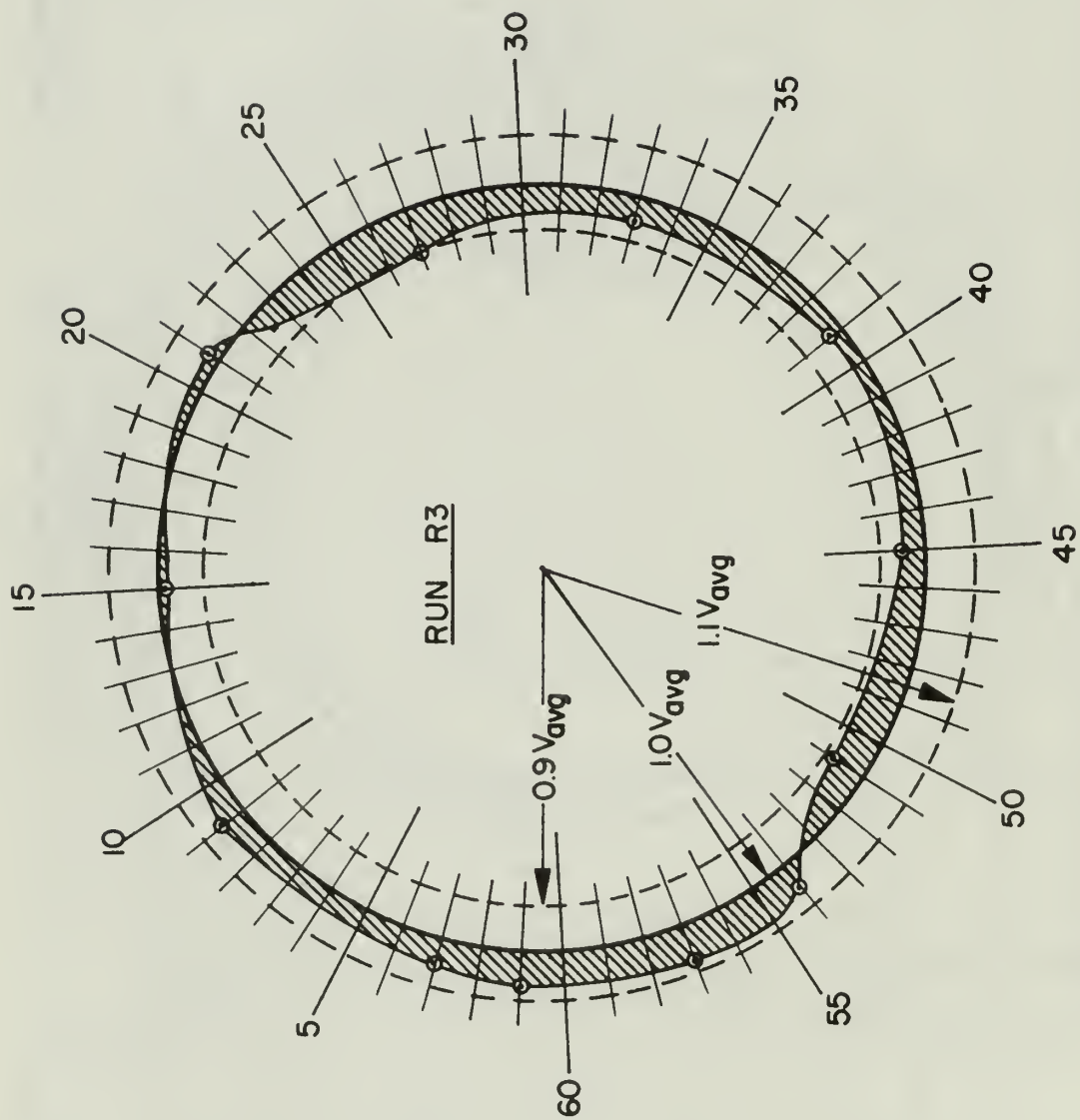


AVERAGE LOSS COEFFICIENTS RETURN SUB-ASSEMBLY
VS REYNOLDS NO.

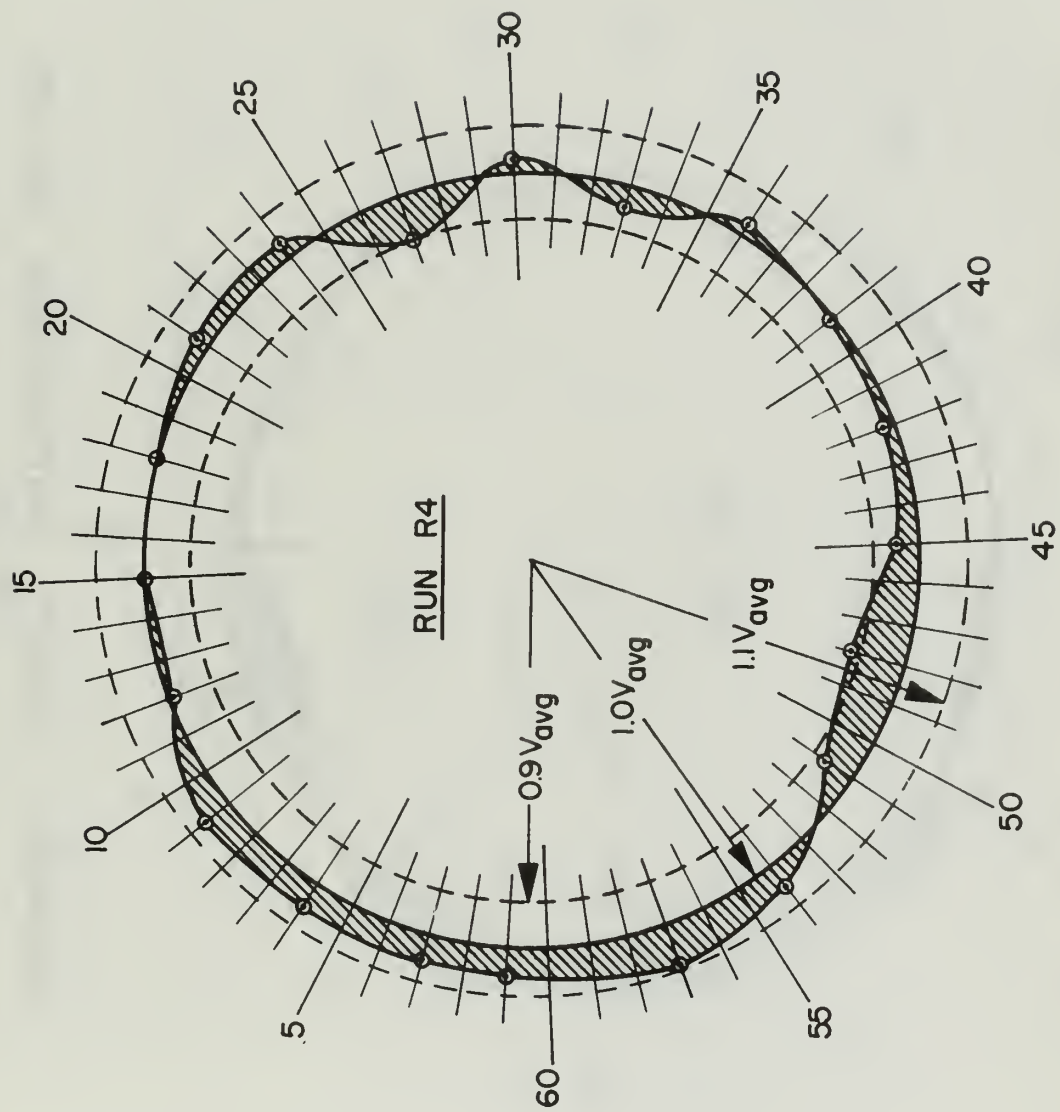
FIG. 35



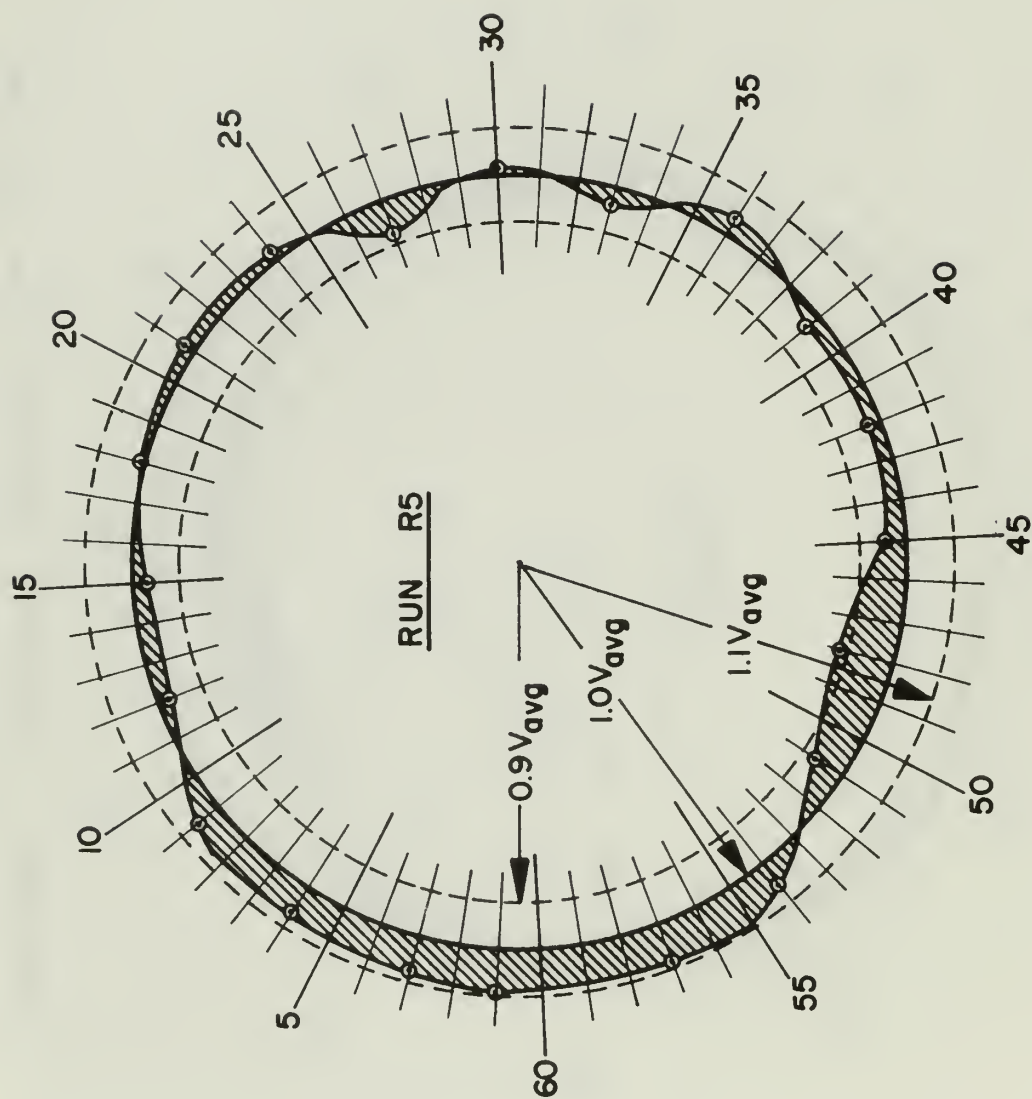
DISCHARGE PLANE I AND LOCATION
OF PLANE H MEASURING TAPS
FIG. 36



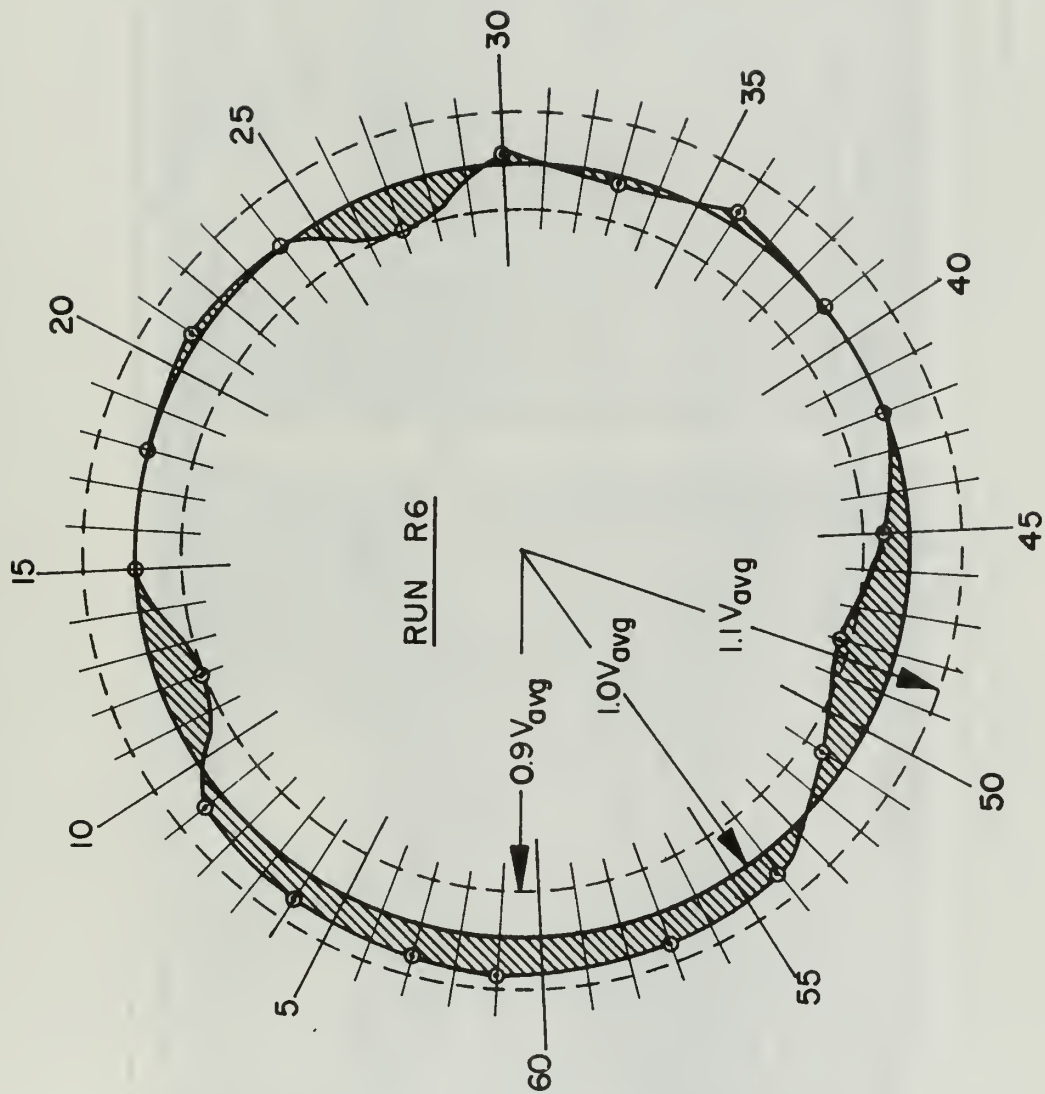
DISCHARGE VELOCITY DISTRIBUTION RUN R3
FIG. 37



DISCHARGE VELOCITY DISTRIBUTION RUN R4
FIG. 38



DISCHARGE VELOCITY DISTRIBUTION RUN R5
FIG. 39



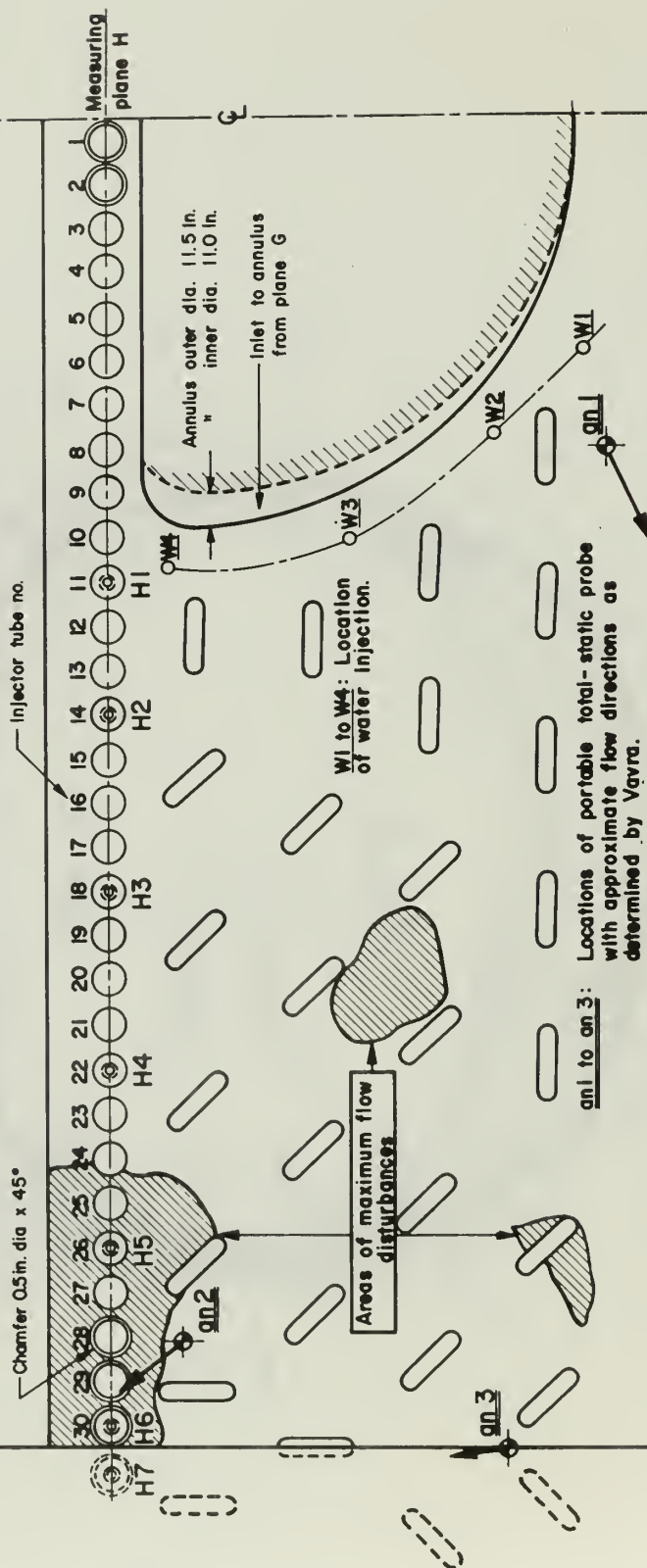
DISCHARGE VELOCITY DISTRIBUTION RUN R6
FIG. 40

FIG. 41

ONE HALF OF RETURN ANNULUS DEVELOPED INTO PLANE

SHOWING:

1. Location of turning vanes.
2. Location of radial holes & static taps in plane H.
3. Location of water injection holes for flow visualization.



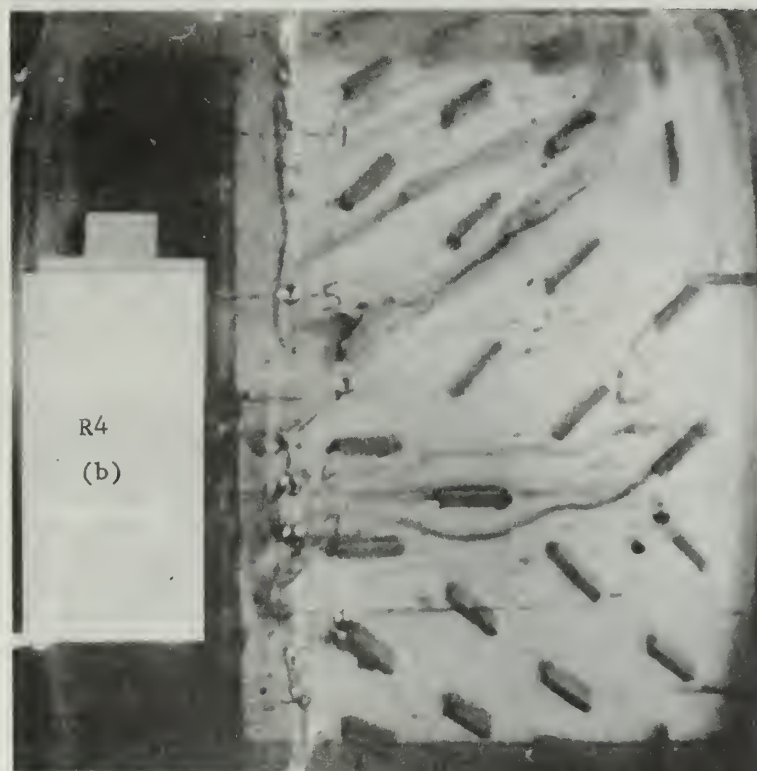


FIG. 42 FLOW IN RETURN ANNULUS RUN R4

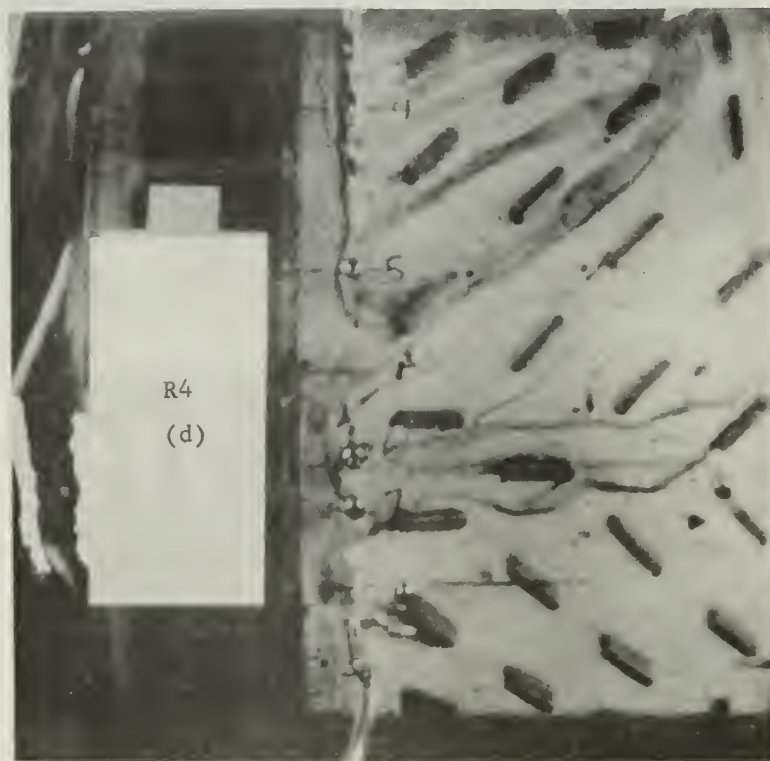
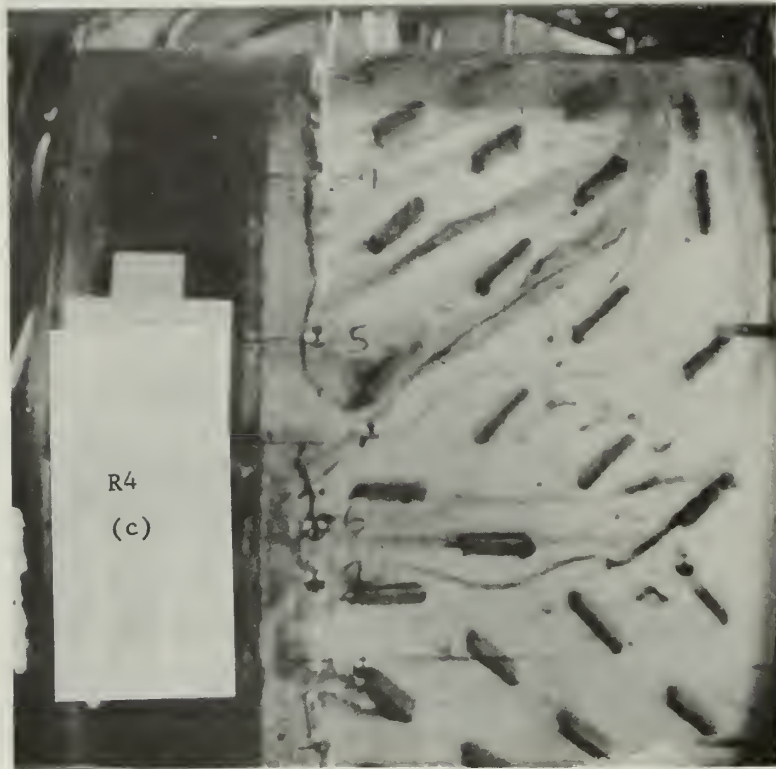


FIG. 42 (con't) FLOW IN RETURN ANNULUS RUN R4

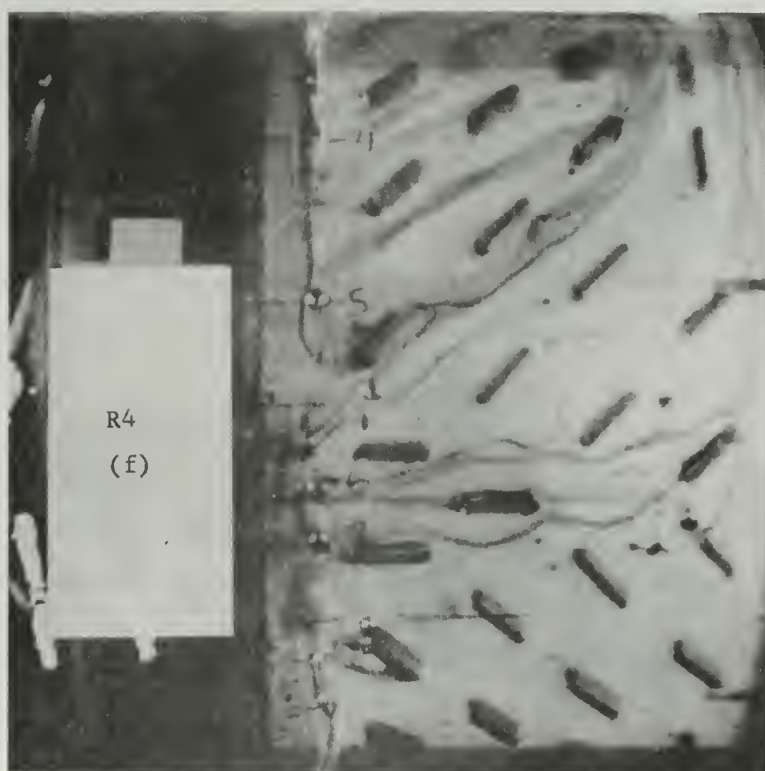
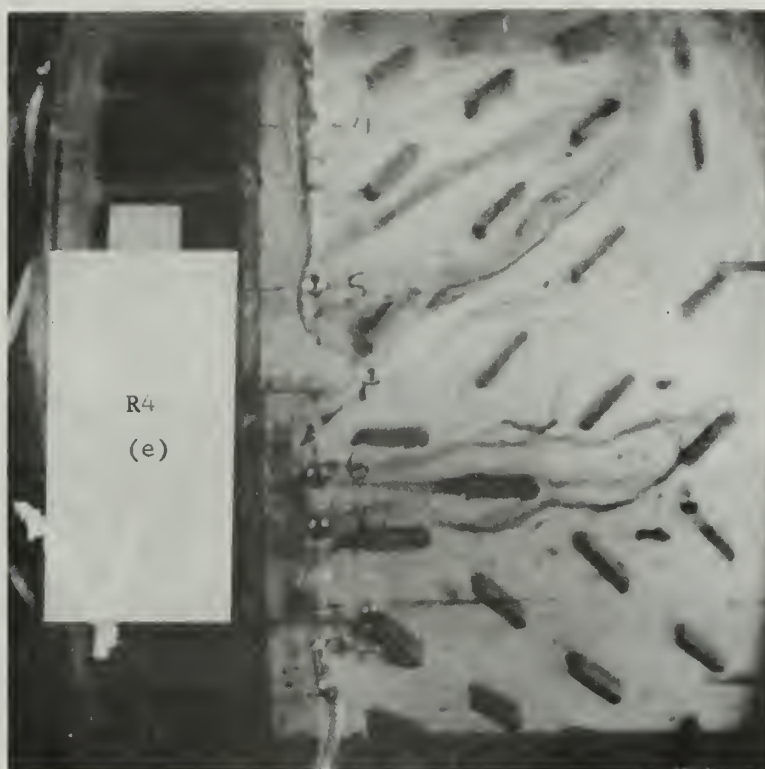


FIG. 42 (con't) FLOW IN RETURN ANNULUS RUN R4

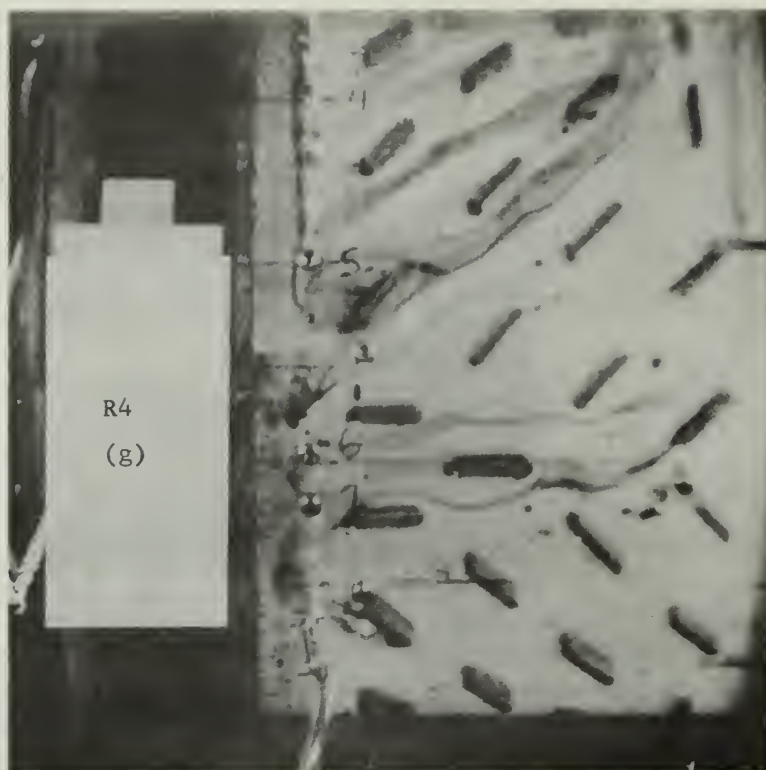


FIG. 42 (con't) FLOW IN RETURN ANNULUS RUN R4

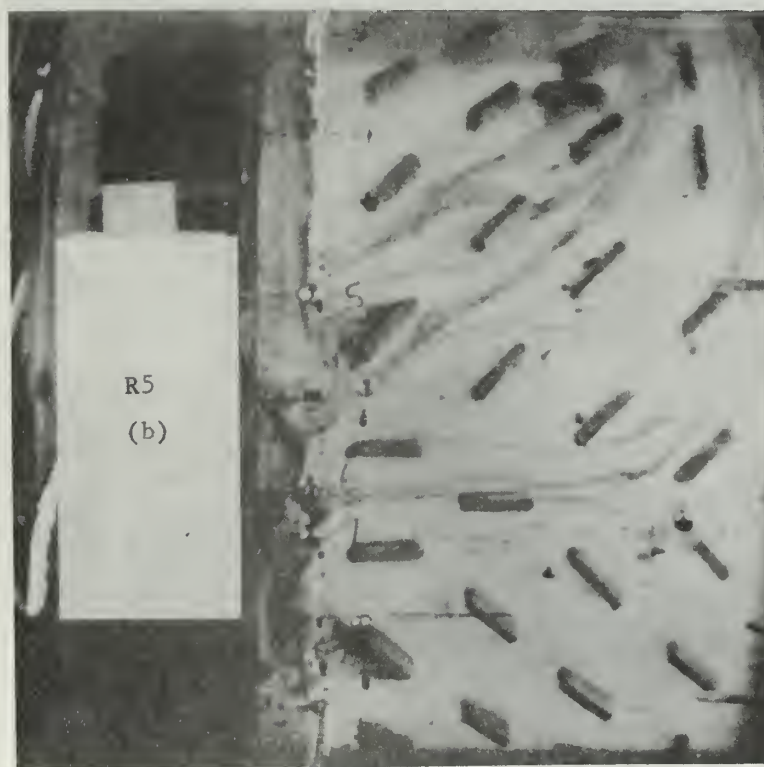
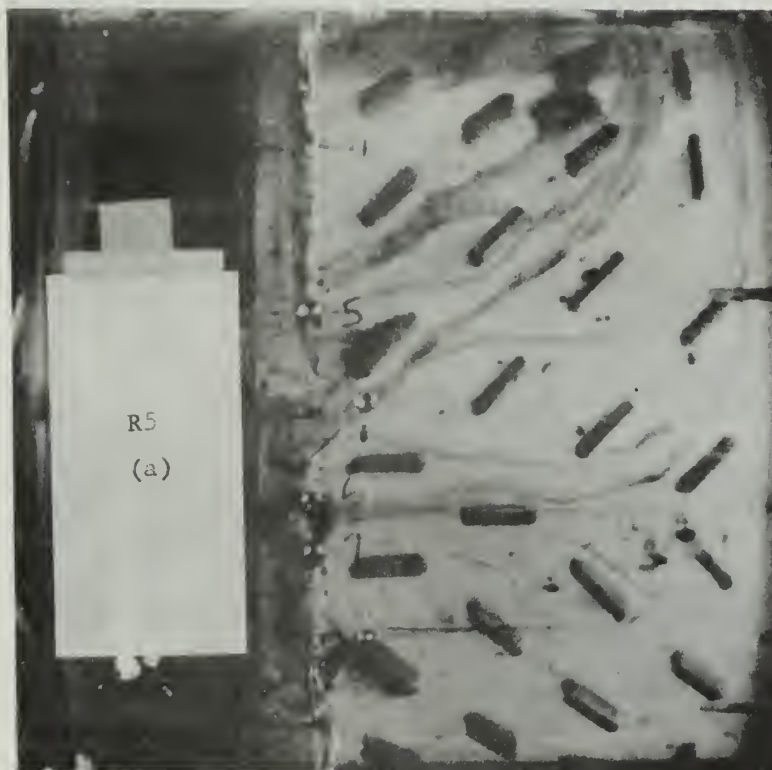


FIG. 43 FLOW IN RETURN ANNULUS RUN R5

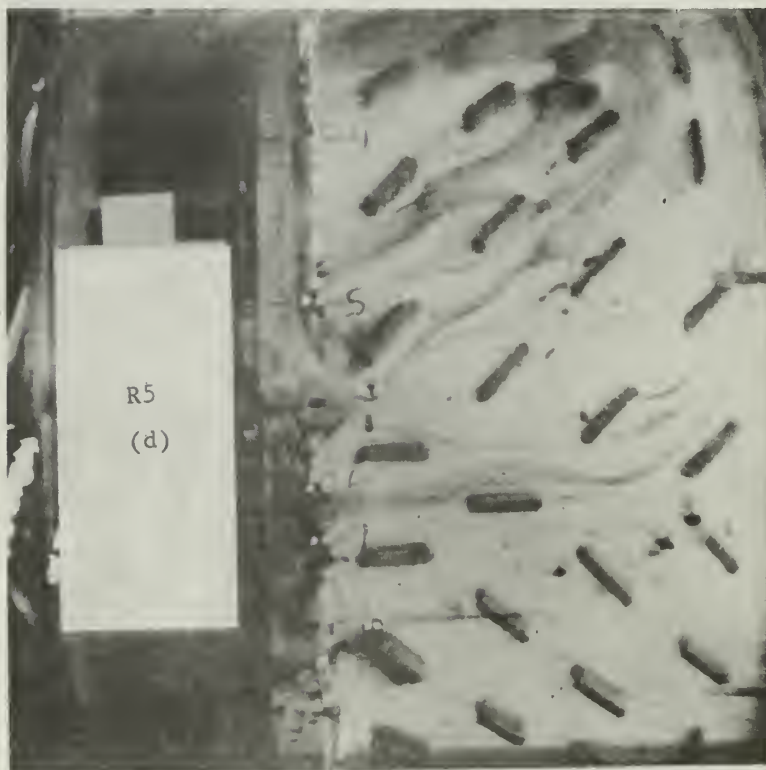
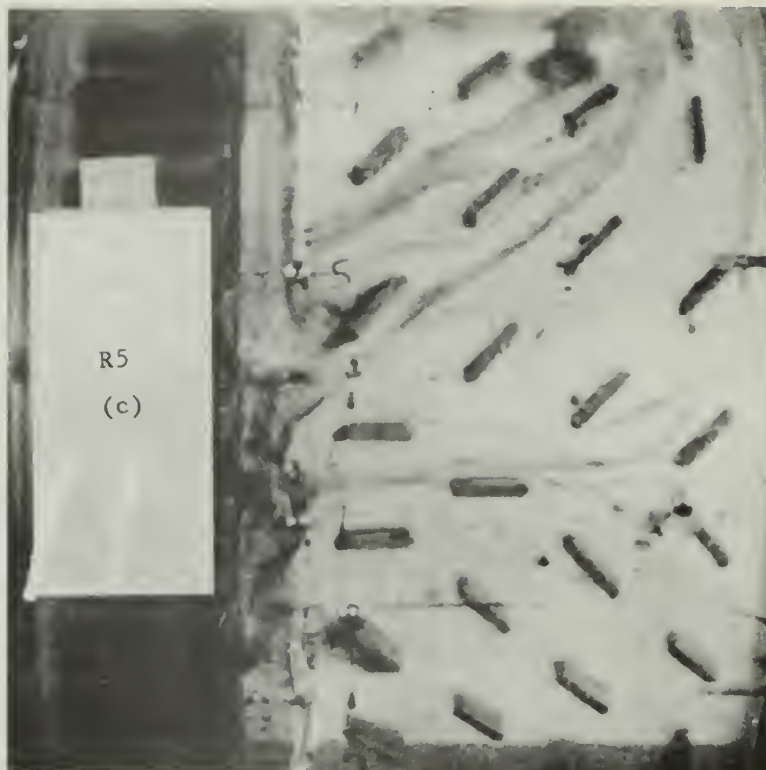


FIG. 43 (con't) FLOW IN RETURN ANNULUS RUN R5

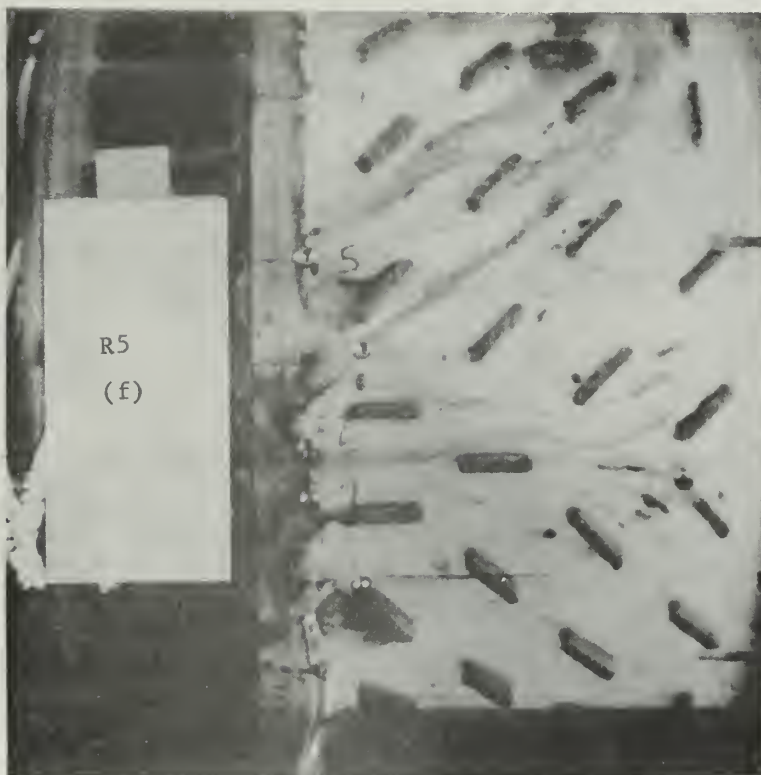
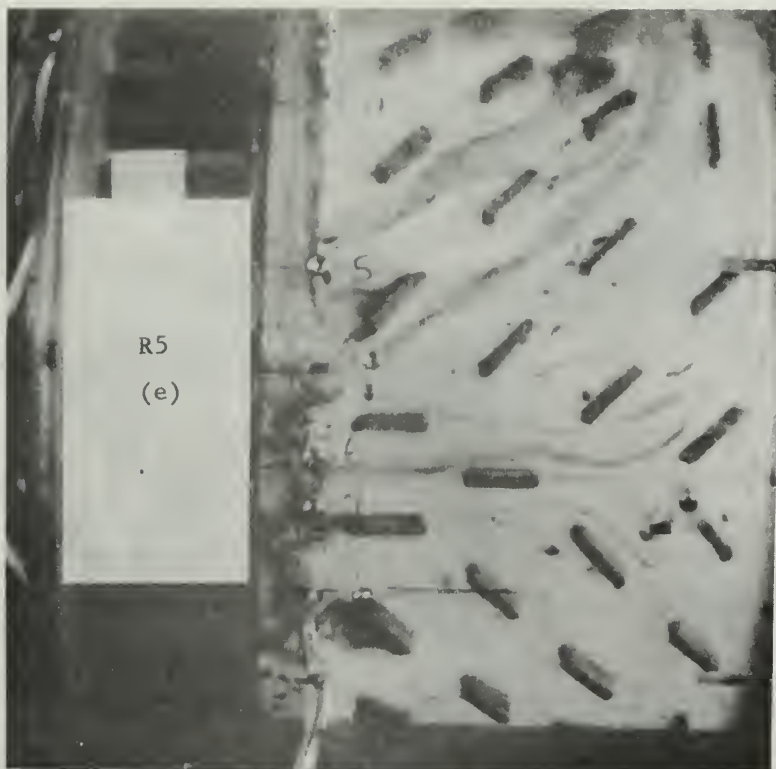


FIG. 43 (con't) FLOW IN RETURN ANNULUS RUN R5

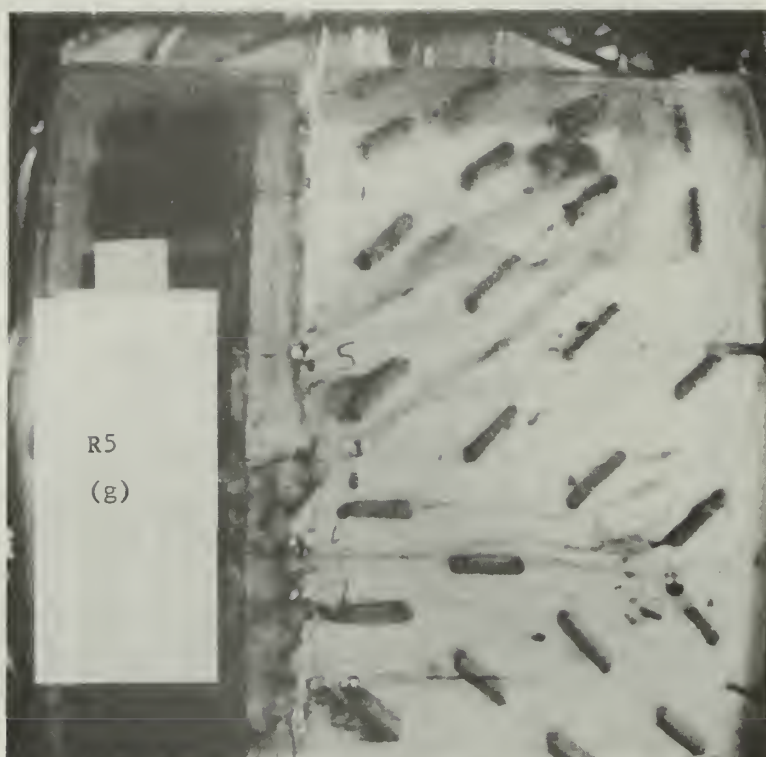
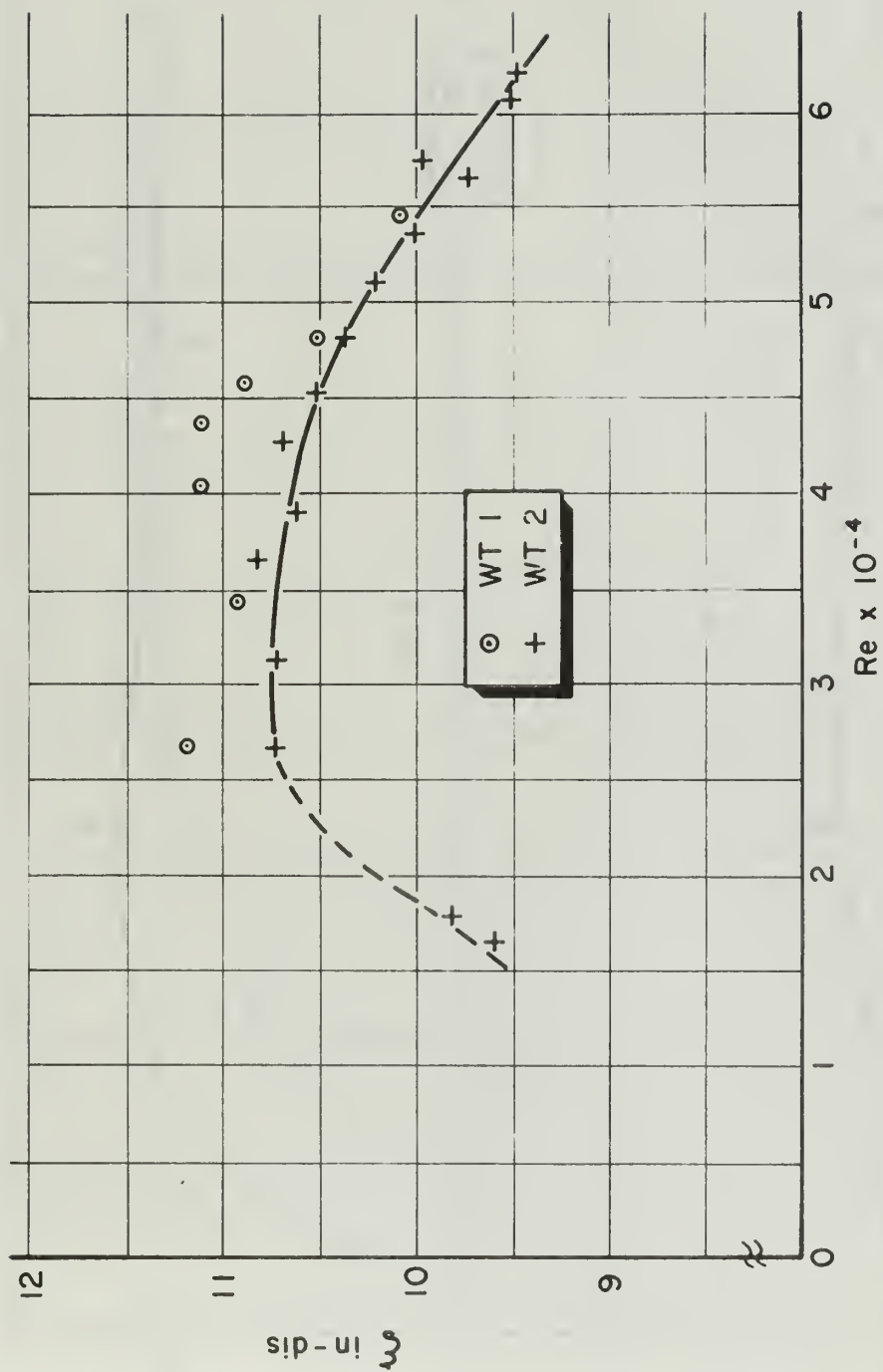
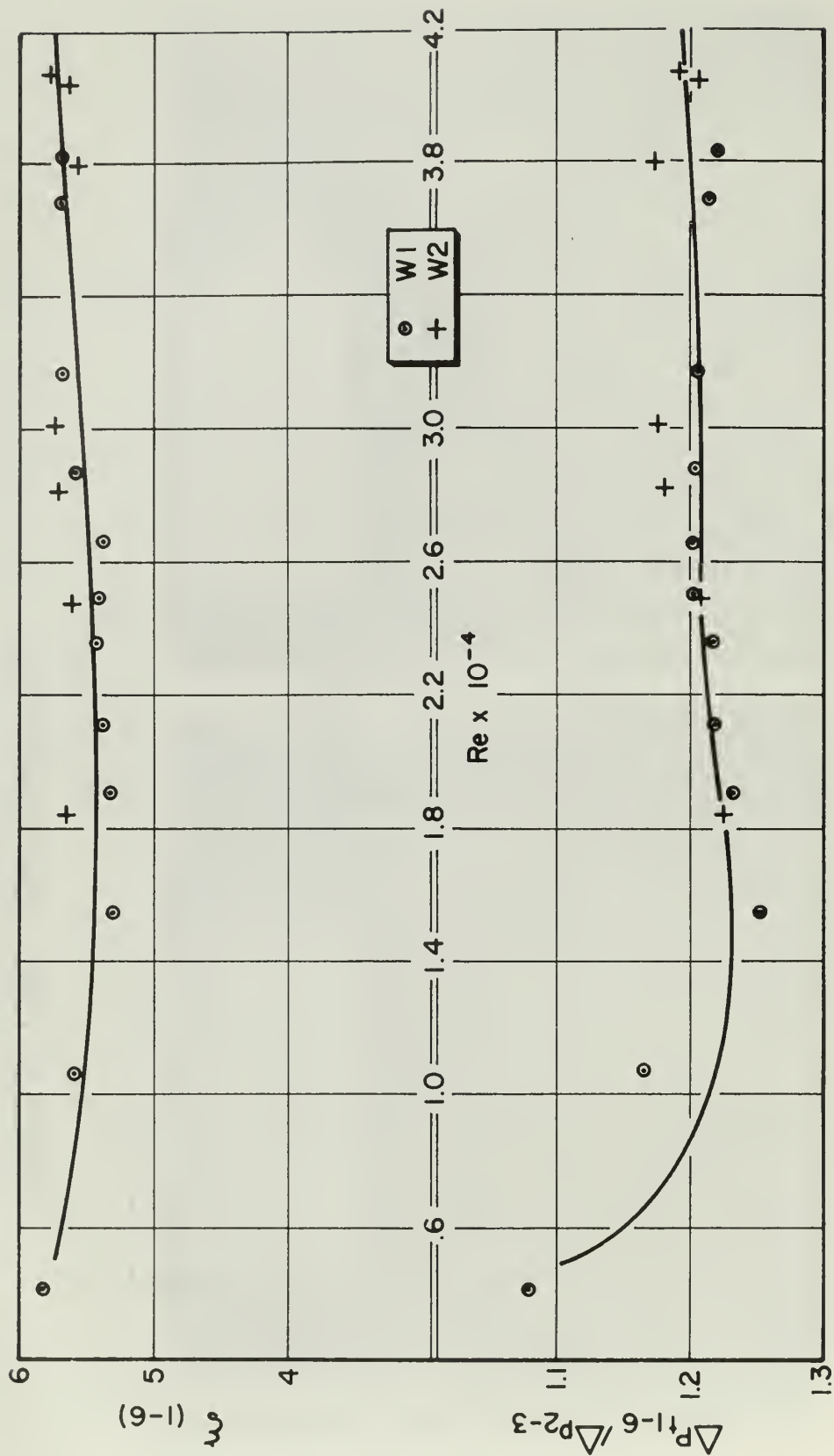


FIG. 43 (con't) FLOW IN RETURN ANNULUS RUN R5



NOZZLE TUBE LOSS COEFFICIENT VS REYNOLDS NO.

FIG. 44

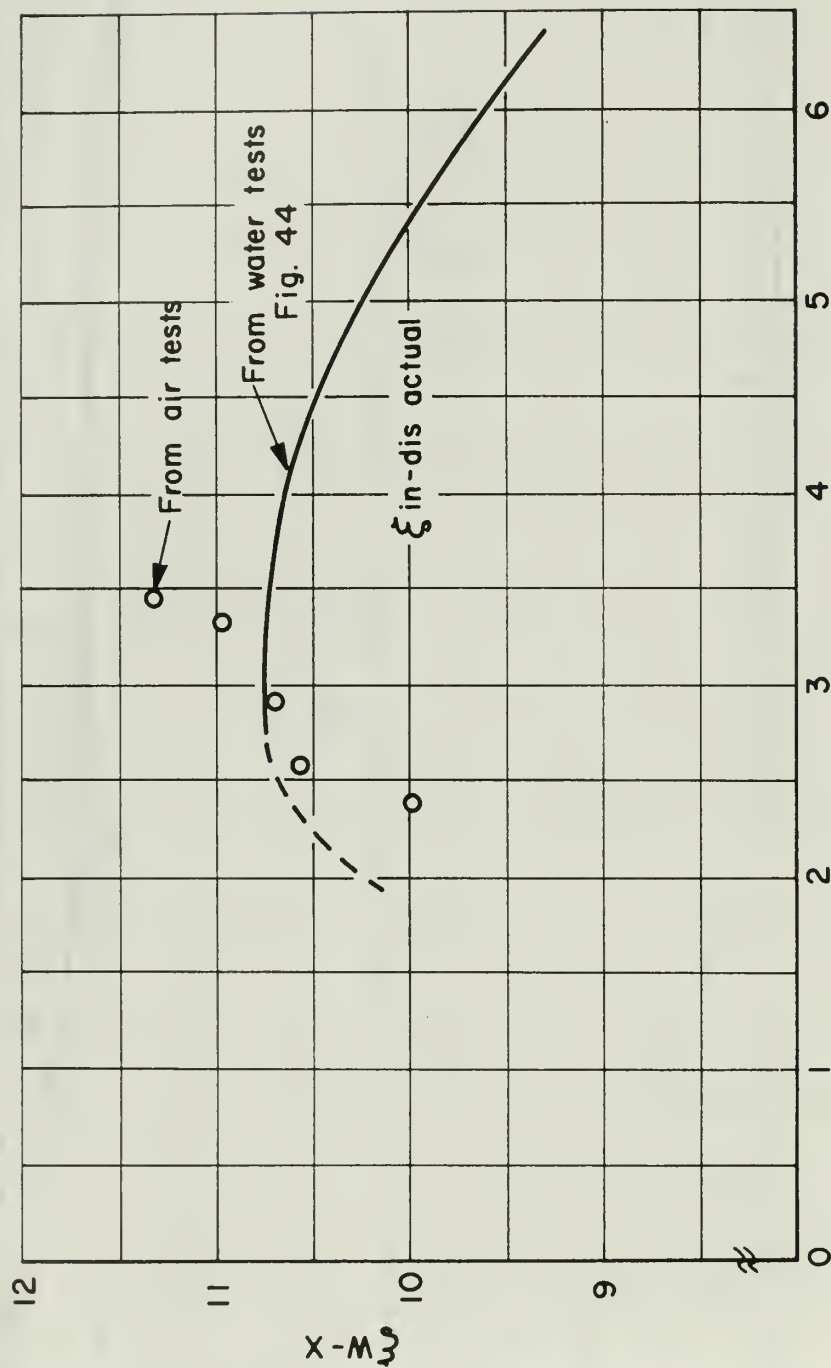


FRICION FACTOR VS REYNOLDS NO. FOR RUNS W1 AND W2

FIG. 45



FRICION FACTOR VS REYNOLDS NO. FOR RUN W3
FIG. 46



LOSS COEFFICIENT ξ_{w-x} VS REYNOLDS NO.

FIG. 47

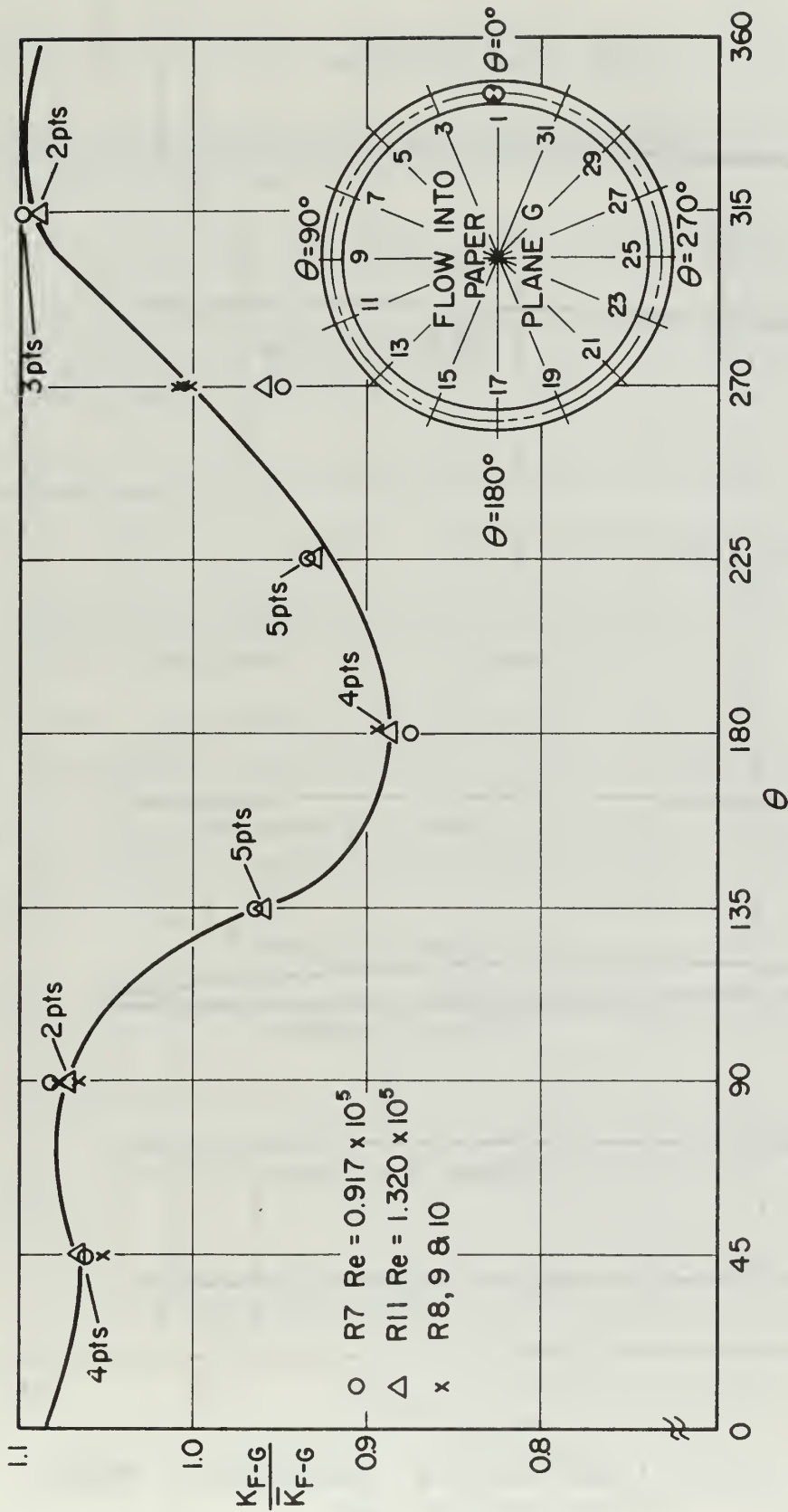
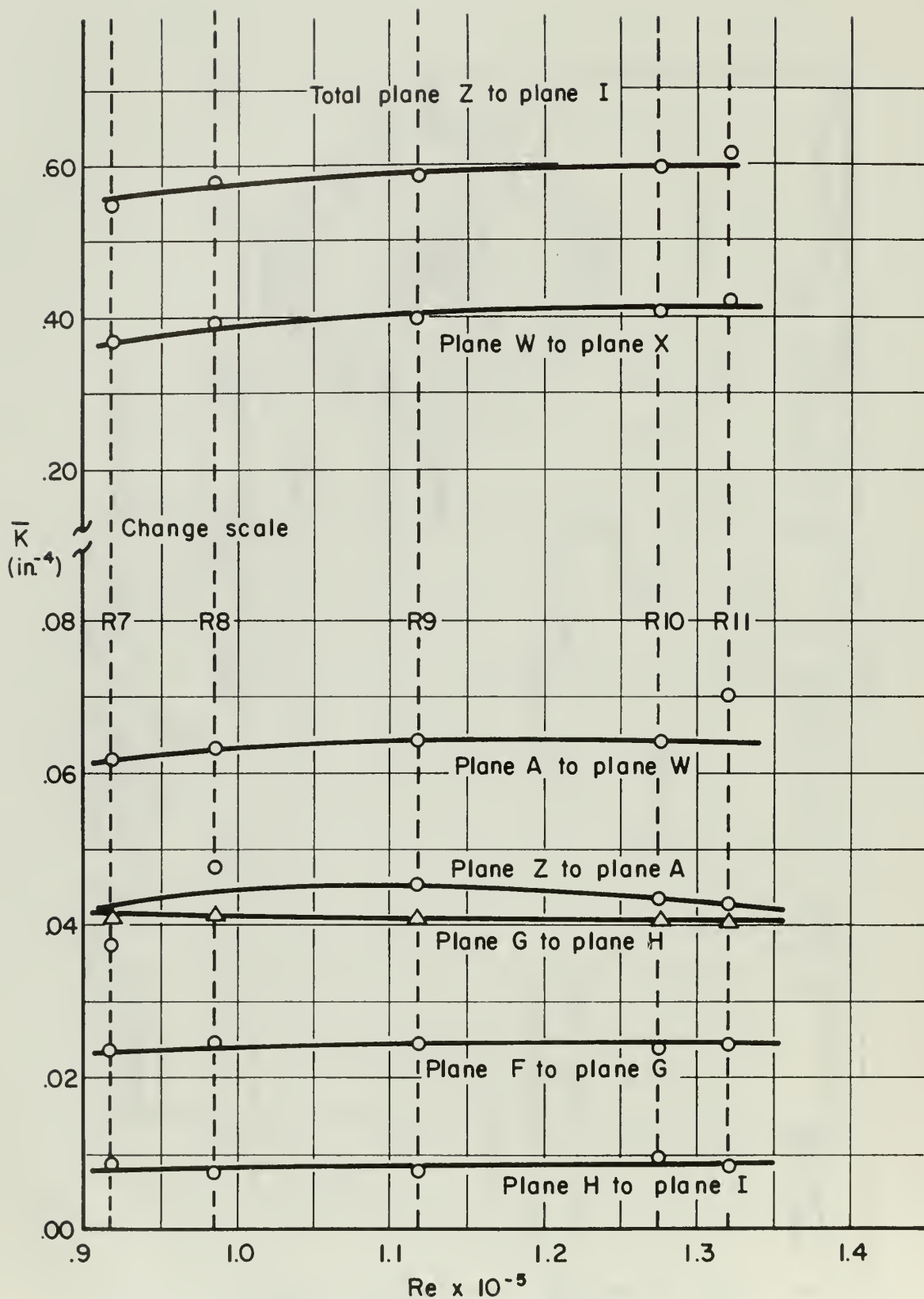


FIG. 48
PERIPHERAL DISTRIBUTION OF LOSS COEFFICIENT
PLANE G, RUNS R7 THRU R11.



AVERAGE LOSS COEFFICIENTS ASSEMBLED MODEL
VS REYNOLDS NO.

FIG. 49

SECTION 8

BIBLIOGRAPHY

1. Vavra, M. H. "Results of Fluid Dynamic Model Tests of ARES Turbine Inlet Passage (Model h)," Report ARES VA-T No. 7, for Aerojet-General Corporation, 1966.
2. Vavra, M. H. "Air Test of MOD 1 ARES Turbine," Report ARES VA-T No. 8, for Aerojet-General Corporation, 1966.
3. Messegee, J. A. "Influence of Axial and Radial Clearances on the Performance of a Turbine Stage with Blunt Edge Non-twisted Blades," Thesis, Naval Postgraduate School, 1967.
4. Vavra, M. H. "Tests of ARES Oxidizer Return Passages," Report ARES VA-T No. 10, for Aerojet-General Corporation, 1966.
5. VDI Durchfluss Messregeln. DIN 1952, VDI Verlag, Berlin, 1943.
6. Kelly, R. J. "Data for Flow Rate Measurements in Addition of Building 230 (Propulsion Laboratory, Department of Aeronautics)", Library, Naval Postgraduate School, 1967.
7. Shames, I. H. Mechanics of Fluids, McGraw-Hill, Inc., 1962, p. 191.
8. Supplement to ASME Power Test Code, Chap. 4, Part 5, ASME, New York, 1959.
9. Schlichting, H. Boundary Layer Theory, McGraw-Hill, Inc., 1960, pp. 517-529.

APPENDIX A

DERIVATION OF FLOW MEASURING EQUATION

The pressure drop $P_u - P_d$ across the flow nozzle is referred to the absolute pressure P_u upstream and is to enter calculations in the dimensionless form $\frac{P_u - P_d}{P_u}$. Thus any consistent unit of pressure may be used.

The equation for flow rate \dot{w} (lb_m/sec)¹ is

$$\dot{w} = \alpha Y_1 A_d f_t f_r \sqrt{2 g \rho_u (P_u - P_d)} \quad (A1)$$

where:

α - nozzle discharge coefficient (independent of Re)

Y_1 - expansion factor to account for compressibility effects

A_d - area based on nozzle diameter (in.²) = 7.17263 in.²

f_t - area multiplier to account for the thermal expansion of the nozzle

f_r - Reynolds number correction factor

g - 32.17 ft/sec²

ρ_u - upstream density (lb_m/ft³)

P_u - pressure upstream (lb/in.²)

P_d - pressure downstream (lb/in.²)

Using the equation of state for a perfect gas

$$\rho_u = \frac{P_u (144)}{R T_u} \quad (A2)$$

¹VDI Durchfluss Messregeln. DIN 1952, VDI Verlag, Berlin, 1943, p. 5.

where $R = 53.35 \text{ ft-lb/lb}_m^{\circ}\text{R}$, and T_u is the upstream temperature ($^{\circ}\text{R}$), equation (A1) can be rearranged to give the equivalent flow rate

$$w_u^* = \frac{\dot{w} \sqrt{T_u}}{P_u} \sqrt{\frac{R}{g}} = Y_1 A_d f_t f_r \sqrt{\frac{P_u - P_d}{P_u}} \quad (\text{in}^2) \quad (\text{A3})$$

The dimensionless coefficients must be investigated for the nozzle with diameter ratio $\beta = 0.7434$ and $m = \beta^2 = 0.552$ where $\beta = d/D$.

The discharge coefficient² \propto for $m = 0.552$ is found to be 1.114.

The density coefficient Y_1 is obtained from the ASME³ standards.

For air with $\gamma = c_p/c_v = 1.4$ and $\beta = .743$ using $x = \frac{P_u - P_d}{P_u}$ there is

$$Y_1 = \sqrt{2.433 \frac{(1-x)^{1.428}}{x} \left\{ \frac{1 - (1-x)^{0.286}}{1 - 0.305 (1-x)^{1.428}} \right\}} \quad (\text{A4})$$

For stainless steel the area multiplier f_t can be expressed by⁴

$$f_t = 1.0 + 0.0015 \left\{ \frac{t_u - 60}{100} \right\} \quad (\text{A5})$$

The design of the nozzle is such that $f_r = 1$ for all pressure ratios.

Combining the above quantities equation (A3) becomes

$$w_u^* = \frac{\dot{w} \sqrt{T_u}}{P_u} \sqrt{\frac{R}{g}} = 11.3 Y_1 \sqrt{\frac{P_u - P_d}{P_u}} \quad (\text{A6})$$

²Ibid. Appendix 6.

³Supplement to ASME Power Test Codes, Chap. 4, Part 5, ASME, New York, 1959, p. 76.

⁴Stearnes, R. F. et. al. Flow Measurements with Orifice Meters, Van Nostrand Co., Inc., New York, 1951, p. 257.

APPENDIX B

DATA REDUCTION FOR AIR AND WATER TESTS WITH FLOW CHANNEL

B. 1 Air Tests

A total of seven data points was observed. The quantities measured were:

H_u - pressure upstream of flow measuring orifice against atmosphere (in.Hg)

Δh_o - change in static pressure across orifice (in.H₂O)

t_u - temperature upstream of orifice (°F)

t_{plen} - temperature in plenum 2 (°F)

H_{atm} - manometer reference (cm H₂O)

H_{in} - inlet total pressure at Kiel probe against atmosphere (cm H₂O)

H_{dis} - discharge total pressure against atmosphere (cm H₂O)

h_{atm} - 30.01 in.Hg

The equivalent flow rate w_u^* is given by equation (A6). It is convenient to use the model inlet as a reference condition. Then the equivalent flow rate is

$$w_{in}^* = w_u^* \frac{P_u}{P_{t_{in}}} \sqrt{\frac{T_{t_{in}}}{T_u}} \quad (in^2) \quad (B1)$$

where $P_u = P_{t_u} = 0.49112 \left\{ H_u + 30.01 \right\} \quad (lb/in^2)$

$$P_{in} = P_{t_{in}} = 0.49112 \left\{ 0.02894 (H_{atm} - H_{in}) + 30.01 \right\} \quad (lb/in^2)$$

Reynolds number Re based on inlet diameter d is

$$Re = \frac{V d \rho}{\mu g} = \frac{4 \dot{w}}{\pi \mu g} \quad (B2)$$

Equation (B2) can be rewritten as

$$Re = w_{in}^* \frac{P_{in}}{\sqrt{T_{t_{in}}}} \frac{4 (12)}{\pi d \mu \sqrt{Rg}} \quad (B3)$$

Air temperature for these tests varied between 85 and 95°F. Introducing a representative viscosity of 3.9×10^{-7} lb-sec/ft², in addition to other non-varying quantities, into equation (B3) gives

$$Re = w_{in}^* \frac{P_{in}}{\sqrt{T_{t_{in}}}} (4.728 \times 10^5) \quad (B4)$$

The loss coefficient is determined by

$$k_{in-dis} = \frac{P_{in} - P_{t_{dis}}}{P_{in}} \bigg/ (w_{in}^*)^2 \quad (in^{-4}) \quad (B5)$$

where $P_{t_{dis}} = 0.49112 \left\{ 0.02894 (H_{atm} - H_{t_{dis}}) + 30.01 \right\} (lb/in^2)$

B.2 Water Tests

A total of four runs was made, each consisting of several data points. The runs were numbered RMW 1, etc. The quantities measured were:

$P_{in\ g}$ - inlet static pressure (lb/in² gage)

W_t - weight of water (lb)

t - elapsed time (sec)

Volume flow rate V is obtained by

$$V = \frac{\dot{w} (100)}{3.6093} \quad (in^3 / sec) \quad (B6)$$

Re based on inlet diameter is

$$Re = \frac{V d_e}{\mu g} = \frac{V}{\pi/4 d \nu} \quad (B7)$$

where ν = kinematic viscosity, for water at $72^{\circ}\text{F} = 152.257 \text{ in}^2/\text{sec}$

Equation (B7) is reduced to

$$Re = V / 239.1645 \quad (\text{B8})$$

Because the inlet and discharge areas are equal

$$\Delta P_{t_{in-dis}} = \Delta P_{in-dis} = P_{in} g$$

The loss coefficient is determined by

$$k_{in-dis} = \frac{P_{in} g \gamma_L}{\dot{W}^2} = \frac{13.9403 P_{in}}{\dot{W}^2} \quad (\text{in}^{-4}) \quad (\text{B9})$$

where γ_L = specific weight of water at 72°F .

APPENDIX C

DATA REDUCTION FOR TESTS WITH ARES MODEL

C.1 General

Methods of data reduction used to obtain loss coefficients and other meaningful quantities from tests on the ARES model (as described in Section 5 of the main body), are discussed in the following Sections. They are listed in the same sequence as used for the performance of the tests.

C.2 Oxidizer Return Sub-assembly

The quantities necessary to obtain mass flow rate are identical to those described in Appendix B. The equivalent flow rate w_u^* is given by equation (A6). In addition the following quantities were recorded

H_{plen} - pressure in plenum 2 (cm H₂O)

$H_{\text{atm } 1}$ - atmospheric reference, manometer bank 1 (cm H₂O)

H_{in} - pressure at Kiel probe (cm H₂O)

H_D - pressure in plane D (cm H₂O)

h_{an} - static pressure at selected locations in annulus (in. H₂O)

H_{an} - total pressure at selected locations in annulus (in. H₂O)

$H_{\text{atm } 3}$ - atmospheric reference, manometer bank 3 (in. H₂O)

h_I - static pressure in plane I (in. H₂O)

H_I - total pressure in plane I (in. H₂O)

t_{plen} - temperature in plenum 2 (°F)

From the polaroid pictures the following quantities were read

h_E - static pressure in plane E at holes 7, 13, 20, 26, 33, 39, 46, 52 (cm H₂O)

h_F - static pressure in plane F at holes 1, 9, 17, 25 (cm H₂O)

H_G - total pressure in plane G between holes 32-1, 4-5, 9-10,
13-14, 17-18, 20-21, 25-26, 29-3 (cm H_2O)

h_H - static pressure in plane H above discharge holes 11, 14, 18,
22, 26, 30, 31, 34, 38, 42, 46, 50 (cm H_2O)

$$Re = w_u^* \frac{P_u}{\sqrt{T_u}} \frac{4(12)}{\pi(4.07)\sqrt{R_g}} \frac{1}{\mu} = w_u^* \frac{P_u}{\sqrt{T_u}} \frac{0.09062}{\mu} \quad (C1)$$

The loss coefficient k for flow between each plane is referred to an inlet condition. The equivalent flow rate must then be referred to conditions at intermediate planes. For example, an average equivalent flow rate at plane F is

$$\bar{w}_F^* = w_u^* \frac{P_u}{\bar{P}_{t_F}} \sqrt{\frac{T_D}{T_u}} \quad (C2)$$

where $\bar{P}_{t_F} = 0.49112 \left\{ 0.02894 (\overline{H_{atm 1}} - \overline{H_F}) \right\} + P_{atm} \text{ (lb/in}^2\text{)}$

T_D - temperature in plane D assumed to be the same as that in plenum 2

P_u and T_u - determined as in equation (B1).

In a similar fashion the equivalent flow rates \bar{w}_D^* , \bar{w}_G^* are determined.

A geometrically similar model of a tube section from plane D to plane X was tested by Vavra. Data from these tests plotted in Figs. 29 and 30 include the orifice discharge coefficient K , and the loss in total pressure \sum_{D-X} from plane D to plane X divided by the static pressure change across the orifice. For each orifice preceding a measuring tap in plane E, an equivalent flow rate is found by

$$w_{D_i}^* = K Y_i A_d \sqrt{2} \sqrt{\frac{P_D - P_E}{P_D}} \quad (C3)$$

where $A_d = 0.0363 \text{ in}^2$ (area of orifice opening).

P_E and P_D are determined as was \bar{P}_{t_F} above. For air with $\gamma = c_p/c_v = 1.4$ from

$$Y_i = 1.0 - 0.36 \frac{P_D - P_E}{P_D} \quad (C4)$$

Equation (C3) becomes

$$w_{D_i}^* = 0.05204 K Y_i \sqrt{\frac{P_D - P_E}{P_D}} \quad (C5)$$

Equation (B4) is modified to find Re referred to tube inlet diameter

$$Re = w_{D_i}^* \frac{P_D}{T_D} (0.323 \times 10^7) \quad (C6)$$

This relation contains a representative value of viscosity for the temperature range encountered in the tests. An iteration is carried out using equations (C5) and (C6). A value of K is assumed and equation (C5) is solved. Using this value of $w_{D_i}^*$, Re is calculated from equation (C6). A corrected value of K is then read from Fig. 29 and the process continued. Generally, one iteration is required only.

The peripheral flow distribution at the orifice plate is found from

$$F_i = (52) w_{D_i}^* / \bar{w}_D^* \quad (C7)$$

The total pressure \bar{P}_{t_x} is found from

$$\bar{P}_{t_x} = P_D - f_{D-x} (\bar{P}_D - P_E) \quad (C8)$$

where f is read from Fig. 30 for the Re found with equation (C6). It is possible also to estimate \bar{P}_{t_E} by using equation (C7) with $f = 0.48$, a standard value for sharp edge orifices with $\beta = 0.72$.

The flow area in plane E is 3.676 sq. in. It is possible to find an average area restriction factor $\bar{\phi}_E$. The equation of continuity for average conditions is

$$\bar{V} = \frac{\dot{W}}{\bar{\rho} A \bar{\phi}} \quad (C9)$$

Also

$$\bar{\rho} \frac{\bar{V}^2}{2} = g \{ \bar{P}_t - \bar{P} \} \quad (C10)$$

Combining equations (C9) and (C10) gives

$$\frac{\dot{W}^2}{\bar{\rho} A^2 \bar{\phi}^2} = 2 g \{ \bar{P}_t - P \} \quad (C11)$$

Using the equation of state for a perfect gas $P = \rho RT$, equation (C11) becomes

$$\frac{\dot{W} RT}{\bar{P} 2 g} = A^2 \bar{\phi}^2 \{ \bar{P}_t - P \} = \frac{\bar{P}}{2} w_s^{*2} \quad (C12)$$

Referring equation (C12) to static conditions at plane E and solving for $\bar{\phi}$

$$\bar{\phi}_E = \left[\frac{1}{2} \frac{(\bar{w}_{E_s}^*)^2}{A_E^2} \left\{ \frac{\bar{P}_E}{\bar{P}_{t_E} - \bar{P}_E} \right\} \right]^{1/2} \quad (C13)$$

where :

$$\bar{w}_{E_s}^* = w_D^* \frac{P_D}{\bar{P}_E} \sqrt{T_E/T_D}$$

An average Mach number M is determined from the pressure ratio \bar{P}_E/\bar{P}_{t_E} . Assuming no change in total temperature across the orifice, i.e.; $T_{t_E} = T_D$, it is possible to find the temperature ratio needed to solve equation (C13).

With the equivalent flow rates and equation (12), average loss coefficients \bar{k}_{D-F} , \bar{k}_{F-G} , \bar{k}_{G-H} , \bar{k}_{G-I} and \bar{k}_{D-X} are determined. For example, the average loss coefficient from plane F to plane G is

$$\bar{k}_{F-G} = \frac{\bar{P}_{t_F} - \bar{P}_{t_G}}{\bar{P}_{t_F}} \bigg/ (\bar{w}_F^*)^2 \quad (\text{in}^{-4}) \quad (C14)$$

At a particular location in plane I the discharge velocity is proportional to the square root of the dynamic pressure.

$$V_i^2 = [H_{atm3} - H_i] - [H_{atm3} - h_i] = q_i \quad (\text{in. H}_2\text{O}) \quad (C15)$$

At each location the velocity relative to the average is then

$$V_i/\bar{V} = \sqrt{q_i} / \frac{1}{n} \sum_i^n \sqrt{q_i} \quad (C16)$$

C.3 Scale Model Nozzle Tubes

The following quantities were recorded

t' - elapsed time (sec)

W_t - weight of water collected (lb)

$P_{in\ g}$ - inlet static pressure (lb/in² gage)

t_w - water temperature (°F)

A_{in} - inlet area (0.07843 in²)

A_{dis} - discharge area (0.11341 in²)

h_{atm} - barometric pressure (in Hg)

Flow rate \dot{w} was determined by dividing the weight of water by the elapsed time. More useful for calculations is the volume flow rate

$$V = \frac{\dot{w} (100)}{3.6093} \quad (\text{in}^3 / \text{sec}) \quad (\text{C17})$$

Velocities at inlet and discharge can be written as

$$V = \frac{V}{A} \quad (\text{C18})$$

Assuming atmospheric pressure at the discharge the loss in total pressure through the tube is

$$P_{t_{in}} - P_{t_{dis}} = \{P_{in} - P_{atm}\} + \frac{1}{2} \rho / g (V_1^2 - V_2^2) \quad (\text{lb/in}^2) \quad (\text{C19})$$

In all tests the water temperature varied only from 55° to 59°F. For $t = 57^\circ\text{F}$ equation (C19) becomes

$$\Delta P_{t_{in-dis}} = P_{in\ g} + (3.965 \times 10^{-3}) V^2 \quad (\text{C20})$$

Re referred to an inlet diameter of 0.316 inches is obtained from equation (B7) with $\mathcal{V} = 160.279 \times 10^{-5} \text{ in}^2/\text{sec}$

$$Re = \frac{V \times 10^4}{3.98} \quad (\text{C21})$$

Using the inlet as reference, the loss coefficient ξ is

$$\xi_{in-dis} = \frac{\Delta P_{t_{in-dis}} (2g)}{e V_1^2} \quad (C22)$$

where
$$e/g = 0.935 \times 10^{-4} \frac{lb-sec^2}{in^4}$$

C.4 Geometrically Similar Model of Section from Plane W to Plane X

Figure 28 shows 6 manometer tubes in a schematic manner. Actually, Stations 2 through 6 have 2 taps each so that h_2 (in H_2O) is an average pressure at Station 2. In addition to pressures, the mass flow rate and water temperature were recorded as described in sub-section C.3. Volume flow rate is determined as in the former tests. Reynolds number referred to an inlet diameter of 1.05 in. is

$$Re = \frac{V \times 10^4}{13.218} \quad (C23)$$

for average temperature conditions.

It is assumed that taps 3 and 5 are placed such that the flow has the same area as the orifice opening. The error in this assumption is absorbed in the flow coefficient K.

Across an orifice the equation of continuity gives

$$A_d V_d = A_{or} V_{or} \quad (C24)$$

where d - station ahead of orifice

or - station behind the orifice

Expressing terms in in. of liquid head, Bernouilli's equation, ignoring losses, gives

$$H_d = \frac{V_d^2}{2g} + h_d = H_{or} = \frac{V_{or}^2}{2g} + h_{or} \quad (C25)$$

Combining equations (C24) and (C25)

$$V_{or} = \sqrt{2g \frac{(h_d - h_{or})}{1 - \beta^4}} \quad (C26)$$

If losses and other factors are included in a coefficient K, the volume flow rate can be written as

$$V = \dot{w}/\rho = K A_{or} V_{or} \quad (C27)$$

Equations (C26) and (C27) are combined to give

$$K = \sqrt{\left\{ \frac{V}{A_{or}} \right\}^2 \frac{(1 - \beta^4)}{2g \Delta h_{d-or}}} = \sqrt{\frac{g_{or} (1 - \beta^4)}{\Delta h_{d-or}}} \quad (C28)$$

Three orifice sizes were tested. Table C-I lists factors for each orifice.

TABLE C-I
GEOMETRIC FACTORS FOR VARIOUS ORIFICES

DIAMETER	β	$1 - \beta^4$	A_{or}
0.757	0.7209	0.7298	0.45007
0.761	0.7248	0.7241	0.45484
0.714	0.6800	0.7862	0.40039

Using Station 6 as an example and assuming stagnation conditions at Station 1, the head loss H_L is written as

$$H_1 - H_6 = h_1 - h_6 - \frac{V_6^2}{2g} = H_{L,1-2} \quad (C29)$$

Compared with other losses, the loss through the inlet orifice is negligible. A loss coefficient from the beginning of the 1.05 in. pipe to Station 6 is then

$$\xi_{1-6} = \frac{\Delta P_{t,1-6} (2g)}{\rho V_d^2} \quad (C30)$$

Introducing the volume flow rate

$$\xi_{1-6} = 578.896 \frac{H_{L,1-6}}{V^2} \quad (C31)$$

C.5 Discharge and Return Assembly

In addition to the quantities measured in the return sub-assembly the following pressures were read

- h_o - static pressure at entrance of model (cm H₂O)
- H_o - total pressure at entrance of model (cm H₂O)
- $h_{atm\ 2}$ - atmospheric reference, manometer bank 2 (cm H₂O)
- h_z - static pressure in plane A, 6 equally spaced taps (cm H₂O)
- H_z - total pressure in plane Z (cm H₂O)
- h_A - static pressure in plane A at holes 1, 14, 27, 40 (cm H₂O)
- H_A - total pressure in plane A between holes 7-8, 20-21, 33-34, 46-47 (cm H₂O)
- h_B - static pressure in plane B at holes 7, 13, 20, 26, 33, 39, 46, 52 (cm H₂O)
- h_C - static pressure in plane C at holes 7, 13, 20, 26, 33, 39, 46, 52 (cm H₂O)
- H_{plen} - pressure in plenum 2 referenced to atmosphere (cm Hg)

Equivalent flow rates found as in Section C.2 include w_u^* , \bar{w}_z^* , \bar{w}_A^* , \bar{w}_F^* , and \bar{w}_G^* . These flow rates are used to calculate the loss coefficients \bar{k}_{Z-A} , \bar{k}_{A-F} , \bar{k}_{F-G} , \bar{k}_{G-H} , and \bar{k}_{G-I} .

Using Re with the 4 in. diameter of the supply pipe as characteristic length, the argument, \bar{k}_{X-F} is read from Fig. 35. Total pressure at plane X is then given by

$$\bar{P}_{tX} = \bar{P}_{tA} - \left\{ \bar{k}_{A-X} \bar{P}_{tA} \bar{w}_A^{*2} \right\} \quad (C32)$$

where :

$$\bar{k}_{A-X} = \bar{k}_{A-F} - \bar{k}_{X-F}$$

An average Re of the flow from plane W to plane X can be written as

$$Re = \bar{w}_W^* \frac{\bar{P}_{tW} (0.02364)}{\sqrt{T_D} \mu} \quad (C33)$$

where:

$$w_W^* = w_u^* \frac{P_u}{\bar{P}_{tW}} \sqrt{\frac{T_o}{T_u}} \quad (C34)$$

and

$$\bar{P}_{tW} = f (\Delta P_{B-C}) + \bar{P}_{tX} \quad (C35)$$

An iteration of equations (C33), (C34), and (C35) is carried out by assuming an initial value of f from Fig. 46. The process converges rapidly because f has a limited range of values.

With the computed values of \bar{P}_{tW} and \bar{w}_W^* , the coefficient \bar{k}_{D-X} is calculated. From equation (12)

$$\xi_{W-X} = \frac{\bar{k}_{W-A}}{2 A^2} \quad (C36)$$

INITIAL DISTRIBUTION LIST

No. Copies

1. Defense Documentation Center Cameron Station Alexandria, Virginia 22314	20
2. Library Naval Postgraduate School Monterey, California 93940	2
3. Commander, Naval Air Systems Command Navy Department Washington, D.C. 20360	1
4. Commander, Naval Ship Systems Command Navy Department Washington, D. C. 20360	1
5. Capt. A. Bodnaruk, USN Naval Ship Systems Command (Code 6140) Navy Department Washington, D.C. 20360	1
6. Office of Naval Research (Power Branch) Attn: Mr. J. K. Patton, Jr. Navy Department Washington, D.C. 20360	1
7. Mr. R. Beichel Liquid Rocket Plant Aerojet-General Corporation Sacramento, California	1
8. Chairman, Department of Aeronautics Naval Postgraduate School Monterey, California 93940	2
9. Professor M. H. Vavra Department of Aeronautics Naval Postgraduate School Monterey, California 93940	3
10. Lcdr. R. J. Kelly, USN Attack Squadron 174 Naval Air Station Cecil Field, Florida	4

DOCUMENT CONTROL DATA - R&D

(Security classification of title, body of abstract and indexing annotation must be entered when the overall report is classified)

1. ORIGINATING ACTIVITY (Corporate author)		2a. REPORT SECURITY CLASSIFICATION	
Naval Postgraduate School Monterey, California 93940		UNCLASSIFIED	
		2b. GROUP	
3. REPORT TITLE			
An Investigation of the Oxidizer Flow Passages in a Dual-Combustion Liquid Rocket Engine			
4. DESCRIPTIVE NOTES (Type of report and inclusive dates)			
Thesis - Aeronautical Engineer			
5. AUTHOR(S) (Last name, first name, initial)			
Kelly, Robert J., LCDR, USN			
6. REPORT DATE		7a. TOTAL NO. OF PAGES	7b. NO. OF REFS
September 1967		131	10
8a. CONTRACT OR GRANT NO.		9a. ORIGINATOR'S REPORT NUMBER(S)	
b. PROJECT NO.			
c.		9b. OTHER REPORT NO(S) (Any other numbers that may be assigned this report)	
d. <i>Distribution unlimited</i>			
10. AVAILABILITY/LIMITATION NOTICES			
This document is subject to special export controls and each transmittal to foreign nationals may be made only with prior approval of the Naval Postgraduate School.			
11. SUPPLEMENTARY NOTES		12. SPONSORING MILITARY ACTIVITY	
		Commander, Naval Air Systems Command, Department of the Navy Washington, D. C. 20360	
13. ABSTRACT			
<p>This work was undertaken to determine the pressure drops in the oxidizer flow passages of a compact dual-combustion liquid rocket engine by means of fluid dynamic model tests, using air instead of liquids, to establish design data. Investigated also were flow distributions and flow instabilities by measurements and flow visualization methods. Changes are indicated to improve the original design.</p> <p>The air tests were carried out over a range of Reynolds numbers to establish the effect of compressibility on the pressure drop loss coefficients. Water tests were undertaken to check the validity of the results and of the proposed calculating method.</p> <p>The tests were conducted at the Turbo-Propulsion Laboratory of the Naval Postgraduate School, Monterey, California</p>			

KEY WORDS

LINK A

LINK B

LINK C

ROLE

WT

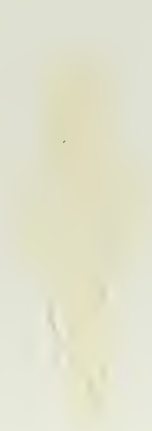
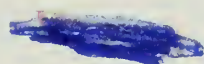
ROLE

WT

ROLE

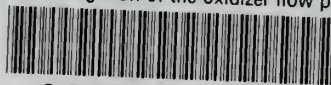
WT

Pressure drop
Rocket engine
Oxidizer
Air Tests
Water Tests



thesK2867

An investigation of the oxidizer flow pa



3 2768 002 12080 0

DUDLEY KNOX LIBRARY